# TIME RESOLVED RADIO POLARIMETRY OF V404 CYGNI'S 2015 OUTBURST

by

ANDREW KENNETH HUGHES

A thesis submitted in partial fulfillment of the requirements for the degree of

Master's of Science

Department of Physics
University of Alberta

# Abstract

Relativistic jets are an ubiquitous element of systems with accreting black holes. These jets carry away a large fraction of the accreted energy which later energizes their surrounding media. On the largest scales, the jets from supermassive black holes found in the center of galaxies provide a powerful feedback mechanism that regulates star formation. Black hole X-ray binaries are their small scale analogs, consisting of a stellar mass black hole accreting from a companion star. The underlying physical processes are fairly (length) scale invariant; however, they evolve on a humanly accessible time-scale due to their smaller size. As synchrotron radiation is the predominant emission mechanism the resulting (radio) waves are linearly polarized with respect to the magnetic field orientation and the local absorption conditions. Here I present VLA observations and a polarimetric analysis of the black hole X-ray binary V404 Cygni taken on June 22$^{\rm nd}$ during its 2015 outburst. The multi-frequency data included simultaneous C (4-8 GHz) and K (20-26 GHz) band radio observations across $\sim$4 continuous hours. The radio frequencies probed the conditions in the radio-loud accretion-powered relativistic jets. After a brief introduction of the emission mechanisms and past observations of similar sources, the evolution of the polarization properties and the frequency-dependent

delays are discussed. The high time-resolution light curves showed a tri-peaked temporal structure across all of the observing frequencies. Each peak was delayed to later times at lower frequencies and qualitatively followed the predicted behaviour of the van der Laan synchrotron plasmoid model. The delays were directly measured from the cross-correlation function between light curves of differing central frequencies. The polarization images were made with a regular $\sim$ 14-min window, constituting one of the highest resolution studies of time-resolved radio polarimetry in flaring black hole X-ray binaries. The polarization properties were extracted from each time bin using both the techniques of rotation measure synthesis and a custom Bayesian forward-modelling approach. The source was observed to be weakly polarized with a polarization angle, fractional linear polarization and rotation measure that was variable in time. The variability points to a rapidly evolving emission environment. However, the system exhibited irregularity during the variability that inhibited the attribution of the observed behaviour to simple jet geometries. The analysis of the weakly polarized emission was limited by the capabilities of the VLA. Future multi-frequency observations will be planned to mitigate these limitations. The routines developed for this thesis can be applied to future observations of rapidly evolving polarized sources, both in black hole X-ray binaries and beyond. Further interpretation will require a more detailed theoretical model that combines the effect of optical depth on observed polarization angle with predictions from a precessing compact steady jet and its ballistic ejecta.

# Preface

This thesis is original work by Andrew K. Hughes. My supervisor, Dr. Gregory Sivakoff, submitted the proposal and organized the planning of these observations. Throughout the body of this thesis there are frequent comparisons to the intensity modelling of the same data (although independently reduced) by Dr. Alexandra Tetarenko of the East Asian Observatory in Hilo, Hawaii and the simultaneous spatially-resolved observations whose analysis was led by Dr. James Miller-Jones of Curtin University in Perth, Australia. Lastly, the custom modelling referenced in the body of the report was an adaptation of the work done by one of Dr. Miller-Jones' undergraduate students, Chris Macpherson.

*"A thesis is never late, nor is it early. It arrives precisely when it means to."*

Adapted from Gandalf the Grey

# Acknowledgements

First and foremost I would like to thank my supervisor, Dr. Gregory Sivakoff, if not for his tireless motivational, financial and academic support I would not have been able to pursue my M.Sc. I would also like to give a massive thank you to both Dr. Cameron Van Eck and Dr. Frank Schinzel for their immeasurable help in the reduction, imaging and interpretation of the polarimetric observations. Additionally, I'd like to thank everyone in the astrophysics group at the University of Alberta, both faculty and students, the positive community and interesting discussions (both in and out of my area of expertise) have kept me focused and motivated. Finally, I would like to thank my parents for never giving up on me and always supporting me, especially during the trying times in my youth.

# Contents


**1 Introduction** **1**

1.1 Black Hole X-ray Binaries . . . . . 2

1.1.1 Accretion States . . . . . 4

1.1.2 Relativistic Jets . . . . . 7

1.2 Radio Emission and Propagation . . . . . 9

1.2.1 The Basic Picture . . . . . 10

1.2.2 Synchrotron Spectra of an Ensemble of Electrons . . . . 12

1.2.3 Polarization Properties . . . . . 14

1.2.4 Applications to Observations of Astrophysical Jets . . . . 15

1.2.5 The Faraday Effect and Rotation Measure . . . . . 17

1.3 V404 Cygni . . . . . 19

**2 Observations** **21**

2.1 Basics of Radio Interferometry . . . . . 22

2.2 Calibration and Editing . . . . . 27

2.3 Imaging . . . . . 33

**3 Methods and Results** **40**

3.1 Peak Delays . . . . . 40

3.2 Polarimetry . . . . . 45

3.2.1 Rotation Measure Synthesis . . . . . 45

3.2.2 Bayesian Modelling . . . . . 50

3.3 Fractional Linear Polarization . . . . . 54
3.4 Results . . . . . 57

**4 Discussion** **61**
4.1 Peak Delays . . . . . 61
4.1.1 Model Comparisons . . . . . 65
4.1.2 Delay Corrected Polarimetry . . . . . 67
4.2 Polarization Properties . . . . . 69
4.2.1 Rotation Measure . . . . . 69
4.2.2 Polarization Angle . . . . . 72
4.2.3 Fractional Polarization . . . . . 74

**5 Conclusions and Future Work** **78**

**Appendices** **91**
A Data Tables . . . . . 91
B Delay Histograms . . . . . 97

# List of Tables

2.1 The 3rd-order polynomial fits for the total intensity and the fractional polarization spectra of the primary calibrator. . . . . 32

2.2 Table of imaging properties. The central frequency of the lowest ($\nu_i$) and highest ($\nu_f$) channels and the imaging bandwidth ($\Delta\nu$) are reported in MHz. The temporal imagin window ($\Delta t$) is reported in seconds. Lastly, the theoretical thermal noise threshold ($\sigma_{\rm RMS}$) and the median noise values for each Stokes parameter ($\sigma_I$, $\sigma_Q$, $\sigma_U$) are reported in mJy. The theoretical noise estimates were calculated using the VLA exposure calculator; `obs.vla.nrao.edu/ect/`. . . . . 36

A.1 Polarimetric results for the 5/7 GHz observations with no delay correction. RM1 and RM2 correspond to the polarization proprieties of the most significant and second most significant detection in each Faraday dispersion function. Note that some FDF had a 3rd or 4th component, but they were omitted from the data table. 91

A.2 Polarimetric results for the 5/7 GHz observations corrected for the flare I delays. . . . . 92

A.3 Polarimetric results for the 5/7 GHz observations corrected for the flare II delays. . . . . 93

A.4 Polarimetric results for the full bandwidth observations without a delay correction. . . . . 94

A.5 Polarimetric results for the full bandwidth observations corrected with the flare I delays. . . . . 95
A.6 Polarimetric results for the full bandwidth observations corrected with the flare II delays. . . . . 96

# List of Figures

1.1 Typical transient outburst cycle of a LMXRB. Temporally, the outburst will follow the higher luminosity horizontal track during the initial transition from hard-to-soft, and return along the lower luminosity track during its return to quiescence. Hardness is defined as the ratio of hard and soft X-ray photons, i.e., the higher the hardness the harder (higher energy) the average X-ray photon. The figure was adapted from Homan and Belloni (2005). 5

1.2 Schematic of a typical self-absorbing synchrotron spectrum, the turnover frequency is highlighted with the dotted black line. Both the units and the absolute values presented on the axis are arbitrary. 8

1.3 Schematic of the synchrotron emission process; for a constant pitch angle, $\alpha$ (equivalent to $\alpha_p$), the electron's velocity vector, the edges of the cones, precesses about the direction of the magnetic field, $B$. The majority of the emitted radiation is confined to the shaded region, within an angle of $\theta \sim \gamma^{-1}$ of the trajectory of the electron. Figure was adopted from Longair (2011). 10

1.4 A schematic diagram of a partially self-absorbing synchrotron spectra for an power-law distribution of electrons. The dotted black lines separate the different emission regimes. . . . . 17

2.1 A schematic diagram of a 2-element interferometer, adopted from Taylor et al. (1999). . . . . 23

2.2 A schematic diagram of the polarization ellipse describing any arbitrary elliptical polarization. . . . . 27
2.3 Fractional Polarization spectra of the primary calibrator for the; (a) 5/7 GHz and (b) 21/26 GHz radio bands. The shaded regions represent the range of frequencies spanned by each observing band. 32

3.1 The intensity light curves, of the fourth spectral window, for each radio baseband binned into 10.0s intervals. The dotted lines (of equivalent color) highlight the I→II transition, and the dashed lines the II→III. The figure clearly highlights a ubiquitous tri-peaked temporal structure across all of the observing frequencies. 41
3.2 The cross-correlation function between the spectral windows with central frequencies of $\nu_c = 7.897$ GHz and $\nu_c = 26.347$ GHz for flare II. The sampled points are in blue and the smoothed fit is seen in black. The inset displays a zoomed view of the peak region, highlighting the oscillatory substructure produced by the ZDCF. . . . . 43
3.3 The measured delays for; (a) The full bandwidth ($\nu_{\rm ref} = 26.347$ GHz) and (b) The 5/7 GHz ($\nu_{\rm ref} = 7.897$ GHz) limited light curves. 44
3.4 A full bandwidth Faraday dispersion function for the time bin between 12:04:00–12:18:00 (absent any delay correction). The $\phi_f$ ranges of the two figures are; (a) $\pm\,10$ FWHM about the central maximum and (b) the full Faraday depth range of $\pm\,9 \times 10^5$ rad m$^{-2}$. . . . . 49
3.5 MCMC modelling of the full bandwidth observations between 12:04:00-12:18:00. (a) The Stokes Q data (blue) with the best fit model over-plotted (red). (b) The Stokes U data (blue) with the best fit model over-plotted (red). (c) Posterior distributions (upper) and walker paths for the sampling iterations (lower) for each model parameter. . . . . 53

3.6 Fractional polarization (blue) and intensity (grey) as a function of time. Each panel represents a different baseband; 26 GHz (top), 21 GHz (2nd from the top), 7 GHz (3rd from the top), 5 GHz (bottom). The horizontal lines are the fractional polarization that corresponds to the detection significance seen on the right hand side of the plot. . . . . 56

3.7 Polarization properties of the 5/7 GHz data, without the application of a peak delay correction for both the MCMC and RM synthesis routines. The shaded regions represent the 99, 90, and 75% significance regions for the 5 GHz observations (the darker shade the more significant). The dotted black line in the lower panel corresponds to the intrinsic polarization angle if the rotation measure is assumed to be a constant value equal to the weighted mean of the RM Synthesis results within the 99% significance interval. . . . . 58

3.8 RM synthesis results for the 5/7 GHz data, with (orange) and without (blue) a delay correction. The shaded regions are the same as Figure 3.7. The vertical dotted line marks the division between flare I and II. The flare I/II delay correction was applied to the data points to the left/right of the vertical line. . . . . 59

3.9 RM synthesis results for the full baseband data, with (orange) and without (blue) a delay correction. The shaded regions are the same as Figure 3.7. The vertical dotted line marks the division between flare I and II. The flare I/II delay correction was applied to the data points to the left/right of the vertical line. . . . . 60

4.1 Key plots from the June 22nd VLBA observations; (Top) Position angles of the spatially resolved jet components. (Bottom) Light curves of resolved ejecta, compact core and total integrated flux as a function of time. These figures were taken directly from Miller-Jones et al. (2019). . . . . 63

4.2 Flare III light curve with; (top) no delay correction, (middle) empirical delay correction measured by the ZDCF for flare III, (bottom) empirical delay correction measured by the ZDCF for flare II. Note, that the ZDCF algorithm fits the single peak in the 5/7 GHz light curve to the early time peak in 21/26 GHz. Applying the flare II delay correction to the flare III light curves positions aligns the 5/7 GHz light curves with the late time peak. 64

4.3 Peak delays for each of the three flares as a function of frequency. The data points correspond to the delays measured by the ZDCF algorithm for each of the spectral windows. The shaded regions of similar colour visualize the predicted range of delays for each flare's model components. The dark regions correspond to delay range spanned by the approaching/receding components of the dominant ejections; ejection 3 and ejection 7 for flare II and III respectively. The light hatched region corresponds to the full range of delays spanned by each flares composite ejecta. The predicted delay range of flare I is significantly narrow and, as a result, it was limited to a single shaded region. It should be noted that (although difficult to see) the lower limits of the shaded region for flare I and II are overlapping. . . . . 66

4.4 A schematic diagram of the different angles of interest as observed by their corresponding interferometric arrays for component S2 and S3. *left*: The components as seen by the VLBA. The dashed line arrows correspond to the direction of propagation of the ejecta projected onto the sky. The position angle (PA) for the ejecta is measured East of North. *right*: The events as seen by the VLA. The VLA observations do not have sufficient angular resolution to separate the compact core and the discrete ejecta and, as a result, a single source is imaged. The colour-coordinated shaded regions corresponds to the range of intrinsic polarization angles, $\psi_0$, during the corresponding times of dominance for each component. The PA and $\psi_0$ values for component S3 were mapped onto the compass. . . . . 73

B.1 Distribution of the ZDCF delays for the Monte Carlo re-sampled light curves of flare I limited to the 5/7 GHz bandwidth. . . . . 97

B.2 Distribution of the ZDCF delays for the Monte Carlo re-sampled light curves of flare II limited to the 5/7 GHz bandwidth. . . . . 98

B.3 Distribution of the ZDCF delays for the Monte Carlo re-sampled light curves of flare II limited to the 5/7 GHz bandwidth. Notice the abrupt transition from 10 minutes to 25 minutes when the comparative frequency changes from 5.185 GHz to 5.057 GHz. . 99

B.4 Distribution of the ZDCF delays for the Monte Carlo re-sampled light curves of flare I limited to the full bandwidth. . . . . 100

B.5 Distribution of the ZDCF delays for the Monte Carlo re-sampled light curves of flare II limited to the full bandwidth. . . . . 101

B.6 Distribution of the ZDCF delays for the Monte Carlo re-sampled light curves of flare III limited to the full bandwidth. . . . . 102

# Chapter 1

# Introduction

As a massive star approaches the end of its lifetime and its internal fuel has been depleted through millions of years of nuclear fusion, the outward pressure is no longer able to support itself against the immense inward gravitational pull, resulting in a catastrophic structural failure and a rapid inward collapse. In most scenarios, the collapse will not completely destroy the star; instead it will produce one of two stellar remnants, a neutron star (NS) or a black hole (BH). During the stellar collapse the rapidly increasing density promotes electron capture processes, converting the majority of nucleons into neutrons. Like electrons, neutrons follow Fermi-Dirac statistics that prohibit the occupation of a single state by multiple neutrons and introduce a new outward (degeneracy) pressure[1]. Situations where neutron degeneracy is sufficient to halt the collapse will form a highly compact neutron star. However, for the most massive stars the neutron degeneracy pressure will be overcome and the collapse will continue, resulting in the formation of a singularity, i.e a black hole[2].

The immense gravitational fields and potential energies of BHs make their local environments home to some of the most energetic phenomena in the

[1]For less massive stars the collapse will be halted by electron (rather than neutron) degeneracy. The resulting stellar remnant is called a white dwarf.

[2]Under certain conditions the star is thought to experience a pair-instability supernova that results in runaway nuclear fusion process and an inevitable thermonuclear detonation that completely destroys the star leaving behind no stellar remnant (Fryer et al., 2001).

observable universe, functioning as natural laboratories for the study of relativity and high energy astrophysics. However, the strength of these gravitational fields inhibit intrinsic electromagnetic radiation, as not even light can escape its inward pull, making isolated BHs "invisible" to direct photon-based observations. Instead, BHs are often studied through their interactions with other astrophysical bodies. An archetypal example of such a system — and the topic of this thesis — are black hole X-ray binaries (BHXBs). BHXBs are rapidly evolving binary systems composed of a stellar mass BH accreting material from a non-degenerate stellar companion. Their bright, multi-wavelength emission spectra have proven to be invaluable tools in the study of accretion/accretion-powered phenomena, e.g. the recent evidence for Lense-Thirring precession of an accretion powered jet (Miller-Jones et al., 2019). This thesis will expand upon the work done by Tetarenko et al. (2017) on the BHXB V404 Cygni, focusing on the time resolved evolution of the polarization properties.

For the remainder of Chapter I will outline a general description of the observations of the BHXB population as a whole, the theory behind its emission processes and introduce the observational history of V404 Cygni. Chapter 2 describes the observations as well as the data reduction and imaging procedures used in this thesis. For Chapter 3 I will outline the methods applied to the reduced data and state the key results, leaving the interpretations for Chapter 4. Finally, Chapter 5 functions as a conclusion, restating the key results and outlining the potential for future research of a similar kind.

## 1.1 Black Hole X-ray Binaries

The behaviour of a BHXB is dependent on its orbital parameters, mass ratio, local environment and donor star. The heterogeneity among BHXBs has resulted in the categorization into a common set of observationally (and somewhat arbitrarily) defined sub-classes;

- **High Mass X-ray Binary (HMXB)**: The companion star's mass obeys $M_2 \gtrsim M_{\rm BH}$, where the subscripts 2 and BH refer to the companion star and the black hole, respectively, and its spectral type is either O or B. The accretion is typically driven by strong stellar winds from the companion.

- **Low Mass X-ray Binary (LMXB)**: The companion star's mass obeys $M_2 \lesssim M_\odot$, where $M_\odot$ is a solar mass and its spectral type is A or "lower". These systems typically accrete through the Roche-Lobe overflow through the binary's second Lagrange point.

- **Transient:** A BHXB that exhibits bright (often recurrent) outbursts (days to weeks) followed by extended periods of quiescence (lasting months to years). Some LMXBs have remained in the outburst state for decades and would have been characterized as persistent had X-ray astronomy started a few decades later.

- **Persistent:** An X-ray binary that remains in outburst for an extended period of time (possibly millions of years).

For a detailed catalog of confirmed and candidate BHXBs the reader is directed to the WATCHDOG database (Tetarenko et al., 2016). The variable multi-wavelength emission produced during an outburst provides a real time view of the evolving structures within the X-ray bright accretion disk and the radio (through infrared) bright relativistic jets. Strong observational correlations between the temporal evolution of the X-ray and radio emission suggest a coupling between the accretion flow and the relativistic jet, where the morphology of the jet seems to be tied to the *state* of the accretion flow (Done et al., 2007; Fender and Gallo, 2014).

### 1.1.1 Accretion States

Within the lifetime of a single outburst, the X-ray emission exhibits a variety of characteristic spectral and timing properties, resulting in a (growing) number of classifications or states (Belloni, 2010; Done et al., 2007; Homan and Belloni, 2005). The state that a transient BXHRB will spend the majority of its lifetime in is called quiescence, and is characterized by a low X-ray luminosity $L_X \lesssim 10^{33.5}$ erg s$^{-1}$ (McClintock and Remillard, 2006). The beginning of the outburst is marked by a rapid increase in luminosity and a transition to the *Hard State* (HS). In this state, the spectrum is dominated by hard (non-thermal) X-rays, described by a power law with photon index of $\Gamma \sim 1.7$[3], with a secondary soft X-ray thermal component. The X-ray timing properties are characterized by a power density spectra (PDS) with strong band-limited noise and an integrated fractional root mean square (RMS) variability on the order of 30% (McClintock and Remillard, 2006). The *Soft State* (SS) follows the HS, experiencing an inversion of the dominant spectral component (soft thermal X-rays now dominate), a steepening of the hard X-ray power law ($\Gamma \gtrsim 2.5$) and a reduction in the integrated fraction RMS variability to $\lesssim 10\%$. In a large section of the literature the HS is called the *low hard state* and the SS the *high soft state*. However, the terminological use of "low" and "high" is a historical remnant of the foundational research into Cyg X-1, involving observations of the 1-10 keV (soft) X-ray band (Tananbaum et al., 1972). Subsequent observations found that the spectra in the HS frequently peak at $\sim 100$ keV, suggesting that the hard X-ray luminosity was systematically underestimated. Since then the SS and HS have been observed at a broad range of overlapping luminosities (Homan and Belloni, 2005).

Furthermore, continuous observations had uncovered a number of intermediate states during the transitions between the HS and SS. The intermediate

[3] $I_\nu \propto \nu^{-(\Gamma+1)}$. The photon index ($\Gamma$) is not equivalent to the electron power-law index $p$ or the radio spectral index $\alpha$ mentioned in the following sections.

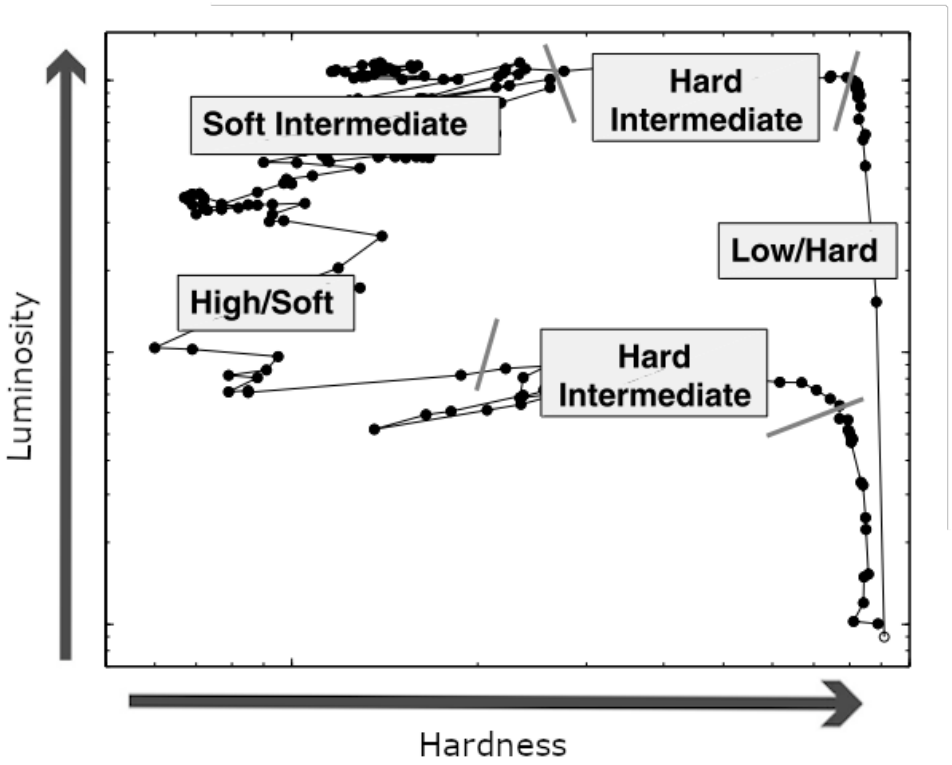


**Figure 1.1:** Typical transient outburst cycle of a LMXRB. Temporally, the outburst will follow the higher luminosity horizontal track during the initial transition from hard-to-soft, and return along the lower luminosity track during its return to quiescence. Hardness is defined as the ratio of hard and soft X-ray photons, i.e., the higher the hardness the harder (higher energy) the average X-ray photon. The figure was adapted from Homan and Belloni (2005).

state nomenclature will follow Homan and Belloni (2005) introducing the *Hard Intermediate State* (HIMS) and the *Soft Intermediate State* (SIMS). A typical outburst track can be seen in Figure 1.1.

The HIMS is characterized by a smooth softening of the power-law to a photon index of $\Gamma \sim 2.5$, an increase in the thermalized flux, a decrease in the integrated RMS variability ($\sim 10 - 20\%$) and the emergence of strong type-C quasi-periodic oscillations (QPOs)[4]. The SIMS maintains the same spectral properties, but with a rapid decrease of the integrated RMS variability ($\lesssim 0.1$) and a transition to Type A or Type B QPOs. Occasionally, a BHXB will exhibit

[4]QPOs are statistically significant noise spikes observed in the PDS, however their physical origins are poorly understood. See (Ingram and Motta, 2020) for a comprehensive review

anomalously high luminosities during the hard-to-soft transitions ($L_{\rm edd} \gtrsim 0.2$), retaining the steepened power-law spectra but with hard X-rays constituting $40 - 90\%$ of the total flux. In these cases the intermediate states are replaced by this *very high* or *steep power law* (SPL) state, which is thought to be a signature of the highest rates of mass accretion among the BHXB population (Lewin and van der Klis, 2006). During the twilight of an outburst, spectral and timing properties follow similar transitions (in reverse) returning to quiescence, typically along a lower luminosity track. It should be noted that there are "failed" outbursts where a system will never fully transition to the SS, instead it will return from the HIMS/SIMS immediately back to the HS before returning to quiescence (Dunn et al., 2010).

The composite spectra are associated with a "piece-wise" accretion flow composed of two or more individual components. Soft X-rays are typically emitted from a multi-temperature, geometrically thin, optically-thick, thermalized accretion disk (Done et al., 2007) and hard X-rays, from a radiatively inefficient, optically-thin, geometrically thick coronal flow composed of a population of electrons that emit via cyclo-synchrotron/bremsstrahlung radiation or Compton up-scattering of seed photons (e.g., Yuan and Narayan 2014). One of the simplest toy models that explains the state evolution is the *Truncated Disk/Hot Inner Flow* (TDHIF), composed of an outer accretion disk and an inner coronal flow connected at some transitional radius. The origin of the transition radius is not well understood, but a popular qualitative explanation invokes a pseudo-evaporation. At the transitional radius, the temperature/density of the disk are sufficiently high/low to facilitate a "state transition" from the cool(er) compact disk to a hot and sparse coronal flow (Meyer et al., 2000). In quiescence the transitional radius is located far from the black hole. During accretion, the disk builds up material, as the transitional radius migrates inwards, liberating gravitational potential as heat and increasing the temperature and luminosity of the disk. When the inner edge of the disk reaches the hydrogen ionization

temperature, an ionization instability wave propagates throughout the disk, drastically increasing its viscosity. The higher viscosity drives rapid accretion onto the central BH and an inward migration of the inner disk radii (potentially down to the inner-most stable orbit). This ionization instability is referred to as the disk-instability model (DIM), originally developed to explain the novae observed in cataclysmic variables (Lewin and van der Klis, 2006). The rapid accretion exhausts the material in the disk, resulting in a dip below the ionization temperature ending the instability and returning the system to quiescence. To first order the TDHIF describes the large-scale outburst behaviour well, making it a useful tool to relate the accretion flows to an evolving jet structure.

### 1.1.2 Relativistic Jets

Accretion powered relativistic jets are generally grouped into two morphological categories; steady, compact jets and transient, discrete jet ejecta. Compact jets are characterized by optically-thick spectra with an inverted or flat spectral index ($\alpha \gtrsim 0$; for $I_\nu \propto \nu^\alpha$). The emission extends from the radio up to a spectral break (typically in the sub-mm or infrared regime) where the jet emission becomes optically-thin, $\alpha < 0$ (Russell et al., 2013). The inverted portion of the spectra is a result of the superposition of multiple spatially-unresolved synchrotron components that originate from different radii along the jet axis, with higher frequency emission being produced closer to the jet's base (Blandford and Königl, 1979). As a result, each frequency below the break frequency originates from a narrow range of distances along the jet axis, probing the spatial region where the optical depth (at a given frequency) approaches unity. Compact jets are typically linked to the HS, as is the case with the spatially resolved AU-scale outflows of Cyg X-1 (Stirling et al., 2001).

Conversely, the discrete ejecta exhibit a single self-absorbed synchrotron spectrum (Figure 1.2) with optically-thin components that often extend well into the radio bands (Fender, 2006). These ejecta have been imaged at milliarcsecond

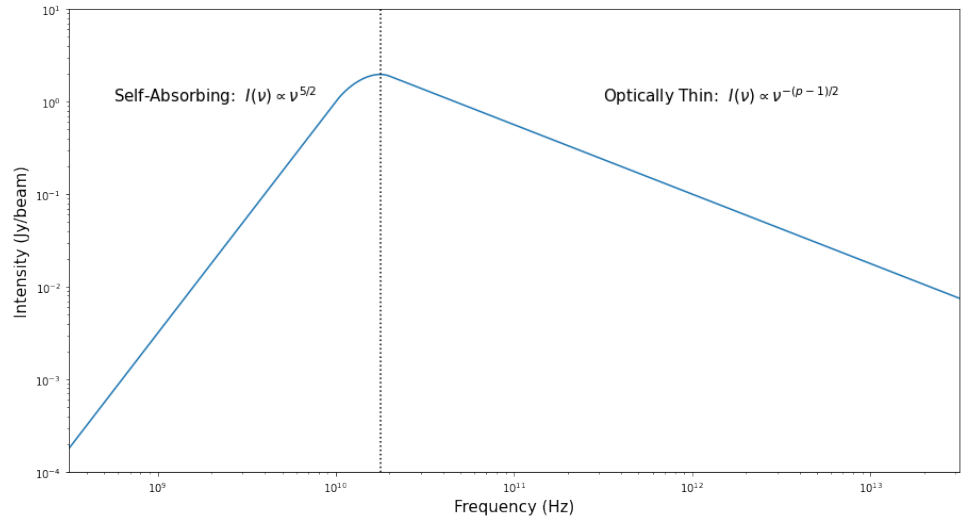


**Figure 1.2:** Schematic of a typical self-absorbing synchrotron spectrum, the turnover frequency is highlighted with the dotted black line. Both the units and the absolute values presented on the axis are arbitrary.

resolutions with very long baseline interferometry (VLBI) (Hannikainen et al., 2001; Rushton et al., 2017; Miller-Jones et al., 2019). Each ejection is typically modelled as a finite knot of magnetically threaded plasma (i.e.,a plasmoid) launched at mild to highly relativistic speeds. The launching mechanism is thought to be a result of a sudden injection of particles and energy into the synchrotron emitting plasma, "breaking off" a plasmoid and accelerating it along the jet axis (the origin of this injection remains unknown). During downstream propagation each plasmoid is subject to an expansion, decreasing the particle, magnetic and energy densities alongside its increasing radius. This model is known as the Van der Laan model (vdL) and was formalised in van der Laan 1966. Each ejection corresponds to a multi-frequency flaring event with well defined (frequency-dependent) rise and decay phases lasting minutes-to-hours — a significantly shorter timescale then the total lifetime of an outburst (Fender, 2006; Tetarenko et al., 2017). The lower frequency light curves appear as temporally smoothed and delayed versions of their high frequency counterparts, as a result of an expansion driven, evolving optical depth.

The coupling between the accretion flow and the jet has strong empirical

evidence. In the hard and quiescence states there is a positive correlation between the X-ray and radio fluxes, characteristic of a steady jet that is driven by the accretion flow (Gallo et al., 2003; Meyer-Hofmeister and Meyer, 2014). Additionally, the hard-to-soft transitions frequently exhibit transient ejection events that are interestingly absent during the return to quiescence (e.g., Fender et al. 2009). Lastly, as the BHXB enters the SS the system crosses the "jet-line", where the radio emission is substantially suppressed or outright quenched. During the transition back to the HS the jet-line corresponds to a reappearance of the compact jet. Despite these clear connections between the radio and X-ray emission (i.e, the jet and the accretion flow), the physical mechanisms responsible for the launching and evolution of jets are yet to be fully realised. However, theory suggests that the processes are very likely to be a result of an evolution of the local magnetic environment (e.g., Blandford and Znajek 1977; Blandford and Payne 1982; Contopoulos et al. 2012).

The synchrotron radio emission generated in the jet has an intrinsic degree of linear polarization that is dependent on the underlying geometric, spectral, and magnetic field properties. Thus, time-resolved radio polarimetry is a tool for probing changes in magnetic environment during jet ejections.

## 1.2 Radio Emission and Propagation

As previously stated, the primary emission mechanism for relativistic jets in BHXBs is through synchrotron radiation. Due to the complexity of the required calculations, the following subsections will state many of the key spectral and polarization properties absent their formal derivations. The reader is directed to Rybicki and Lightman (1979) and Longair (2011) (and references therein) for a comprehensive derivation.

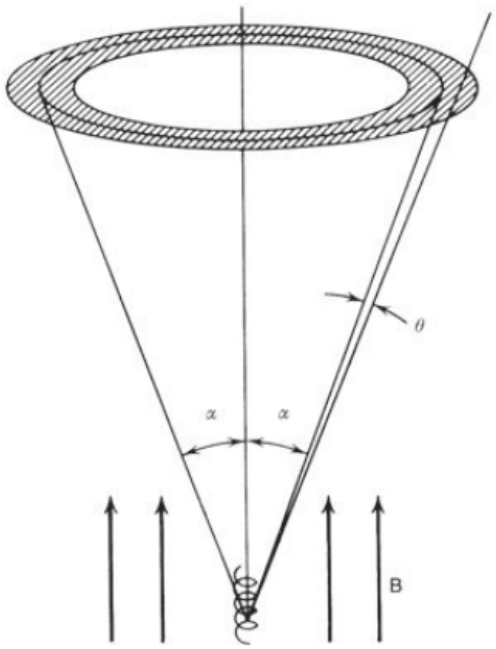


**Figure 1.3:** Schematic of the synchrotron emission process; for a constant pitch angle, $\alpha$ (equivalent to $\alpha_p$), the electron's velocity vector, the edges of the cones, precesses about the direction of the magnetic field, $B$. The majority of the emitted radiation is confined to the shaded region, within an angle of $\theta \sim \gamma^{-1}$ of the trajectory of the electron. Figure was adopted from Longair (2011).

### 1.2.1 The Basic Picture

Synchrotron emission is a result of the dipole radiation from an electron accelerating around a magnetic field line. Considering the simplest case of a constant, unidirectional magnetic field of magnitude $B$ and an single electron orbiting about it with pitch angle $\alpha_p$ (i.e, the angle between the electron velocity and the magnetic field direction; Figure 1.3) and velocity $v$, the Lorentz factor of the electron is given by,

$$\gamma = \frac{1}{\sqrt{1 - \frac{v^2}{c^2}}}. \tag{1.1}$$

Assuming the pitch angle remains constant, it has been shown that the energy loss rate via radiation is given by,

$$-\frac{dE}{dt} = \sigma_T c \frac{B^2}{\mu_0} \left(\frac{v}{c}\right)^2 \gamma^2 \sin^2 \alpha_p, \tag{1.2}$$

where $\sigma_T$ is the Thomson cross-section for the electron, $c$ is the speed of light, and $\mu_0$ is the magnetic permeability of free space. During an electron's lifetime, scattering processes will cause significant pitch angle variability. Thus, assuming an isotopic distribution of pitch angles the average energy loss rate is given by,

$$-\frac{dE}{dt} = \frac{2}{3}\sigma_T c \frac{B^2}{\mu_0} \left(\frac{v}{c}\right)^2 \gamma^2. \tag{1.3}$$

In the non-relativistic case ($v \ll c$; i.e., gyroradiation) beaming effects are negligible. Here the variability of the electric field in the observer's frame adopts a sinusoidal form and the resulting electromagnetic radiation has a frequency equal to the non-relativistic gyrofrequency $\nu_g = \frac{eB}{2\pi m_e}$ multiplied by the pitch angle,

$$\nu = \nu_g \sin \alpha_p. \tag{1.4}$$

In the ultra-relativistic limit ($v \sim c$), as is the case for synchrotron emission, the radiation is subject to strong beaming effects along the electron's trajectory with 50% of the radiated power confined within an angle $\theta \sim \gamma^{-1}$ with respect to the velocity vector. As a result, an observer will detect a pulse of radiation every time the velocity vector lies within an angle of $\gamma^{-1}$ with respect to the observer's line of sight. The duration time of the pulse is,

$$\Delta t \sim \frac{1}{\gamma^2 \nu_g \sin \alpha_p}, \tag{1.5}$$

and its spectral decomposition via Fourier techniques now has multiple components (when compared to the singular component in gyroradiation) with a maximum emissivity at a frequency of $\nu \sim \Delta t^{-1}$,

$$\nu \sim \gamma^2 \nu_g \sin \alpha_p. \tag{1.6}$$

Thus, to first order, the observed radiation frequency from an ultra-relativistic electron accelerating around a magnetic field will be a factor of $\gamma^2$ larger (and more energetic) than the non-relativistic case.

### 1.2.2 Synchrotron Spectra of an Ensemble of Electrons

An observed synchrotron spectrum will be produced by an ensemble of individual electrons. The energy distribution of a non-thermal electron population is often assumed to follow a power-law distribution with an electron power-law index $p$,

$$N(E)dE = CE^{-p}dE, \tag{1.7}$$

where $N(E)dE$ is the number density of electrons within the energy interval $E + dE$ and $C$ is a constant. Given that the emissivity from a single electron is strongly peaked at its maximum Fourier component, assume that an electron of energy $E$ emits radiation at,

$$\nu \sim \ \gamma^2 \nu_g \sin \alpha = \left( \frac{E}{m_e c^2} \right)^2 \nu_g \sin \alpha. \tag{1.8}$$

Note, that in the previous step the Lorentz factor of the electron was replaced using the relativistic energy equation, $E = \gamma m_e c^2$. Therefore, the energy radiated within the frequency range $\nu + d\nu$ can be attributed to electrons of energy $E + dE$. The emissivity per unit volume (henceforth volume emissivity),

$J$, is given by,

$$J(\nu)d\nu = -\frac{dE}{dt}N(E). \tag{1.9}$$

By substituting in Equation (1.3), (1.7), and (1.8) into (1.9), one finds that the volume emissivity has a frequency dependency of the following form,

$$J(\nu) \propto \nu^{-\frac{p-1}{2}}. \tag{1.10}$$

Fortunately, the full derivation (absent the simplifying assumptions) arrives at an identical proportionality. The volume emissivity can be related to the observed intensity, $I$, through the radiative transfer equation,

$$\frac{dI}{dx} = -\mu(\nu)I(\nu) + \frac{J(\nu)}{4\pi}, \tag{1.11}$$

where $\mu$ is the absorption coefficient of the system. Solving for the intensity of a source with a characteristic length scale, $L$, and a length independent volume emissivity,

$$I(\nu) = \frac{J(\nu)}{4\pi\mu(\nu)}\left(1 - e^{-\mu(\nu)L}\right). \tag{1.12}$$

For a source that is optically-thin, $\mu(\nu)L \ll 1$, the exponential is expanded as a Maclaurin series, discarding any terms of order-2 or higher. Thus, for optically-thin synchrotron emission the intensity is directly proportional to the volume emissivity,

$$I(\nu) \propto J(\nu) \longrightarrow I_{\text{thin}}(\nu) \propto \nu^{-\frac{p-1}{2}}. \tag{1.13}$$

The exponent in Equation (1.13) is equivalent to the previously introduced spectral index, $\alpha \equiv -\frac{p-1}{2}$, with typical values of $p \sim (1-2)$ (Markoff et al., 2001).

For an optically-thick source, $\mu(\nu)L \gg 1$, the exponential becomes negligible and the intensity is proportional to the ratio of the volume emissivity and the absorption coefficient. It should be noted that the term "absorption" is being used loosely in this context, the coefficient includes both the inverse process of *synchrotron self-absorption* and "negative" absorption from stimulated or spontaneous emission within the plasma. These processes can been interrelated through a detailed treatment of the Einstein coefficients resulting in a derived absorption coefficient with a frequency dependency of $\mu(\nu) \propto \nu^{-\frac{p+4}{2}}$, and as a result, the spectrum of a self-absorbing synchrotron source follows,

$$I_{\text{thick}}(\nu) \propto \nu^{\frac{5}{2}} \tag{1.14}$$

In this idealized case, a synchrotron source of a power-law distributed population of electrons will be self-absorbed below a turnover (or break) frequency and optically-thin above it (see Figure 1.2).

### 1.2.3 Polarization Properties

A formal derivation of synchrotron emission necessitates a vector treatment of the electron dynamics, and therefore the selection of a coordinate system. In Rybicki and Lightman (1979) and Longair (2011) the coordinate system is chosen to include the direction to the observer $\mathbf{n}_0$ and the directions perpendicular/parallel to the projection of the magnetic field on the plane of the sky, $\mathbf{n}_\perp/\mathbf{n}_\parallel$ (this greatly simplifies the analysis). Since the radiation propagates along $\mathbf{n}_0$, its polarisation state is fully described by the strength of the intensities along the $\mathbf{n}_\perp$ and $\mathbf{n}_\parallel$ directions. The observed polarization angle is parallel to the direction where the majority of the intensity is liberated and the fractional polarization is defined by,

$$\Pi = \left| \frac{I_\perp - I_\parallel}{I_\perp + I_\parallel} \right|. \tag{1.15}$$

Once again, by assuming a power-law distribution of electrons the polarization properties of an optically-thin synchrotron source follow,

$$\frac{I_{\text{thin},\perp}}{I_{\text{thin},\parallel}} = \frac{3p+5}{2}, \quad \text{and} \tag{1.16}$$

$$\Pi_{\text{thin}} = \left| \frac{3p+3}{3p+7} \right|. \tag{1.17}$$

for a typical power-law index of $p \sim 2.5$, optically-thin synchrotron emission will be $\sim 72\%$ linearly polarized, with a polarization angle oriented perpendicular to the projected magnetic field. If the source is optically-thick, the absorption coefficient must be considered in the radiative transfer equation; however, it too must be decomposed into its orthogonal components. The full decomposition can be found in Ginzburg and Syrovatskii (1969) and references therein. The optically-thick, self-absorbing synchrotron polarization properties are as follows,

$$\frac{I_{\text{thick},\perp}}{I_{\text{thick},\parallel}} = \frac{3p+5}{3p+8}, \quad \text{and} \tag{1.18}$$

$$\Pi_{\text{thick}} = \left| \frac{3}{6p+13} \right|. \tag{1.19}$$

For a typical power-law index of $p \sim 2.5$, a self-absorbed synchrotron spectra is expected to see a drop in the polarization fraction to $\sim 11\%$, and an inversion of the dominant intensity component aligning the polarization angle parallel to the projected magnetic field.

### 1.2.4 Applications to Observations of Astrophysical Jets

The assumption of a constant, unidirectional magnetic field is not likely prescribable to the anisotropic local environments of BHXBs. In regards to polarization

observations, Equation (1.17) and (1.19) become upper limits that quantify how ordered the magnetic field directions are within a spatial resolution element and with respect to the line of sight (Blandford and Königl, 1979). Similarly, the polarization angle is determined by the dominant direction of the magnetic field (if there is one) and the absorption conditions. The initial (pre-launch) magnetic field orientations within the jet plasma are thought to be intrinsically disordered (i.e., no large scale magnetic field direction) and at some point during the ejection or propagation processes some physical mechanism results in the emergence of a preferential magnetic field direction and an observed polarization. Thus, the relationship between the jet axis, magnetic field and polarization angle are dependent on the mechanism that generates the preferential field direction.

In the simplest ejecta geometry the dominant field direction arises through a shock-compression (potentially during launch) with a magnetic field parallel to the shock front and normal to the jet axis (Laing, 1980b). This model has been successfully applied to a number of spatially resolved ejecta, although others have required a more complex description (see Curran et al. 2014 and references therein).

For compact jets, the archetypal model is described in Blandford and Königl (1979) and assumes a conical geometry. The synchrotron emission originates from an inhomogeneous population of electrons with particle and internal energy densities that follow an inverse quadratic decay with respect to their distance from the apex of the compact jet. Thus, the heterogeneous population of electrons captured within a given resolution element form a superposition of single synchrotron spectra, with a radially variable turnover frequency. The frequencies that lie between the maximum and minimum are partially self-absorbed and the resulting spectral index flattens with respect to the self-absorbed value of $\alpha = 2.5$ (see Figure 1.4). Additionally, due to its significantly higher fractional polarization, the polarized emission is dominated by the

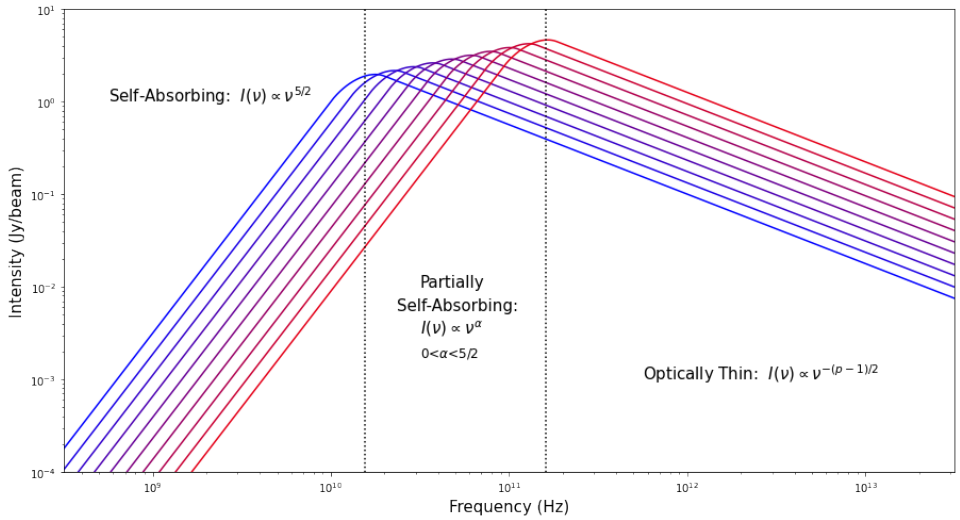


**Figure 1.4:** A schematic diagram of a partially self-absorbing synchrotron spectra for an power-law distribution of electrons. The dotted black lines separate the different emission regimes.

optically-thin bandwidth (Zdziarski et al., 2014). Hughes et al. (1985) proposed a shock-in-jet mechanism to produce a dominant magnetic field direction that similarly aligns the magnetic field direction perpendicular to the jet axis through a shock-compression front. However, there are some sources that appear to have a magnetic field direction perpendicular to the jet axis (e.g., M87; Laing 1980a) and are thought to be a result of velocity shearing at the edge of the jet (Laing, 1980b).

### 1.2.5 The Faraday Effect and Rotation Measure

As linearly polarized emission propagates through a magneto-ionic plasma it experiences a rotation of its polarization angle due to a process called Faraday rotation. The presence of such a plasma is ubiquitous throughout the observable universe (e.g., the $\sim \mu G$ magnetic field that threads the ISM; Haverkorn 2015). Faraday rotation is best understood through the deconstruction of any arbitrarily oriented linearly polarized waveform into the superposition of two orthogonal circular waves, whose phase difference defines the polarization angle. During propagation through any magneto-ionic plasma, the waves experience a

birefringence causing the two circular components to propagate with different phase velocities. As a result, their relative phases will continuously rotate as long as the radiation is within the plasma. Therefore, the observed linear polarization angle will be offset from its intrinsic value. The magnitude of the rotation is a function of the path length travelled, $d$, the strength of the magnetic field component parallel to the line of sight, $B_{\parallel}$, the number density of electrons contained with the plasma, $n_e$ and the wavelength of the emission, $\lambda$ (Lorimer and Kramer, 2012),

$$\Delta\psi = \frac{e^3\lambda^2}{8\pi^2 m_e^2 c^3}\int_0^d n_e B_{||} dl \tag{1.20}$$

Where $e$, $m_e$, and $c$ are the values of the elementary charge, the mass of an electron, and the speed of light, respectively. From here the rotation measure (RM) is defined as,

$$\mathrm{RM} = \frac{e^3}{8\pi^2 m_e^2 c^3}\int_0^d n_e B_{||} dl \tag{1.21}$$

It directly follows that the rotation measure is the slope of the linear relationship between the observed polarization angle, $\psi$, and the square wavelength of the emission,

$$\psi(\lambda^2) = \psi_0 + \mathrm{RM}\cdot\lambda^2 \tag{1.22}$$

Therefore, by measuring the polarization angle at a range of frequencies, the RM can be measured and the polarization angle can be de-rotated to its intrinsic value, $\psi_0$.

The total rotation (for a source within our Galaxy) will be the sum of the contributions from the ISM and any magneto-ionic plasma clouds local to the source environment. During transient events, variability in the observed RM or deviations from a baseline value are characteristic of an evolution in local

magnetic field or electron density distribution. Faraday rotation can also lead to depolarization of the observed emission if multiple lines of sight passing through different magneto-ionic plasma are contained within a resolution element or if a single line of sight has emission originating from a range of distances along it. This is a significant effect in many active galactic nuclei (AGN), although, it has also been seen within the spatially resolved observations of the BHXB SS 443 (Stirling et al., 2004; Miller-Jones et al., 2008).

## 1.3 V404 Cygni

Discovered in 1989, V404 Cyg (also named GS 2023+338) is a low-mass transient BHXB that has undergone four recorded outbursts. Of the four outbursts, two were caught in real time, the initial discovery with the Ginga satellite (Makino, 1989) and the most recent outburst discovered by the Burst Alert Telescope aboard the *Neal Gehrels Swift Observatory* (Barthelmy et al., 2015). Searches through historical photo plates identified that there were two additional outbursts in 1938 and 1956 (Richter, 1989). Observations of the main-sequence companion star revealed an orbital period of $6.47141 \pm 0.0001$ days and a mass function of $f(M) = 6.08 \pm 0.06\, M_{\odot}$ (Casares and Charles, 1994). The K spectral type of the companion star, coupled with near-infrared spectroscopy (and modelling of the H-band ellipsoidal modulations), infer a BH mass of $9.0^{+0.2}_{-0.6}\, M_{\odot}$ with a best fit orbital inclination angle of $67^{\circ\,+3}_{-1}$ (Khargharia et al., 2010). It should be noted that the modelled orbital inclination angle (and corresponding BH mass) assumes that the optical light curves have an accretion disk contamination of $\lesssim 3\%$; higher fractional contamination have been proposed and subsequent modelling has suggested inclinations far outside the predicted range (Tetarenko et al., 2017). High angular resolution radio parallax measurements determined a source distance of $2.39 \pm 0.14$ kpc(Miller-Jones et al., 2009), making it one of the closest known BHXBs and a superb laboratory for the study of accretion

physics.

On 2015 June 15 V404 Cyg went into its fourth recorded outburst. After its initial X-ray detection, a multi-wavelength follow-up campaign (radio through X-ray) showed bright flaring activity across all observing bands and V404 Cyg became the brightest BHXB outburst observed in the last decade, characteristic of an extremely high near-Eddington accretion rate. Towards the end of June the source began decaying, eventually reaching quiescence in mid-August, although the source showed brief periods of renewed activity in December (and January of the following year).

The data set analysed in this thesis was taken seven days following the initial detection and consists of a multi-frequency 4 hour long observation using the Karl G. Jansky Very Large Array (VLA) radio interferometer. During the observational coverage the source exhibited bright ($\sim$1 Jy) and rapid (minutes-hours) flaring activity. Simultaneous observations with the Very Long Baseline Array (VLBA) resolved several transient ejection events on top of a continuous (but variable) emission from a radio core (Miller-Jones et al., 2019). Whether the core is composed of an array of unresolved ejecta or a single steady jet is still to be seen, but the variability is characteristic of a rapidly evolving accretion environment.

# Chapter 2

# Observations

On June 22, 2015 the VLA observed V404 Cyg in an outbursting state between 11:18:12 and 14:38:06 UTC (project code: 15A-504). The multi-band observation – in both the C (4-8 GHz) and K (20-26 GHz) observing bands – were taken when the array was in its most extended A-configuration. To achieve simultaneity in both bands, the 27-element interferometer was broken into a 14-element (S1) and a 13-element sub array (S2). Each sub-array alternated between bands, switching $\sim 1/3$ and $\sim 2/3$ through the observations with S1 observing the sequence C-K-C and S2 observing K-C-K. The alternation ensured that a catastrophic failure of a single sub-array would not corrupt the entirety of a single bands data. The observations were temporally subdivided into $\sim$2 minute scans, with 88.0s on source and 28.0s on the phase calibrator during the bulk of the observing time (more about calibration in Section 2.2). Each antenna is equipped with an 8-bit sampler, separating each observing band into two 1.024 GHz basebands and each baseband is composed of 8 128.0 MHz spectral windows of 64 2.0 MHz channels. Henceforth, the C and K observing bands will be described by their 5/7 and 21/26 GHz basebands. Additionally, there were simultaneous observations taken at a central frequency of 15.6 GHz using the VLBA.

Unfortunately, even in its most extended A-configuration the VLA did not

have sufficient angular resolution to spatially resolve the relativistic jets of V404 Cyg, and the VLBA did not include any polarization information. As a result, spatially resolved polarimetry is not possible with these set of observations.

The following subsections will highlight some of the fundamentals of radio interferometry and synthesis imaging, and how it was applied to the data reduction and imaging of V404 Cyg. For all you could ever want to know (and more) about radio interferometry and synthesis imaging see Taylor et al. (1999).

## 2.1 Basics of Radio Interferometry

It's easiest to begin with the simplest configuration, the 2-element (single baseline) interferometer. Unlike optical observations, radio photons have insufficient energies to "eject" electrons from photoelectric material, inhibiting intensity measurements through photon counting apparati (e.g., CCDs). Instead, radio observations utilize the wave properties of light, measuring voltages induced across an antenna from the alternating electric field of the radio wave. For single aperture radio telescopes the intensities can be directly inferred from the amplitude of the induced voltages. However, radio interferometers measure the correlation of the input signals along the baseline connecting two spatially separated apertures. The input signals of the two antennae follow simple sinusoidal forms, $V_1(t) = v_1 \cos\left[2\pi\nu(t-\tau_g)\right]$ and $V_2(t) = v_2 \cos\left[2\pi\nu t\right]$ as does their correlation,

$$r(\tau_g) = \langle V_1(t) V_2(t) \rangle = v_1 v_2 \cos(2\pi\nu\tau_g) \tag{2.1}$$

Where $v_1 v_2$ is the fringe amplitude(directly proportional to the received power) and $\tau_g$ is a geometric phase delay resulting due to the spatial separation of the two antennae. The phase delay can be expressed as a function of the baseline separation, $\mathbf{b}$, and source position, $\mathbf{s}$, so that $\tau_g = \mathbf{b} \cdot \mathbf{s}/c$ (see Figure 2.1 for a schematic). Additionally, the fringe amplitude observed from a source

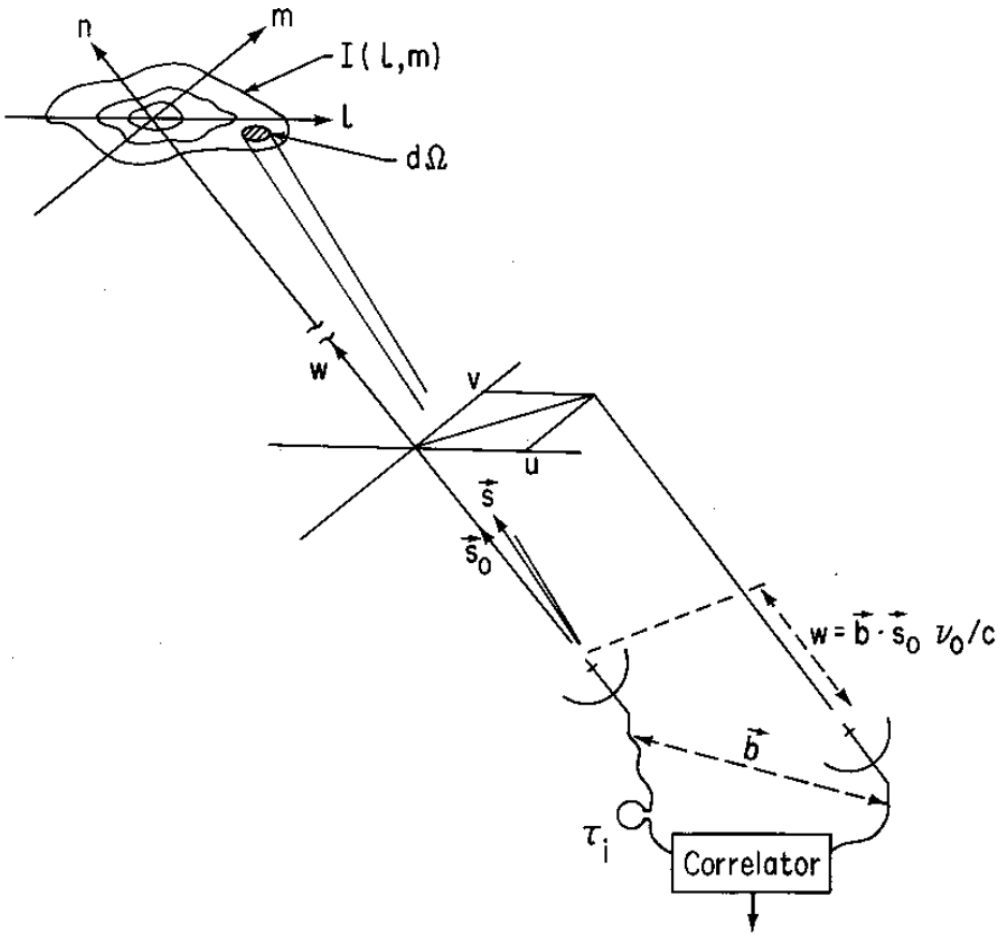


**Figure 2.1:** A schematic diagram of a 2-element interferometer, adopted from Taylor et al. (1999).

element of solid angle $d\Omega$ along the celestial sphere and an observing bandwidth $\Delta\nu$ is defined as $v_1 v_2 = A(\mathbf{s})I(\mathbf{s})\Delta\nu d\Omega$, for intensity $I(\mathbf{s})$ and antenna response pattern $A(\mathbf{s})$[1]. The correlator output can be found by integrating over all solid angles,

$$r = \Delta\nu \int_S A(\mathbf{s})I(\mathbf{s}) \cos \frac{2\pi\nu \mathbf{b}\cdot\mathbf{s}}{c} d\Omega \tag{2.2}$$

[1]The antenna response pattern describes the sensitivity of a single antenna as a function of source position, with a maximum sensitivity along the pointing direction. To understand the antenna response pattern it's useful to draw comparisons to the classic double slit experiment; the correlator output is analogous to the interference pattern between the two slits and the antenna response pattern is equivalent to the single-slit envelope that encases it.

Although this integral is taken over the entire celestial sphere, the response pattern falls to very low values outside of a small angular field, therefore the resulting output is confined to a small region of the sky. By defining a constant reference position or *phase center*[2], $\mathbf{s}_0$, the source direction can be rewritten with respect to the phase center, $\mathbf{s} = \mathbf{s}_0 + \boldsymbol{\sigma}$. Thus, the correlator output becomes,

$$\begin{aligned} r = \Delta\nu \cos\frac{2\pi\nu\mathbf{b}\cdot\mathbf{s}_0}{c}\int_S A(\mathbf{s})I(\mathbf{s})\cos\frac{2\pi\nu\mathbf{b}\cdot\boldsymbol{\sigma}}{c}d\Omega \\ - \Delta\nu \sin\frac{2\pi\nu\mathbf{b}\cdot\mathbf{s}_0}{c}\int_S A(\mathbf{s})I(\mathbf{s})\sin\frac{2\pi\nu\mathbf{b}\cdot\boldsymbol{\sigma}}{c}d\Omega \end{aligned} \tag{2.3}$$

From which, the **key** interferometric property is defined, the *complex visibility*;

$$V \equiv |V|e^{i\phi_V} = \int_S \mathcal{A}(\boldsymbol{\sigma})I(\boldsymbol{\sigma})e^{-2\pi i\nu\frac{\mathbf{b}\cdot\boldsymbol{\sigma}}{c}}d\Omega \tag{2.4}$$

Here, $\mathcal{A}(\boldsymbol{\sigma}) \equiv A(\boldsymbol{\sigma})/A_0$ is the *normalized* antenna response pattern (or primary beam) and $A_0$ is the response in the beam center. Through the substitution of the real and imaginary components of Equation (2.4) into (2.3) the correlator output can be rewritten with respect to the amplitude and phase of the complex visibility,

$$r = A_0\Delta\nu|V|\cos\left(\frac{2\pi\nu\mathbf{b}\cdot\mathbf{s}_0}{c} - \phi_V\right) \tag{2.5}$$

Following the coordinate system shown in Figure 2.1 the baseline vector and the source direction vector are replaced by their components $(u, v, w)$ and $(l, m, n)$ respectively. The components of the baseline vectors are conveniently expressed in units of the central wavelength of the observing band. The positions on the sky $l$, $m$ are direction cosines with respect to the $u$ and $v$ axes, and $n = \sqrt{1 - l^2 - m^2}$. By definition the $w/n$-components are selected so they point

[2]The phase center is the location along the celestial sphere where the complex visibility phase is defined as zero. For multi-baseline interferometers the phase is zero across all baselines.

towards the phase center. Expanding the dot products of Equation (2.4), the complex visibility becomes,

$$V(u,v,w) = \int_{-\infty}^{\infty}\int_{-\infty}^{\infty} \mathcal{A}(l,m)I(l,m)e^{-2\pi i\left[ul+vm+w(\sqrt{1-l^2-m^2}-1)\right]}\frac{dl\,dm}{\sqrt{1-l^2-m^2}} \tag{2.6}$$

For small-scale sources in close proximity to the phase tracking center, $w(\sqrt{1-l^2-m^2}-1) \sim 0$, and the dependence of the visibility on $w$ is negligible; an equivalent scenario would be an array of coplanar antennae ($w \sim 0$). Through these assumptions (2.6) simplifies to a two-dimensional Fourier transform and its inverse is the intensity distribution along the sky,

$$V(u,v) = \int_{-\infty}^{\infty}\int_{-\infty}^{\infty} \mathcal{A}(l,m)I(l,m)e^{-2\pi i(ul+vm)}dl\,dm \tag{2.7}$$

$$I(l,m) = \frac{1}{\mathcal{A}(l,m)}\int_{-\infty}^{\infty}\int_{-\infty}^{\infty} V(u,v)e^{2\pi i(ul+vm)}du\,dv \tag{2.8}$$

An interferometer will measure the response pattern, solve for the complex visibility phase/amplitude and then perform a Fourier transform to solve for the intensity distribution or *image* of the source on the projection of the sky.

It should be noted that the preceding description implicitly ignored the vector properties of electromagnetic radiation, treating the electric field as a scalar phenomenon. Fortunately, any arbitrary polarization can be represented as the superposition of two orthogonally polarized wavefronts. The full polarization information of a source is described by the four visibility pairs of two orthogonally polarized receivers; typical modern day interferometric antenna are equipped with two orthogonally polarized feeds[3] The matrix equation relating the different

[3]The VLA antenna have right and left hand circularly polarized feeds.

correlation pairs to the polarization properties can be seen below,

$$\begin{bmatrix} V_{RR^*} & V_{RL^*} \\ V_{LR^*} & V_{LL^*} \end{bmatrix} = \begin{bmatrix} V_I + V_V & V_Q + iV_U \\ V_Q - iV_U & V_I - V_V \end{bmatrix} \tag{2.9}$$

The subscripts in the left-hand matrix correspond to a given correlation between the feeds of two antenna; i.e $V_{RR^*}$ is the correlation function between the right-hand circularly polarized feed of one antenna and the complex conjugate of another. Equation (2.9) equates the measured visibilities to the visbilities of the source's Stokes parameters. The Stokes parameters are a particularly useful mathematical result that describes any arbitrary polarization state through a set of four fluxes. $I$ remains the total intensity and the other Stokes parameters describe the polarization state of the emission,

$$Q = If\cos 2\psi \cos 2\phi \tag{2.10}$$

$$U = If\sin 2\psi \cos 2\phi \tag{2.11}$$

$$V = If\sin 2\phi \tag{2.12}$$

and the fractional polarization, $f$, is defined by,

$$f = \frac{\sqrt{Q^2 + U^2 + V^2}}{I} \tag{2.13}$$

For negligible degrees of circular polarization, $\phi = V = 0$, $Q/U$ describe the linear polarization state with a linear polarization angle $\psi$; where, $\psi$ is the projection of the electric field vector on the sky and the quoted angle is measured east of north with a 180° degeneracy. A schematic diagram for an arbitrary polarization ellipse is presented in Figure 2.2.

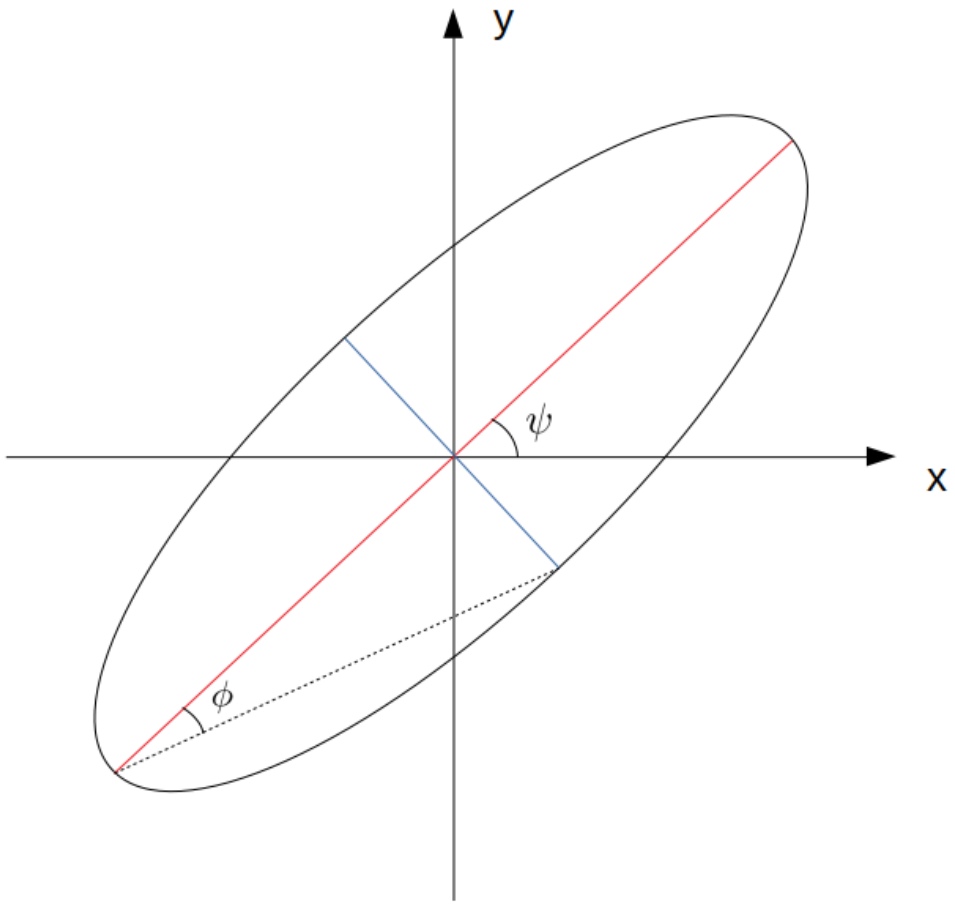


**Figure 2.2:** A schematic diagram of the polarization ellipse describing any arbitrary elliptical polarization.

## 2.2 Calibration and Editing

An unfortunate repercussion of the advancement of wireless technology is the prevalence of radio-frequency interference (RFI) originating from cellular devices, WiFi towers and other similar hardware. The construction of interferometers in remote locations and the enforcement of "radio-free" zones is effective in the minimization of RFI, but its complete removal is not possible. In addition to RFI, internal electronic failures can cause portions of the observed bandwidth to be irreparably corrupted. The identification and subsequent removal of these corrupted visibilities – through manual inspection or automated algorithms – is

termed *flagging*. In contrast, each observation will be subject to a number of correctable effects intrinsic to the interferometer or caused by the interactions between the incoming radiation and the Earth's atmosphere. These corrections are what is known as *calibration*. Calibration can be mathematically described as the solving for a complex gain term, $\mathcal{G}_{ij}$, that alters the measured visibilities $\widetilde{V}_{ij}$ with respect to the *true* visibilities $V_{ij}$, along the baseline connecting antenna $i$ and $j$;

$$\widetilde{V}_{ij}(t) = \mathcal{G}_{ij}(t)V_{ij}(t) + \epsilon_{ij}(t) + \eta_{ij}(t) \tag{2.14}$$

Where, $\epsilon_{ij}(\sim 0)$ and $\eta_{ij}$ are the complex offset and the stochastic noise respectively. The complex gain is approximated as the ratio of the true and observed visibilities, and solved for by assuming a model value for the true visibilities. These models are constructed through one of two methods; the utilization of standardized calibrators with known spectral properties and/or a self-calibration procedure where a bright source is used to iteratively improve a model of itself. Due to the rapid variability of the source self-calibration was not applied to the data and and will not be discussed any further.

An ideal calibrator will have simple amplitude and phase behaviour. The simplest morphologies are steady amplitude point sources at the phase center of the imaging plane so their visibilites have a constant amplitude and zero phase across the time and frequency domains. Atmospheric and electronic effects often exhibit a rapid temporal variability with timescales as short as a few minutes, and an angular inhomogeneity (only for atmospheric effects). Therefore, an ideal calibrator must have a line of sight similar to the source and be re-observed often enough to capture these short timescale effects effects. Finding a single calibrator that meets all of these criteria is extremely rare, so the calibration effects are corrected using multiple sources.

The primary or *Flux* calibrator is typically a bright ($\sim$1 Jy) non-variable source with well constrained spectral properties. It functions as an absolute scaling factor for the flux and a *bandpass* calibrator, identifying any artificial spectral features. The sparsity of primaries along the celestial sphere often results in large angular separations with respect to the target. Thus, the primaries are infrequently observed, inhibiting their ability to solve for short-timescale gain solutions. These effects are accounted for using secondary or *phase* calibrator(s) that also have stable visibilities but the addition of a similar line of sight as the source. If total intensity information is all that is desired these calibrators are all that is required. However, polarimetry has additional calibration effects; the correction of the absolute polarization angle and the removal of artificial polarization introduced by intensity *leakage* originating from the imperfect orthogonality of the antenna's feeds. Fortunately, the primary calibrator often has well constrained polarimetric properties and therefore can correct for any artificial rotation of the polarization angle and an unpolarized source can identify leakage. For these observations the primary was 3C48, the secondary was J2025+3343 and the leakage calibrator was J2355+4950[4].

All data reduction was performed with the Common Astronomy Software Application (CASA) and its included packages (McMullin et al., 2007). Initial flagging follows a standardized procedure ubiquitous to all VLA observations, which includes the removal of "dummy" scans[5], zero-amplitude data, shadowing[6] and unstable frequency channels at the edges of each spectral window. The remaining *advanced flagging* is observing run specific. Although variability of the phase and amplitude of the source are typical and physically reasonable effects in both the spectral and temporal domains, data that exhibited deviations

[4]Detailed information on the various VLA calibrators can be found at; `https://science.nrao.edu/facilities/vla/observing/callist`

[5]Dummy scans are used to configure the arrays, so their visibilities have no physical meanings.

[6]Shadowing is a dominant effect in compact array configurations where one antenna's dish will partially block an adjacent array. The VLA was in the most extended A-configuration during our observations reducing shadowing to a negligible effect.

that were irregularly large or sporadic were deemed RFI and flagged. Advanced flagging began with the implementation of the auto-flagging function `tfcrop`, a sigma-clipping routine effective at the removal of strong narrow-band RFI. The data were then visually inspected using CASA's visibility viewer `plotms` and any remaining (and noticeable) RFI was manually flagged. The data were reviewed once more post-calibration and any irregularities that appeared after calibration were subsequently removed and the data re-calibrated.

For calibration purposes the leakage and phase calibrators are point sources and do not require detailed spectral models to fulfill their respective purposes. However, the quality of the calibration is highly dependant on the accuracy of the primary model. CASA includes a repository of standardized total intensity models for many of the common primary calibrators, including 3C48. Each model is a spatially resolved intensity map at a single frequency that's extrapolated to the remainder of the frequencies through the flux scaling relationships from (Perley and Butler, 2017),

$$\log(S_\nu) = \sum_{n=0}^{N} a_n \log\left(\nu_{\mathrm{GHz}}\right)^n \tag{2.15}$$

The fit parameters, $a_n$ and $N$, were empirically determined from each primary's broadband intensity spectra. The function that is typically used to define the polarization model (`setjy`) implicitly assumes that the calibrator is a point source. However, the VLA was in an extended configuration and, as a result, the primary was slightly resolved. To account for potential resolution effects, a custom model image cube was constructed for each observing band, spanning the full bandwidth and containing information on all four Stokes planes. The model adopted the spatial distribution of the repository intensity maps, assuming it was uniform for all of the Stokes intensities. The $Q$ and $U$ fluxes were scaled according to Equations (2.10), (2.11) & (1.29), assuming an intrinsic

polarization angle of $\psi_0 = -58°$[7], a rotation measure of RM $= -68$ rad/m$^2$ and an ellipticity angle of $\phi \sim 0$ ($V \sim 0$). The fractional linear polarization of 3C48 varies with frequency; thus, it was modelled assuming the same functional form as Equation (2.15) and fit to the data presented in Perley and Butler (2013). The model fit and best fit parameters can be seen in Figure 2.3 and Table 2.1 respectively. Following the advice of the NRAO[8] staff, each radio band was fit independently — in contrast to the single broadband fit from Perley and Butler (2017) — as it is expected to improve the stability of the calibration solutions. The remainder of the calibration closely followed the approaches outlined in the CASA documentation[9].

[7]The reported value in Perley and Butler (2013) is 122° however the polarization has a 180° degeneracy, so was converted to fall within the typical range of $-90° \leq \psi_0 \leq 90°$.

[8]The National Radio Astronomy Observatory (NRAO) is the organization that operates the VLA and develops CASA.

[9]The CASA guide documentation contains a number of detailed guides on a variety of sources; `casaguides.nrao.edu/index.php/Karl_G._Jansky_VLA_Tutorials`.

| Quantity | Band | $a_0$ | $a_1$ | $a_2$ | $a_3$ |
|---|---|---|---|---|---|
| $S_\nu$ | C | 1.3253 | -0.7553 | -0.1914 | 0.0498 |
| | K | ” | ” | ” | ” |
| $f_\nu$ | C | -3.6323 | -1.6671 | 2.0709 | -0.5315 |
| | K | 3.6676 | -8.9995 | 3.7320 | -0.4767 |

**Table 2.1:** The 3$^{\text{rd}}$-order polynomial fits for the total intensity and the fractional polarization spectra of the primary calibrator.

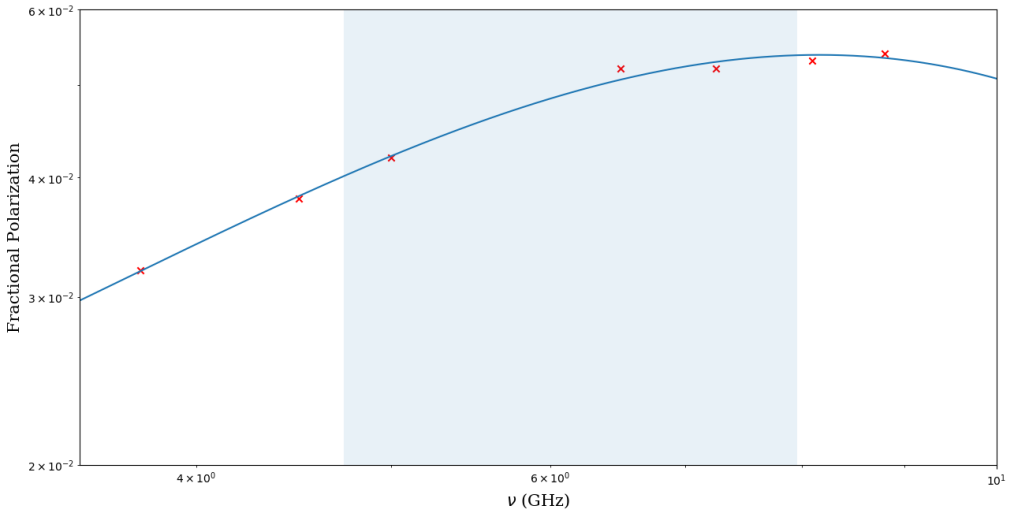


**(a)**

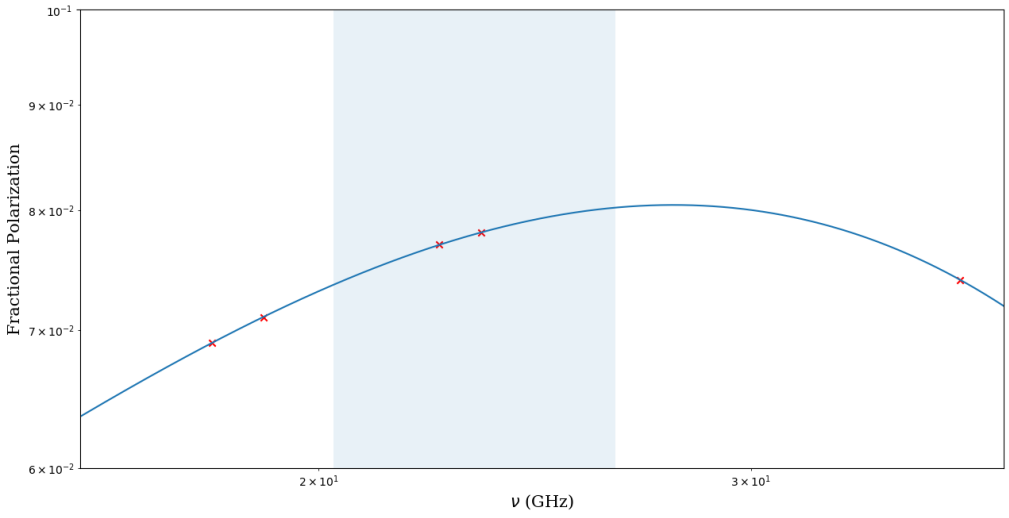


**(b)**

**Figure 2.3:** Fractional Polarization spectra of the primary calibrator for the; (a) 5/7 GHz and (b) 21/26 GHz radio bands. The shaded regions represent the range of frequencies spanned by each observing band.

## 2.3 Imaging

Equation (2.8) implicitly assumed a continuous coverage of the $uv$-plane. However, a $N$-element interferometer will only have $N(N-1)/2$ baselines (or $N(N-1)$ $uv$-pairs for a single frequency and *snapshot* in time). As a result, the *sampled* visibility distribution, $V_s$, is a product of the *true* distribution and a sampling function, $S(u,v)$,

$$V_s(u,v) = S(u,v) \cdot V(u,v) \tag{2.16}$$

In its simplest form, the sampling function is a sum of Dirac $\delta$-functions positioned at the sampled $uv$-pairs;

$$S(u,v) = \sum_{n=1}^{N} \delta(u-u_n, v-v_n) \tag{2.17}$$

The effects of finite sampling in the imaging plane are quantified through the application of convolution theory; i.e, for two functions $f$ and $g$, $\mathcal{F}[f \cdot g] = \mathcal{F}[f] * \mathcal{F}[g]$ (where $\mathcal{F}$ represents a Fourier transform). Thus, the observed or *dirty* image, $I_D(l,m)$, is a convolution of the Fourier transform of the sampling function or *dirty beam*, $B(l,m) = \mathcal{F}[S(u,v)]$, and the true image $I(l,m)$. The convolution effects manifest as bright artificial structures (commonly seen as sidelobes around bright sources) in the imaging plane with flux distributions defined by the shape of the dirty beam. The fundamental goal of synthesis imaging is the minimization and removal of the sampling effects, to reconstruct the true intensity distribution to as high an accuracy as possible. The "simplest" approach to reduce sampling effects is through an improved coverage of the $uv$-plane. In many cases waiting for large infrastructural projects to be approved is an inadvisable approach; instead, the improved coverage can be achieved by

imaging over larger intervals in frequency and time[10] at the cost of spectral or temporal resolution.

The dirty beam can also be "fine-tuned' to maximize specific scientific goals by replacing the simple sampling function with a weighted sampling function, $W(u, v)$,

$$W(u,v) = \sum_{n=1}^{N} K_n T_n D_n \delta(u - u_n, v - v_n) \tag{2.18}$$

where, $K_n$ quantifies the reliability of the $n^{\text{th}}$ visibility through trends in the local scatter of the data, unfortunately, there is little control over this parameter. The tapering function $T_n(u, v)$ is typically a separable, circularly symmetric function typically used to down weight visibility data at the outer edges of the $uv$-coverage, suppressing small scale sidelobes and increase the beamwidth. Lastly, the density function, $D_n$, assigns weights to each visibility as a function of the local data densities, where the classic weighting schemes are,

$$D_n = 1, \qquad \textit{natural weighting} \tag{2.19}$$

$$D_n = \frac{1}{N(n)}, \qquad \textit{uniform weighting} \tag{2.20}$$

here, $N(n)$ is defined as the number of data points within a symmetric region of the $uv$-plane centred on the $n^{\text{th}}$ visibility. Natural weighting weights all points equally and optimizes for signal-to-noise and uniform weighting sacrifices sensitivity to improve resolution. The hybrid or 'Briggs' weighting introduces a robustness parameter $R \in (2, 2)$ such that $R = 0$ gives a good trade off between the uniform ($R \sim -2$) and natural ($R \sim 2$) weighting schemes (Briggs, 1995). The small angular scale of V404 Cyg inhibited its resolution regardless of the chosen weighting scheme and, as a result, the weighting parameters were selected to optimize the sensitivity of the images; $T_n = D_n = 1$.

[10]The total baseline separation, $\sqrt{u^2 + v^2}$, will remain (roughly) constant with time, but the individual components will change with the rotation of the Earth.

Although the aforementioned improvements may reduce the effects of the dirty beam, deconvolution is almost always necessary to maximize image fidelity and detection significance. In astrophysics the predominant deconvolution routines are based off the CLEAN algorithm (Högbom, 1974). The deconvolution begins by locating the peak intensity value (or CLEAN component) in the dirty image. If there is *a priori* information about the emission region the search area for CLEAN components can be confined to a user-defined CLEAN "mask". Subsequently, the product of the dirty beam and a $\delta$-function at the position of CLEAN component (with an amplitude equal to a factor of $\sim 0.1$ times the intensity) is subtracted from the dirty image. The CLEAN component is also recorded in a separate "CLEAN image". This process continues for a user-defined number of iterations or until the peak intensity is below some chosen threshold intensity. At the end of the deconvolution the CLEAN image is convolved with an idealized "synthesized beam" (typically a 2-D Gaussian with dimensions set by the longest baseline(s) and the source's parallactic angle) and the residuals of the dirty image are added to the CLEAN image. The size and shape of the synthesized beam is what defines the smallest resolvable scales.

CASA's imager/deconvolver (`tclean`) is based on the Cotton-Schwab algorithm, separating the processes into major and minor cycles that handle the uniform gridding of the visibilities and deconvolution iterations respectively (Schwab, 1984). The motivation behind the uniform visibility re-gridding, is to allow for the use of fast Fourier transform algorithms that greatly improve computational efficiency. Each minor cycle is similar to a CLEAN cycle, with the addition of a secondary local stopping criterion[11] that initiates a transition to a major cycle. During a major cycle the intensity map is inversely Fourier transformed (back to visibilities), de-gridded and the CLEAN components are subtracted from the **ungridded** visibilities before returning to the imaging

[11] This criterion is either a fixed number of iterations or an automatically calculated intensity threshold. The automatic stopping criterion is typically defined as the iteration when the peak residual is equal to the intensity of the primary sidelobe of the brightest source.

| Baseband | $\nu_i$ | $\nu_f$ | $\Delta\nu$ | $\Delta t$ | $\sigma_{\rm RMS}$ | $\sigma_I$ | $\sigma_Q$ | $\sigma_U$ |
|---|---|---|---|---|---|---|---|---|
| 5 GHz | 4738 | 5762 | 1024 | 840 | ∼0.03 | ∼0.54 | ∼0.05 | ∼0.05 |
| | | | 2 | 840 | ∼0.51 | ∼0.92 | ∼0.57 | ∼0.57 |
| | | | 128 | 10 | ∼0.49 | ∼2.07 | — | — |
| 7 GHz | 6938 | 7962 | 1024 | 840 | ∼0.02 | ∼0.99 | ∼0.05 | ∼0.05 |
| | | | 8 | 840 | ∼0.22 | ∼1.24 | ∼0.32 | ∼0.32 |
| | | | 128 | 10 | ∼0.43 | ∼2.77 | — | — |
| 21 GHz | 20288 | 21312 | 1024 | 840 | ∼0.06 | ∼3.34 | ∼0.13 | ∼0.12 |
| | | | 128 | 840 | ∼0.16 | ∼3.17 | ∼0.30 | ∼0.31 |
| | | | 128 | 10 | ∼1.26 | ∼9.89 | — | — |
| 26 GHz | 25388 | 26412 | 1024 | 840 | ∼0.06 | ∼4.58 | ∼0.24 | ∼0.18 |
| | | | 256 | 840 | ∼0.10 | ∼4.54 | ∼0.37 | ∼0.32 |
| | | | 128 | 10 | ∼1.16 | ∼12.2 | — | — |

**Table 2.2:** Table of imaging properties. The central frequency of the lowest ($\nu_i$) and highest ($\nu_f$) channels and the imaging bandwidth ($\Delta\nu$) are reported in MHz. The temporal imagin window ($\Delta t$) is reported in seconds. Lastly, the theoretical thermal noise threshold ($\sigma_{\rm RMS}$) and the median noise values for each Stokes parameter ($\sigma_I$, $\sigma_Q$, $\sigma_U$) are reported in mJy. The theoretical noise estimates were calculated using the VLA exposure calculator; `obs.vla.nrao.edu/ect/`.

plane. The iterative gridding procedure introduces a gridding convolution function (GCF) that serves as the last tool that can be "tweaked" to better focus the data analysis procedure on the science goals of a given set of observations. Since V404 Cyg is a point source in close proximity to the phase tracking center, all baselines are adequately coplanar and a simple GCF (the default prolate spheroid with a 3×3 *uv*-pixel support size) was selected to maximize computational efficiency.

To address the science goals of this project, three *classes* of images where made; baseband averaged polarization images, narrow-band polarization images and high time resolution intensity images. The high time resolution images were made using the routine described in Tetarenko et al. (2017) and all others were made with a series of custom scripts. For the narrow-band imaging, the equispacing of the frequency channels caused the local $\lambda^2$ channel density to increase with an increasing central frequency. Potential biasing was avoided by scaling the frequency widths of each image to maintain an (approximately) constant $\lambda^2$ channel density across all 4 basebands.

The imaging properties summarized in Table 2.2 ubiquitously show elevated measured RMS noise levels compared to the (approximate) theoretical values. These effects are most significant in the total intensity (Stokes $I$) images and appear to worsen at higher central frequencies and larger imaging bandwidths. A slight increase in the measured noise is expected, as the theoretical estimators assume the utilization of the full bandwidth and time range, ignoring the flagging of channels and scans during editing and calibration. However, the magnitudes of the increases (in all images except the narrow-bandwidth Stokes $Q$ and $U$ images in the 5 GHz baseband) are much larger then can be explained by flagging effects. Potential sources of elevated noise include a result of imperfect visibility calibration (e.g., averaging of short time-scale phase variability), visibility averaging during imaging (e.g., spectral slopes/curvature in wide-bandwidth images), external sources (e.g., aliasing from bright sources outside the imaged field), or a combination of multiple effects. A generalized imaging script was run on a subset of images to see if the noise could be reduced. The script increased the imaging field to include the entire primary beam (but not multiple primary beams that also image the major sidelobes), implemented an iterative phase and amplitude self-calibration, included (when possible) Taylor terms to account for spectral variations in the CLEAN algorithm, and omitted source masking to CLEAN any remaining bright sources or artifacts and remove their sidelobes. In all test cases, this generalized approach reduced the measured RMS across all Stokes parameters by a factor $\gtrsim 10$ or within $\sim 20\%$ of the predicted theoretical value. No source brighter than $\sim 3$ mJy was detected, suggesting that neither bright sources nor artifacts were a primary issue. Despite the successful noise reduction, this routine greatly increases the computational requirements. For example, the number of pixels in each image was increased by a factor $\gtrsim 10$, becoming prohibitively large when considering the $\sim 23000$ images that are needed to perform the full analysis in this thesis. (This suite of $\sim 7$ test images took $\sim 10$ hours to run). Fortunately, the narrow-bandwidth images that are

utilized in the polarimetric analysis have median Stokes $Q/U$ noise values that are within a factor of $\sim$1.1, 1.5, 2, and 4 of the theoretical limit for the 5, 7, 21, and 26 GHz basebands, respectively. Furthermore, the majority of the polarimetric discussion was limited to the 5/7 GHz basebands (see Chapter 4), and therefore the elevated noise is expected to have a negligible effect on the derived polarization properties.

All fluxes were measured directly from the generated images. The Stokes $I$ fluxes were measured using the CASA task `imfit`, a routine that fits an elliptical Gaussian component to the image region. Since V404 Cyg is a point source the Gaussian fit adopted the shape of the synthesized beam. The narrow-bandwidth imaging coupled with V404 Cyg's intrinsically low fractional polarization resulted in peak magnitudes similar to (or in some cases below) the local peaks in the RMS noise for the Stokes $Q/U$ images. Therefore, attempts at direct fitting would either not converge or converge on local noise peaks. As a result, the $Q$ and $U$ values were measured from the total integrated flux within the same elliptical Gaussian region that was fit to the corresponding Stokes $I$ image (in both time and frequency).

The narrow-band images frequently revealed anomalous channels that were missed during flagging and calibration or corrupted by a systematic error native to one of the CASA functions. To correct for this, a $\sigma$-clipping routine was applied to the total intensity spectra at each time bin. The 21/26 GHz images were sufficiently broadband, that any rogue channels were smoothed over during frequency averaging, and therefore they were omitted from the $\sigma$-clipping. The routine began with the calculation of a residual standard deviation between the original 5/7 GHz data and a model. The model was a smoothed version of the original data and the smoothing filter was chosen to be a Gaussian with a standard deviation fixed at half the width of a spectral window. Any data point that was $> 3\sigma$ from the smoothed fit was flagged, the residual standard deviation was recalculated and the routine continued until the fractional difference in

residual standard deviations between the current and previous iteration was $\leq 1\%$. The frequencies of the channels that were removed from the total intensity spectra were recorded and subsequently removed from the $Q/U$ data as well. No further data manipulation was applied.

# Chapter 3

# Methods and Results

To understand the polarization state of V404 Cyg there are three key properties that needed to be analysed; the fractional polarization, the rotation measure and the polarization angle. In this Chapter I will describe the routines that were developed to extract those properties as well as the analysis of the temporal delays of the peak fluxes seen in the intensity light curves.

## 3.1 Peak Delays

The high time resolution intensity light curves for a central spectral window in each baseband are presented in Figure 3.1, each displaying a "three flare" morphology and a peak delay qualitatively consistent with the expected behaviour of a vdL plasmoid. Consider the case where the flares are a result of a single ejection event that maintains a constant magnetic field direction with time. The variable times of peak flux are a result of the delayed evolution of the optical depth in the lower frequency bands, therefore different segments of the bandwidth are subject to different local absorption conditions (i.e., higher/lower frequency will be optically thin/thick). As described in Chapter 1, the alignment of the polarisation angle with respect to magnetic field exhibits a 90° swing during the thick-to-thin transition; thus, if the peak delays are left uncorrected

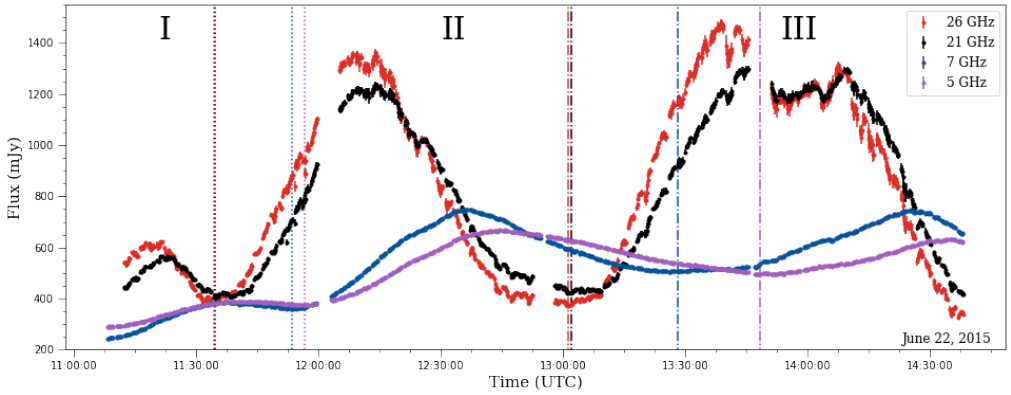


**Figure 3.1:** The intensity light curves, of the fourth spectral window, for each radio baseband binned into 10.0s intervals. The dotted lines (of equivalent color) highlight the I→II transition, and the dashed lines the II→III. The figure clearly highlights a ubiquitous tri-peaked temporal structure across all of the observing frequencies.

(in this highly idealized case) it will cause significant depolarization. This picture becomes more complicated in the presence of time dependent magnetic field directions or multiple unresolved jet components. In those cases, maintaining simultaneity may more accurately probe the intrinsic polarization properties. It's unclear which of these two prescriptions is preferable for the analysis of V404 Cyg's 2015 outburst, so the polarimetric analysis was applied to both peak delay corrected and uncorrected data.

The original intensity modelling of the VLA data (Tetarenko et al., 2017) and the spatially resolved VLBA observations (Miller-Jones et al., 2019) showed that the observed light curves are a superposition of the emission from $\geq$8 bi-polar ejecta in addition to a compact core. The insufficient spatial resolution of the VLA observations inhibited the disentanglement of the contributions from the individual components; therefore, the temporal divisions were simplified by breaking the light curve into only three segments, one for each of the three major flaring structures. The transitional times were defined as the time of minimum flux in each of the two "troughs" and are shown by the vertical dotted or dashed lines in Figure 3.1. Although this simple treatment will undoubtedly introduce biases/errors, the current iteration of the peak delay correction serves as an introductory investigation into its effects.

Each peak delays had been measured from the cross-correlation function (CCF) between the light curves of two spectral windows. Each CCF was generated using the z-transformed discrete correlation function (ZDCF) techniques of Alexander (1997)[1]. The delay binning was fixed at the temporal resolution (10.0s); following the recommendation of the developer, the 0s delay bin was omitted. The uncertainty on the best fit delays are typically measured through a maximum likelihood estimator. The estimator calculates the uncertainty from the 68% fiducial interval around the maximum of the normalized likelihood function (`PLIKE`; see Alexander 2013 for more details). However, the algorithm seemed to randomly diverge — appearing to be more unstable for small delays — so the error was instead estimated using a Monte Carlo re-sampling routine. Assuming Gaussian errors, each light curve was re-sampled 1000 times, generating 1000 CCFs for each spectral pairing (See Appendix C for the histograms of each delay distribution). The best fit delays were taken to be the median value and the $+/-$ uncertainties as the range between the median and the $85^{\text{th}}/15^{\text{th}}$ percentile. The uncertainties associated with the Monte Carlo sampling intervals are consistently (and significantly) low when compared to the instances when `PLIKE` converged, suggestive of a systematic underestimation of the delay uncertainty by the Monte-Carlo re-sampling routine.

The highest frequency spectral window in the bandwidth of interest was fixed as the reference in all of the generated CCFs. The polarimetric analysis was applied to both the full bandwidth ($\nu_{\text{ref}} \equiv 26.347$ GHz) and the lower frequency 5/7 GHz basebands ($\nu_{\text{ref}} \equiv 7.897$ GHz) and, as a result, the peak delays were measured with respect to both reference frequencies. The CCFs between 5/7 GHz and 21/26 GHz spectral windows displayed a peculiar oscillatory behaviour around the global maximum (see the inset of Figure 3.2). The measured delays were discretized in the frequency domain, a result of the transition from one local maximum to another. Absent any reasonable physical explanation, the

[1]FORTRAN code available at;
`http://www.weizmann.ac.il/particle/tal/research-activities/software`

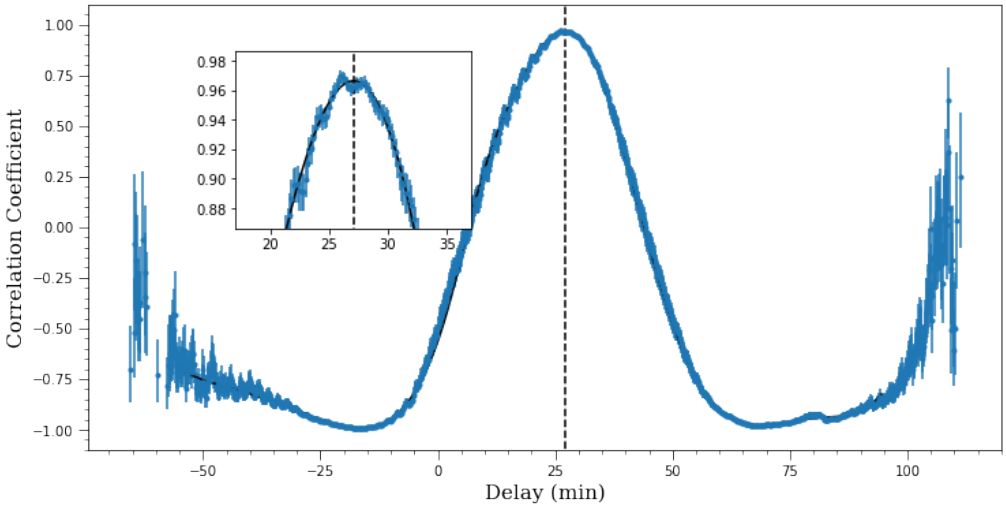


**Figure 3.2:** The cross-correlation function between the spectral windows with central frequencies of $\nu_c = 7.897$ GHz and $\nu_c = 26.347$ GHz for flare II. The sampled points are in blue and the smoothed fit is seen in black. The inset displays a zoomed view of the peak region, highlighting the oscillatory substructure produced by the ZDCF.

substructure was presumed to be an artifact introduced by the ZDCF algorithm and subsequently removed through an empirically motivated smoothing routine. Utilizing the interpolation functionality of `scipy`, each CCF was fit (and smoothed) with a $4^{\text{th}}$–order spline. The adjustable smoothing parameter was iteratively increased until the small–scale oscillations were smoothed over and the large–scale structure of the peak remained largely unaffected. The simple analytical form of a spline interpolation function (i.e., a piecewise polynomial) allowed for the direct computation of each fit's critical points. The measured delays were taken to be the position of the global maximum of the spline fit.

The derived delays were applied during imaging using a custom script that shifted the imaging window backwards in time by the magnitude of the measured delay for the nearest spectral window. For imaging bandwidths less than 1.024 GHz this procedure introduced a (minor) systematic error by ignoring the changes within a spectral window. However, the maximum intra-spectral window delay was $\sim$1 minute, significantly smaller than the temporal imaging window. Tests that applied a linear interpolation between the measured

delays, had negligible differences when compared to the implemented imaging routine. Therefore, the temporal averaging by the imaging window dominated any systematic introduced by the assumption of uniform delays across each spectral window. The measured delays for each flare (with respect to each reference frequency) are presented in Figure 3.3.

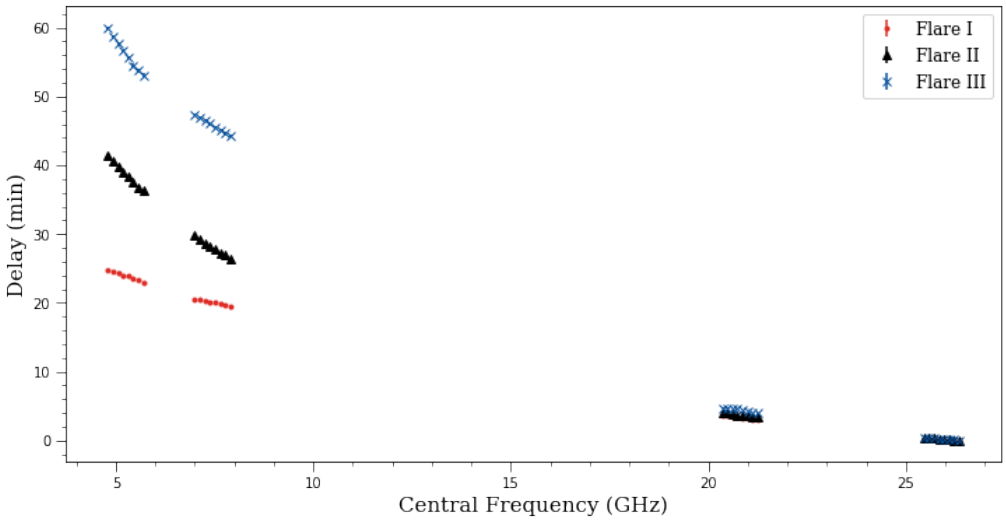


**(a)**

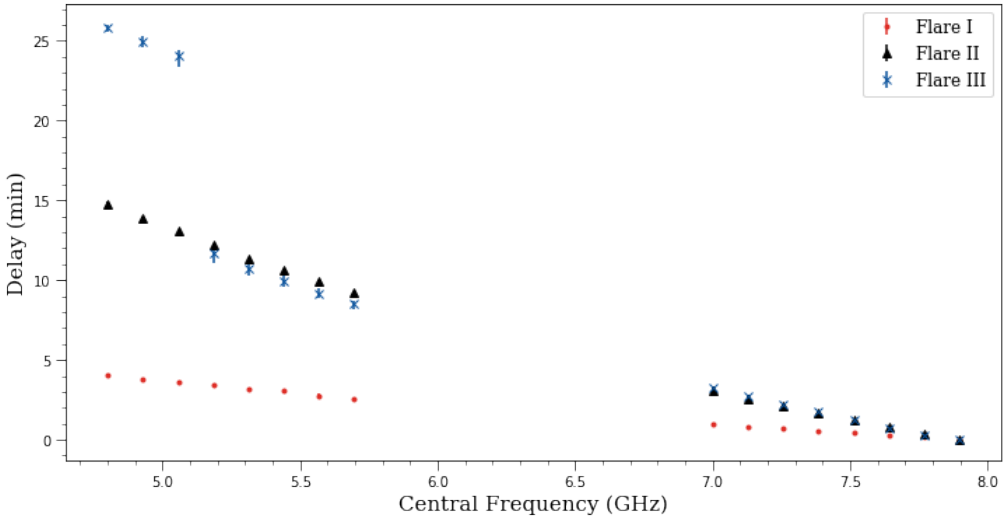


**(b)**

**Figure 3.3:** The measured delays for; (a) The full bandwidth ($\nu_{\rm ref}$ = 26.347 GHz) and (b) The 5/7 GHz ($\nu_{\rm ref}$ = 7.897 GHz) limited light curves.

## 3.2 Polarimetry

Two independent techniques were used to extract the polarization angle (both intrinsic and observed) and the rotation measure from the observations; a powerful Fourier technique, *Rotation Measure Synthesis*, and a custom model that implemented a Markov Chain Monte Carlo (MCMC) algorithm.

### 3.2.1 Rotation Measure Synthesis

Faraday rotation measure synthesis is a Fourier technique that probes the polarization properties of a source through the transformation of typical polarimetric observations into a complex Faraday dispersion function (Burn, 1966; Brentjens and de Bruyn, 2005). The input of any RM synthesis routine is an ensemble of Stokes $Q$, $U$ and $I$ values corresponding to $N$ (unique) spectral channels. Each spectral channel has its polarization properties described by through complex linear polarization, $P(\lambda^2) = Q(\lambda^2) + iU(\lambda^2)$. The RM synthesis algorithm derotates the ensemble of complex linear polarizations across a range of trial RMs (or *Faraday depths* $\phi_f$) to the value at the weighted average of the $\lambda^2$ channels,

$$\lambda_w^2 = K \sum_{j=1}^{N} w_j \lambda_j^2 \quad \& \quad K = \left( \sum_{j=1}^{N} w_j \right)^{-1}. \tag{3.1}$$

Typically (as is the case in the following analysis), the spectral channels are assigned inverse variance weights, $w_i = 1/\sigma_{QU}^2$, for $\sigma_{QU} \approx (\sigma_Q + \sigma_U)/2$. Following the derotation, the complex polarizations are summed along the spectral axis at each value of $\phi_f$. The resulting summations are known as the complex Faraday dispersion function (FDF),

$$\widetilde{F}(\phi_f) = K \sum_{j=1}^{N} \widetilde{P}(\lambda_j^2) e^{-2i\phi_f(\lambda_j^2 - \lambda_w^2)}. \tag{3.2}$$

The leading factor of $K$ is a result of the sampling effects caused by incomplete $\lambda^2$-coverage. The true FDF, $F(\phi_f)$, is a convolution of the observed FDF and a sensitivity function, $R(\phi_f)$,

$$\widetilde{F}(\phi_f) = F(\phi_f) * R(\phi_f), \tag{3.3}$$

$R(\phi_f)$ is known as the rotation measure synthesis function (RMSF), and is computed as follows,

$$R(\phi_f) = K \sum_{j=1}^{N} w_j e^{-2i\phi_f(\lambda_j^2 - \lambda_w^2)}. \tag{3.4}$$

The RMSF is analogous to the dirty beam in the context of synthesis imaging, introducing artificial peaks in the FDF that are subsequently minimized through the implementation of a CLEAN algorithm.

Suppose that along a given line of sight there is a single source of linearly polarized emission subject to a rotation by Faraday dispersion. At the true Faraday depth, $\phi_{\rm RM}$, the derotated complex polarizations have been aligned and the summation of the spectral channels is coherent. The result is a significant peak in the FDF at the position of the true Faraday depth. Conversely, at all other $\phi_f$ channels the inaccurate derotation will maintain the incoherent summation and define the underlying noise structure. The magnitude of the FDF peak is equivalent to the de-rotated linear polarization intensity and the observed polarization angle (at $\lambda_w^2$) is defined by the ratio of its real and imaginary components,

$$\psi_w = \frac{1}{2} \arctan\left(\frac{\mathrm{Im}[F(\phi_{\rm RM})]}{\mathrm{Re}[F(\phi_{\rm RM})]}\right). \tag{3.5}$$

If the signal-to-noise ratio (S/N) is sufficiently high, the polarization angle can be further derotated to its intrinsic value at $\lambda^2 = 0$ using Equation (1.22).

If there are multiple sources along the line of sight the FDF will have multiple statistically significant peaks; thus, the measuring of RM(s) and intrinsic polarization angle(s) has been reduced to the location of these peaks.

It follows from the coherent summation that the significance of a RM synthesis detection is limited by the band averaged S/N ratio rather than the much lower channelized S/N. The historical techniques for measuring polarization properties involved the linear fitting of the $\psi$–$\lambda^2$ relationship. However, $Q$ and $U$ share a non-linear relationship with $\psi$ that inhibits the use of low S/N channelizations. Thus, RM synthesis is an extraordinarily powerful technique when applied to weakly polarized sources, multi-component lines of sight or sources with extreme RM values that require maximal spectral resolution. Empirical analyses have constrained the significance threshold to occur at a band averaged S/N $\gtrsim 7$ (in the imaging plane) (Brentjens and de Bruyn, 2005; Macquart et al., 2012). Any RM synthesis experiment is dependent on two primary length scales; the Faraday depth that corresponds to a sensitivity drop $\sim 50\%$ and the FWHM of the central peak of the RMSF. The latter — similar to a synthesized beam — defines the resolution limit in Faraday space and is a function of the total width of the $\lambda^2$ coverage (c.f. the longest baseline in Synthesis imaging),

$$\text{FWHM} \sim \frac{2\sqrt{3}}{\Delta\lambda^2}. \tag{3.6}$$

Conversely, the other scale is characteristic of the largest resolvable Faraday depth, and is governed by the spectral channelization,

$$||\phi_{\max}|| \sim \frac{\sqrt{3}}{\delta\lambda^2}. \tag{3.7}$$

For this experiment the generated FDFs were defined to span a range of Faraday depths defined by the characteristic length scale presented in Equation (3.7). The uneven sampling resulted in a range of $\delta\lambda^2$ values. To reduce the effects of any potential aliasing from high RM sources, the maximum value

was chosen corresponding to $\phi_{\rm max} \sim 9 \times 10^5$ rad m$^{-2}$. This value remained consistent for both the full bandwidth and 5/7 GHz data. The $\phi_f$ channel size was defined using typical centroiding accuracy, $\delta\phi_f \sim {\rm FWHM}/(2 \times {\rm S/N})$, and adopting a median value of S/N $\sim$ 10. There is a slight reduction in $\lambda^2$ bandwidth from the omission of the 21/26 GHz basebands, and as a result, an increase in the FWHM from $\sim$1000 rad m$^{-2}$ to $\sim$1500 rad m$^{-2}$. Therefore, the Faraday depth channel widths were 50 and 75 rad m$^{-2}$ for the full bandwidth and the 5/7 GHz observations respectively.

The scripts used for the RM Synthesis analysis were developed by CIRADA and can be found in the CIRADA-Tools package `RM-Tools`[2]. The standard RM synthesis routine exclusively solved for the highest S/N component exclusively, and therefore, to account for the presence of multiple components, the script was modified so that it located all peaks in the FDF that exceeded a $5\sigma_{\rm RM}$ threshold. The chosen metric to quantify the noise was the root-mean-square of the Faraday dispersion function after a masking $\pm$2FWHM around the central maximum. Following the basic routine, each peak was fit with a three-point parabolic interpolation, adopting the fit values as the polarization intensities and rotation measures and reducing any pixel discretization errors (Hales et al., 2012). To help the reader visualize a typical FDF, a sample is provided for a single time range in Figure 3.4.

[2]The Github repository can be found here:
`https://github.com/CIRADA-Tools/RM-Tools`

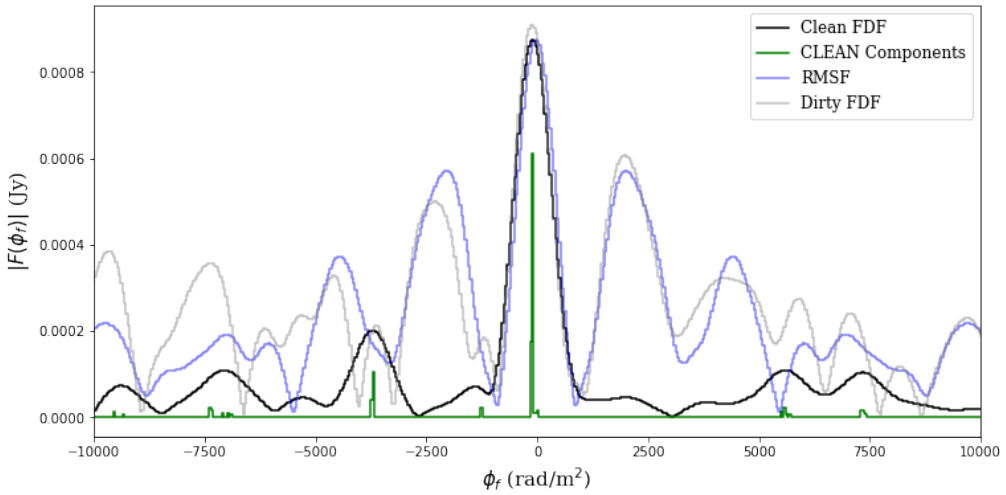


**(a)**

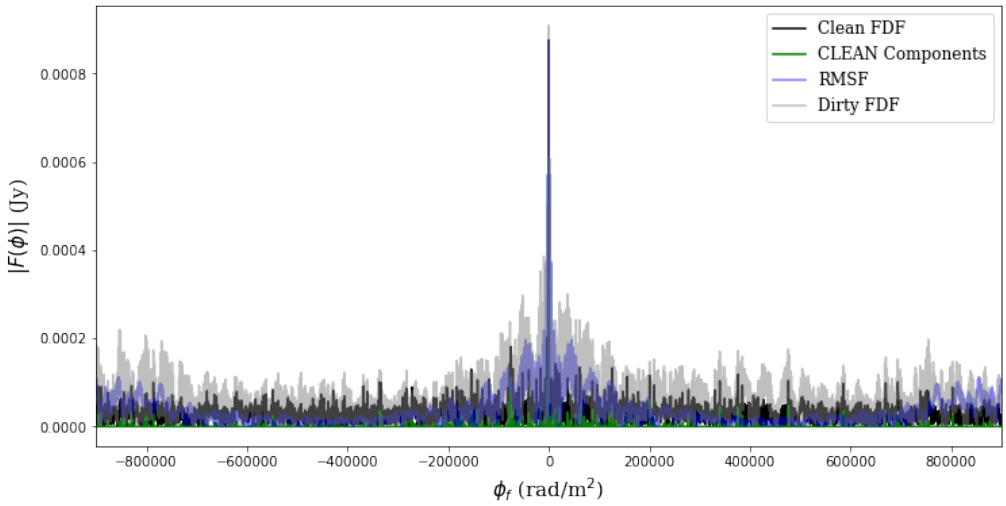


**(b)**

**Figure 3.4:** A full bandwidth Faraday dispersion function for the time bin between 12:04:00–12:18:00 (absent any delay correction). The $\phi_f$ ranges of the two figures are; (a) $\pm 10$ FWHM about the central maximum and (b) the full Faraday depth range of $\pm 9 \times 10^5$ rad m$^{-2}$.

### 3.2.2 Bayesian Modelling

To complement the RM synthesis results, and help identify any potential systematics, an alternative polarimetric routine was developed using a simple Bayesian forward model that fit the polarization parameters directly to the unmodified observations. The Bayesian approach was a Markov-Chain Monte Carlo (MCMC) algorithm implemented through Python's `EMCEE` package. `EMCEE` is a pure-Python implementation of Goodman and Weare's Affine Invariant Markov chain Monte Carlo Ensemble Sampler (Foreman-Mackey et al., 2013; Goodman and Weare, 2010); a modified version of the classic Metropolis-Hastings algorithm, simultaneously evolving a select number of *walkers* through parameter space. The number of (accepted) walkers was fixed at five times the number of dimensions, 20. To remain consistent with RM synthesis the fitting functions solved for the polarization angle at $\lambda_w^2$, $\psi_w$. The rotation measure and polarization angle were related to the observed polarized fluxes by combining Equations (1.29), (2.11) and (2.12) and assuming a negligible degree of circular polarization,

$$\widetilde{Q} = If \sin\left[2\psi_w + 2\mathrm{RM}(\lambda^2 - \lambda_w^2)\right], \quad \text{and} \tag{3.8}$$

$$\widetilde{U} = If \cos\left[2\psi_w + 2\mathrm{RM}(\lambda^2 - \lambda_w^2)\right]. \tag{3.9}$$

It should be noted that Equation (3.8) and (3.9) implicitly assume a single Faraday component and, as a result, the Bayesian modelling is incapable of distinguishing between single and multi-component lines of sight. To construct the likelihood function ($\mathcal{L}$) the sampled $Q/U$ fluxes were assumed to be independently distributed normal random variables such that the log-likelihood

function follows,

$$\log \mathcal{L} = -\sum_{j=1}^{N} \left[ \log \sqrt{2\pi\widetilde{\sigma}_{Q,j}^2} + \frac{(Q_j - \widetilde{Q}_j)^2}{2\widetilde{\sigma}_{Q,j}^2} + \log \sqrt{2\pi\widetilde{\sigma}_{U,j}^2} + \frac{(U_j - \widetilde{U}_j^2)}{2\widetilde{\sigma}_{U,j}^2} \right]. \tag{3.10}$$

The tildes denote the model parameters. The variances seen in Equation (3.10) are summations of the measured RMS noise in the imaging planes and an additional variance term that accounts for any missed systematic effects; i.e., elevated scatter from the proximity of the flux to the noise threshold in the narrow-band images. The systematic variances compose the final two fitting parameters, with a single variance per $Q/U$ spectrum. In the current version of the Bayesian modelling, the total intensity ($I$) and linear fractional polarization ($f$) aren't directly fit, instead their models are approximated by passing the original data though a Gaussian smoothing filter, retaining the overall structure while removing small-scale stochastic variability. In followup work, a physically motivated spectral fit (e.g., a power-law or broken power-law) will be included as model parameters.

All four priors were selected to be broad, uniform and uninformative to accurately reflect the lack of *a priori* information on V404 Cyg's polarization state. Additionally, the walker starting positions were distributed uniformly across the prior range. The positive definite systematic variances had a maximum value set as twice the sample variance of their corresponding Stokes parameters, and thus the prior is time bin dependent. The rotation measure of the prior was defined as $\pm||\phi_{\max}||$ to remain consistent with the corresponding FDF spectra. A uniform prior was unable to capture the circularity of the intrinsic polarization angle. As a result, individual walkers frequently become trapped in the local minima created by the prior's edges, which subsequently inhibited convergence. The prior was expanded to include $\pm 3\pi/2$, while maintaining the initial condition distribution that spanned the physically meaningful range of

$\pm\pi/2$. Additionally, each run was initialized with 40 walkers, twice the number intended for sampling. Following an initial set of "burn-in" iterations, half of the walkers with the lowest posterior probabilities were truncated and the remainder were run through a second set of "burn-in" iterations before sampling. The median of each posterior distribution was adopted as the modelled value and the ranges between the median and the $15^{\text{th}}$/ $85^{\text{th}}$ percentiles defined the $(-)/(+)$ uncertainties. The MCMC results for the same time bin as Figure 3.4 are presented in Figure 3.5.

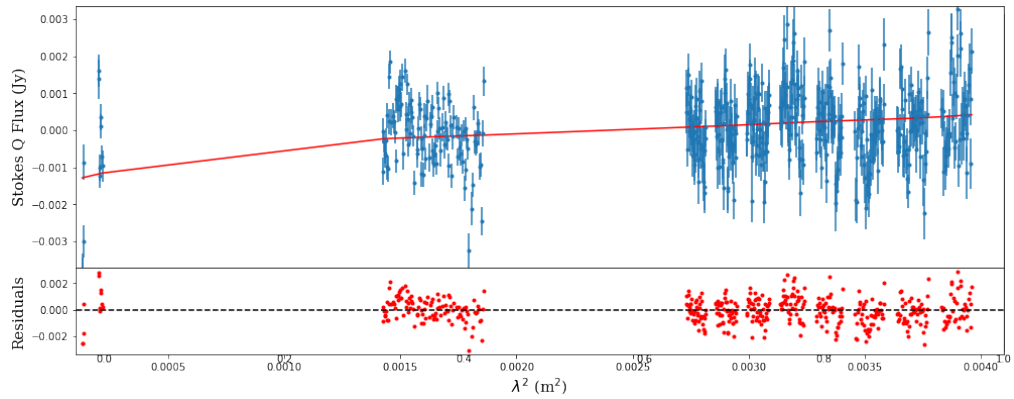


**(a)**

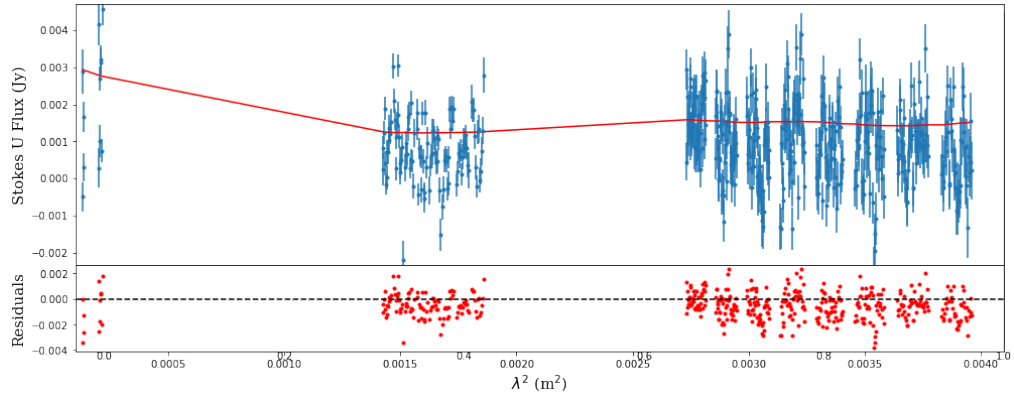


**(b)**

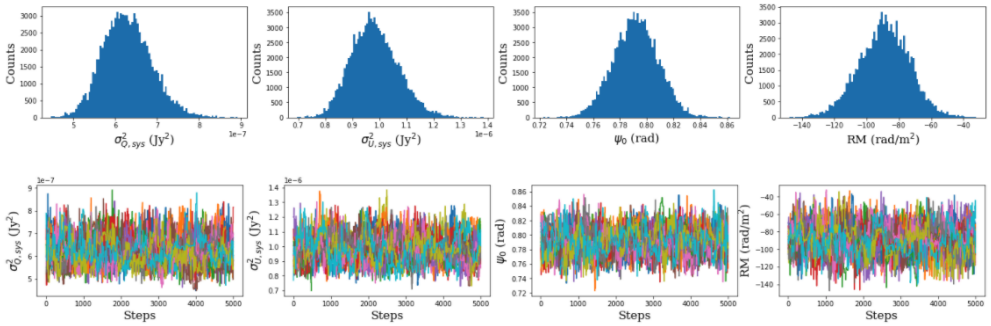


**(c)**

**Figure 3.5:** MCMC modelling of the full bandwidth observations between 12:04:00-12:18:00. (a) The Stokes Q data (blue) with the best fit model over-plotted (red). (b) The Stokes U data (blue) with the best fit model over-plotted (red). (c) Posterior distributions (upper) and walker paths for the sampling iterations (lower) for each model parameter.

## 3.3 Fractional Linear Polarization

The fractional linear polarization was derived from the baseband averaged total intensity and the linear polarization intensity maps ($P = \sqrt{Q^2 + U^2}$) for each time bin. Since $P$ is a non-negative quantity, the noise inherently present in the $Q$ and $U$ maps will result in a positive value even if no signal exists. Therefore, the observed linear polarization intensity will be biased, increasing its value with respect to the true or intrinsic signal $P_0$. For those curious, the statistics of $P$ with respect to its true signal $P_0$ and noise value $\sigma_{QU}$ are given by the Ricean distribution of Rice (1945). As a result, the linearly polarized intensity was debiased using the correction from George et al. (2012),

$$P_0 = \sqrt{P^2 - 2.3\sigma_{QU}^2}, \tag{3.11}$$

where once again $\sigma_{QU} \approx \frac{1}{2}(\sigma_Q + \sigma_U)$[3]. The linear polarization fraction was then defined as $f = P_0/I$ and the uncertainty was approximated by addition through quadrature,

$$\frac{\sigma_f^2}{f^2} \approx \frac{\sigma_{QU}^2}{P_0^2} + \frac{\sigma_I^2}{I^2}. \tag{3.12}$$

The fractional polarization *light curves* for the baseband averaged images are presented in Figure 3.6. It should be noted that although the averaging will result in a degree of bandwidth depolarization due to internal Faraday rotation, for a typical derived rotation measure of $\sim -200$ rad m$^{-2}$ the decrease in fractional polarization is $\lesssim 2\%$[4]. The low values of the intrinsic fractional linear polarization approach the predicted level of spurious linear polarization (that are

[3]This equation was adopted to remain consistent with the RM Synthesis routine. The values of $\sigma_Q$ and $\sigma_U$ correspond to the measured RMS noise of the corresponding Stokes $Q$ and $U$ images.

[4]The quoted 2% value is relative to the intrinsic fractional polarization, it is not to be confused with an absolute value.

a result of imperfect leakage calibration). These effects were quantified in Hales (2017) (see Equation A9) who suggested that the spurious linear polarization follow a Rayleigh distribution. The estimated mean spurious linear polarization fractions are 0.062/0.069/0.28/0.34% for the 5/7/21/26GHz basebands. The horizontal dashed lines overplotted on Figure 3.6 represent the probability that a $f$ detection at that value corresponds to a real signal.

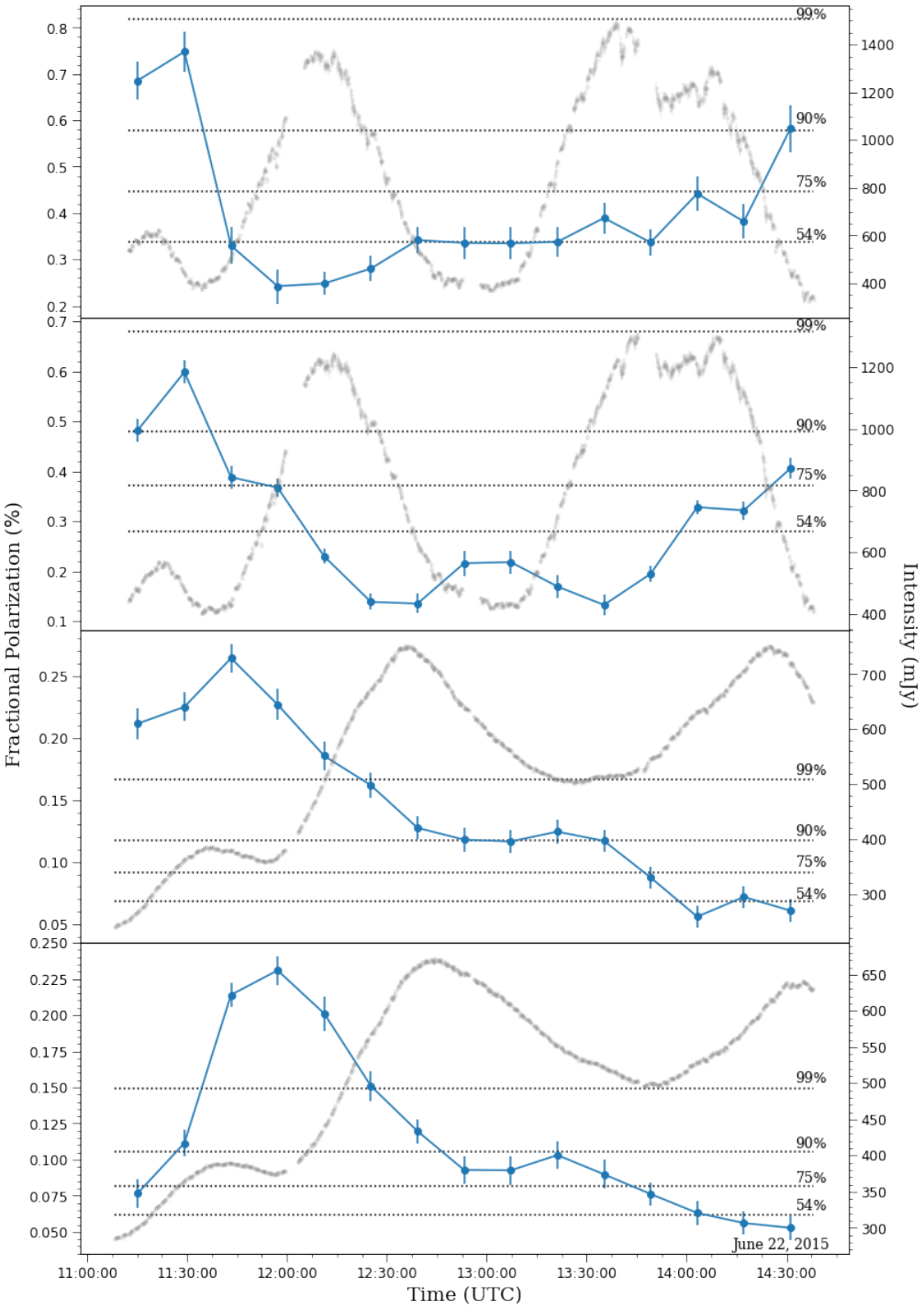


**Figure 3.6:** Fractional polarization (blue) and intensity (grey) as a function of time. Each panel represents a different baseband; 26 GHz (top), 21 GHz (2$^{nd}$ from the top), 7 GHz (3$^{rd}$ from the top), 5 GHz (bottom). The horizontal lines are the fractional polarization that corresponds to the detection significance seen on the right hand side of the plot.

## 3.4 Results

The following plots highlight the key results utilized during the interpretations of the polarization evolution presented in Chapter 4. For each figure only the dominant component of each FDF was plotted as it is likely the only significant detection (see Appendix A for the complete data tables).

The grey-scale regions associate the time bins with the 99, 90, and 75% significance levels of the 5 GHz observations presented in Figure 3.6. The darker the region the more significant the detection.

The vertical dotted line highlights the transitional time between flare I and flare II. In the delay corrected curves the data to the left/right of the dotted line had were corrected for the I/II peak delays.

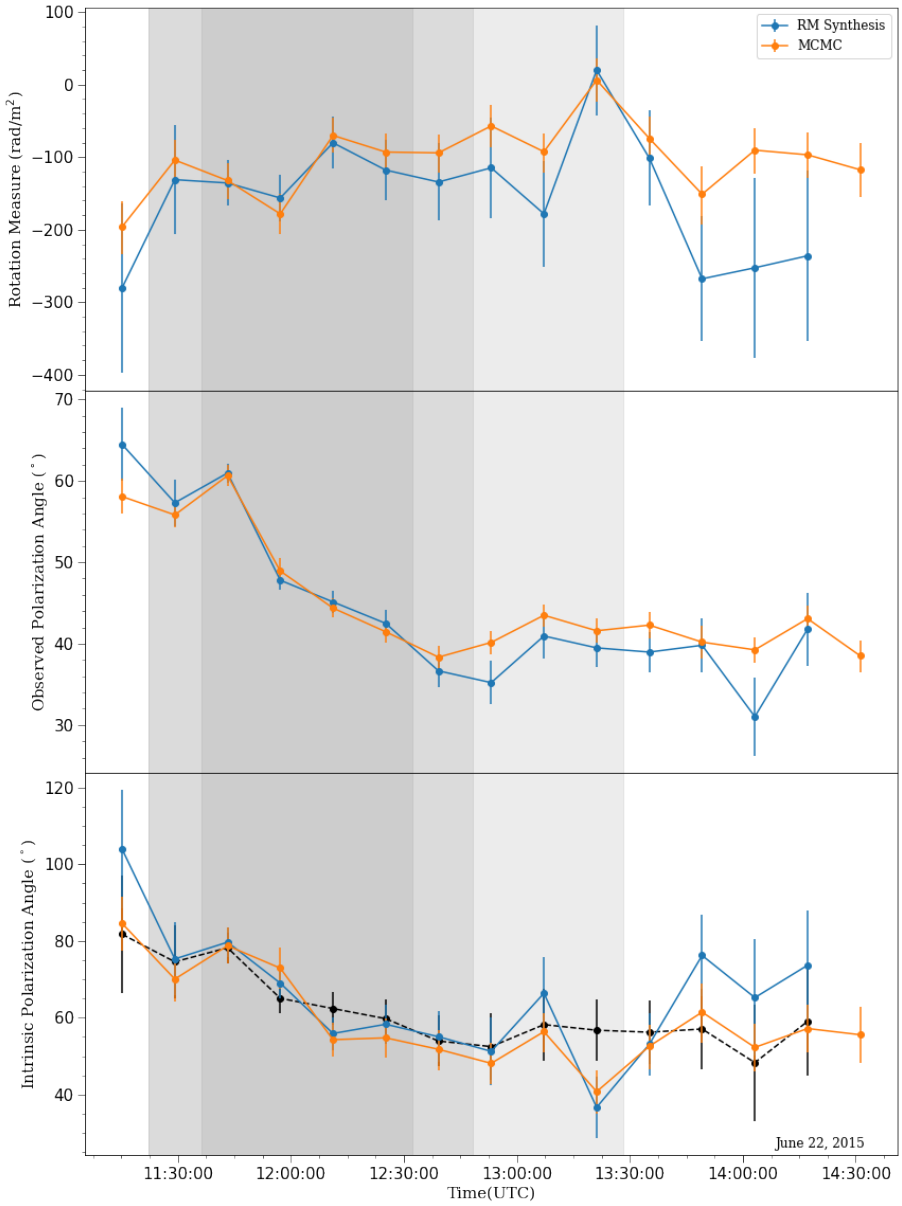


**Figure 3.7:** Polarization properties of the 5/7 GHz data, without the application of a peak delay correction for both the MCMC and RM synthesis routines. The shaded regions represent the 99, 90, and 75% significance regions for the 5 GHz observations (the darker shade the more significant). The dotted black line in the lower panel corresponds to the intrinsic polarization angle if the rotation measure is assumed to be a constant value equal to the weighted mean of the RM Synthesis results within the 99% significance interval.

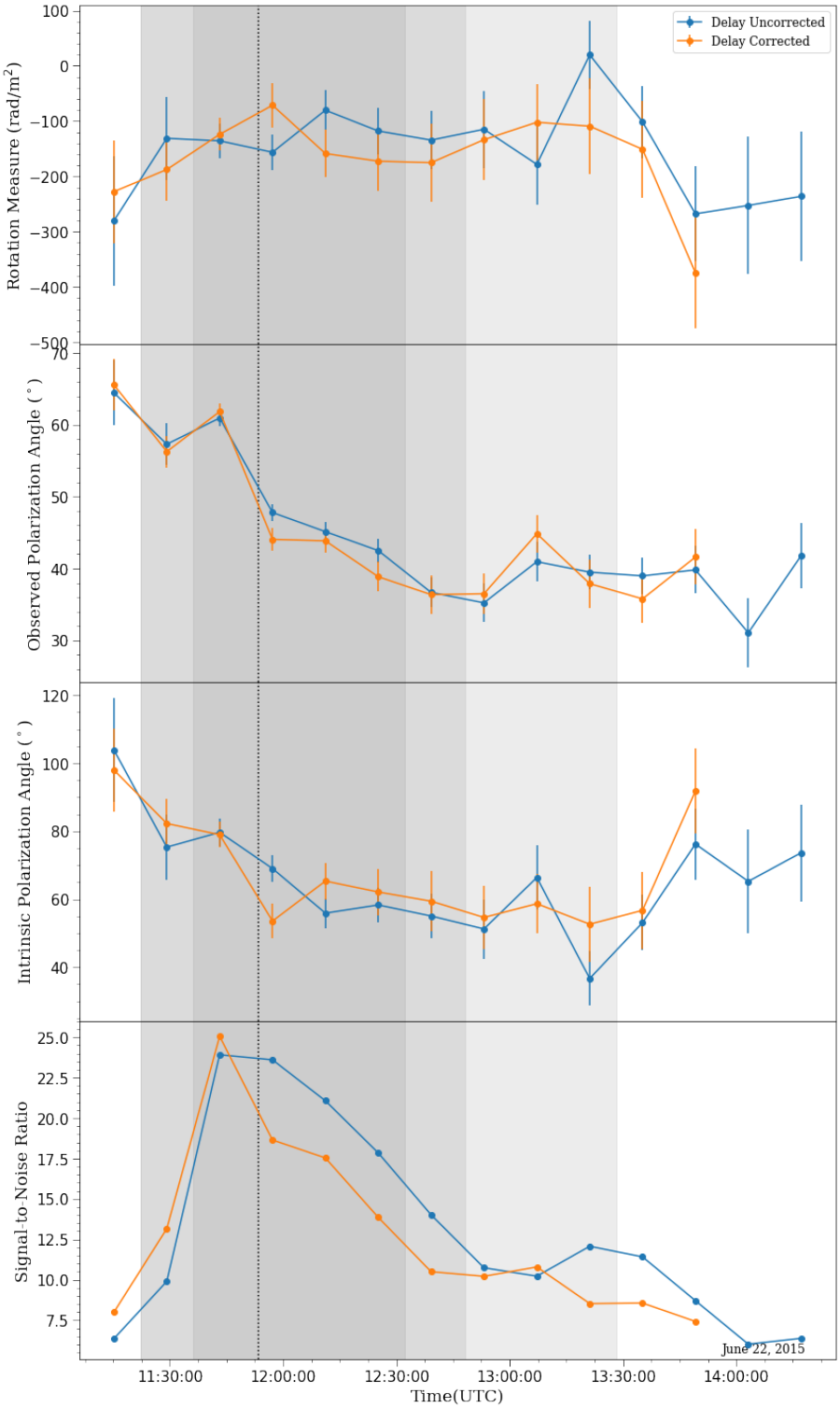


**Figure 3.8:** RM synthesis results for the 5/7 GHz data, with (orange) and without (blue) a delay correction. The shaded regions are the same as Figure 3.7. The vertical dotted line marks the division between flare I and II. The flare I/II delay correction was applied to the data points to the left/right of the vertical line.

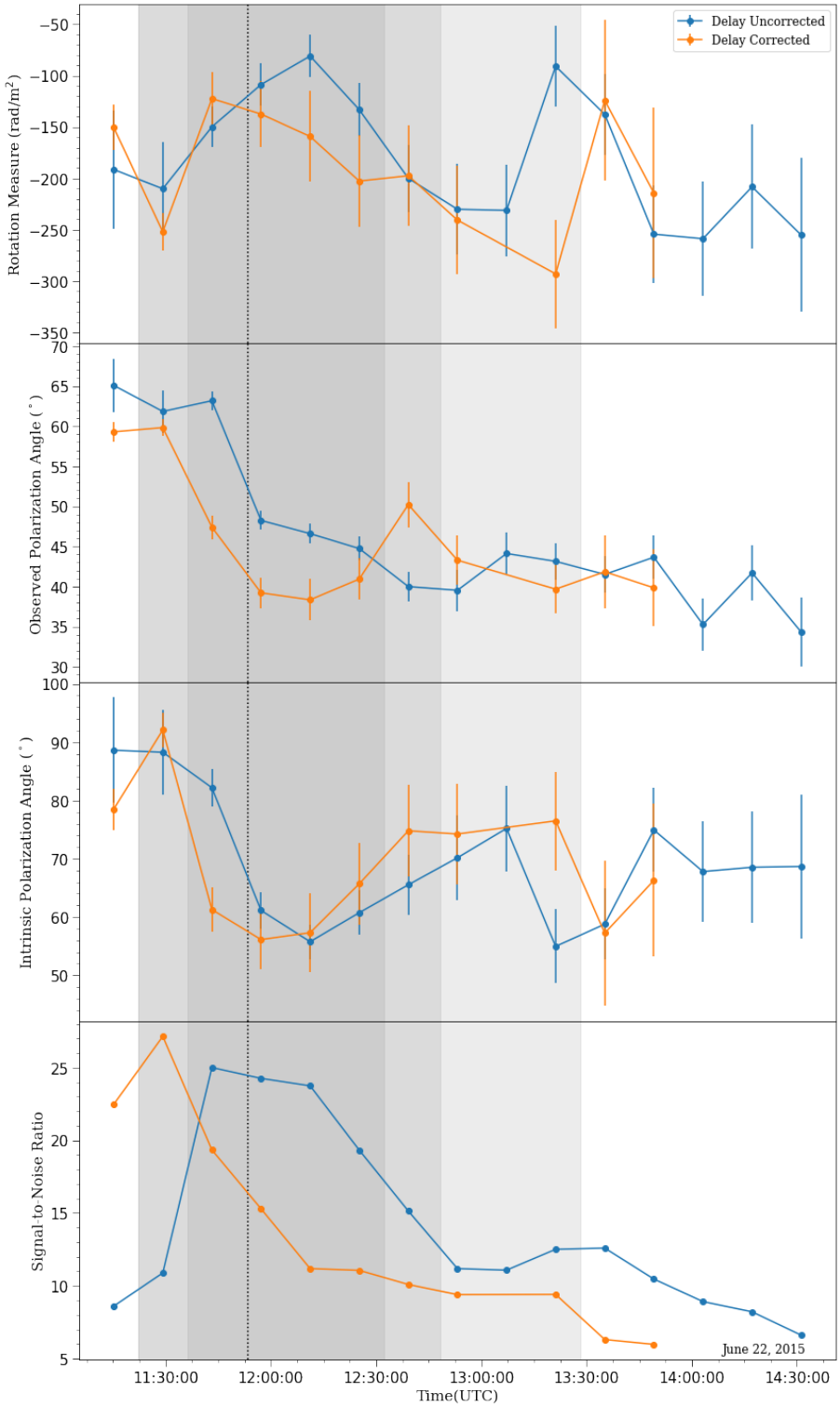


**Figure 3.9:** RM synthesis results for the full baseband data, with (orange) and without (blue) a delay correction. The shaded regions are the same as Figure 3.7. The vertical dotted line marks the division between flare I and II. The flare I/II delay correction was applied to the data points to the left/right of the vertical line.

# Chapter 4

# Discussion

In this Chapter, the results from Chapter 3 are discussed with respect to the previous analyses of V404 Cyg and to the general population of BHXRBs as a whole.

## 4.1 Peak Delays

The delays for the time of peak flux (Figure 3.3) display a (mostly) smooth increase in magnitude with a decreasing central frequency of the observing band, in addition to variability between the different flares. The maximum delays for the entire observing band ($\nu_{\rm ref} \equiv 26.347$ GHz) were $\sim$25, 45, and 60 minutes for flares I, II, and III, respectively. Restricting the frequencies to the 5/7 GHz basebands ($\nu_{\rm ref} \equiv 7.897$ GHz) reduced the maximum delay (as expected), while maintaining a similar frequency relationship. The reduced maxima for flares I, II and III are $\sim$5, 15, and 27 minutes, respectively. Figure 3.3b highlights the anomalous behaviour towards the lowest frequency spectral windows for flare III. The 5/7 GHz peak delay exhibits an abrupt $\sim$15 minute increase over a single spectral window, inconsistent with the preceding trend. In these spectral windows, the corresponding CCFs showed an extended plateau around the maximum coefficient, resulting in a poorly defined peak value. The flat nature

of the CCF increased as the time when the observations ended moved closer to the peak. Because of this, the lowest frequency (most delayed) light curves were the most affected and the observed discontinuity is likely nonphysical.

The full bandwidth data exhibited a similar"jump" in flare III's peak delays, although this discontinuity occurred within the frequency band gap between the 7 and 21 GHz basebands. The ZDCF algorithm preferentially fit the single peak of the 5/7 GHz light curves to the early-time peak of the bimodal structure observed in the light curves of the 21/26 GHz basebands. The ZDCF fitting resulted in a large inter-band delay inconsistent with the preceding (and following) intra-band trends. These intra-band trends exhibited an extremely similar behavior to peak delays measured from the flare II light curves. When comparing the 21 and 26 GHz data, the early-time peak exhibits a rapid decrease in magnitude when moving to the lower frequency baseband, while the late-time peak remains approximately constant (Figure 3.1). Additionally, the bimodal structure is completely absent from the intermediate frequency (15.6 GHz) VLBA light curve (Figure 4.1). This behaviour suggests that the early-time peak may also be absent from the 5 and 7 GHz light curves and the single peak structure is the remnant of the late-time peak. As a result, the ZDCF fits appear to be over-correcting the 26 to 5/7 GHz delays. The intra-band similarities for the full bandwidth delays and the similarity in the 5/7 GHz fits motivated the adoption of the flare II delays when applying the delay correction to either itself or flare III. In the lower panel of Figure 4.2, applying the flare II delay-correction to flare III aligns the 5/7 GHz peaks with the late-time peaks of the 21/26 GHz bimodal structure.

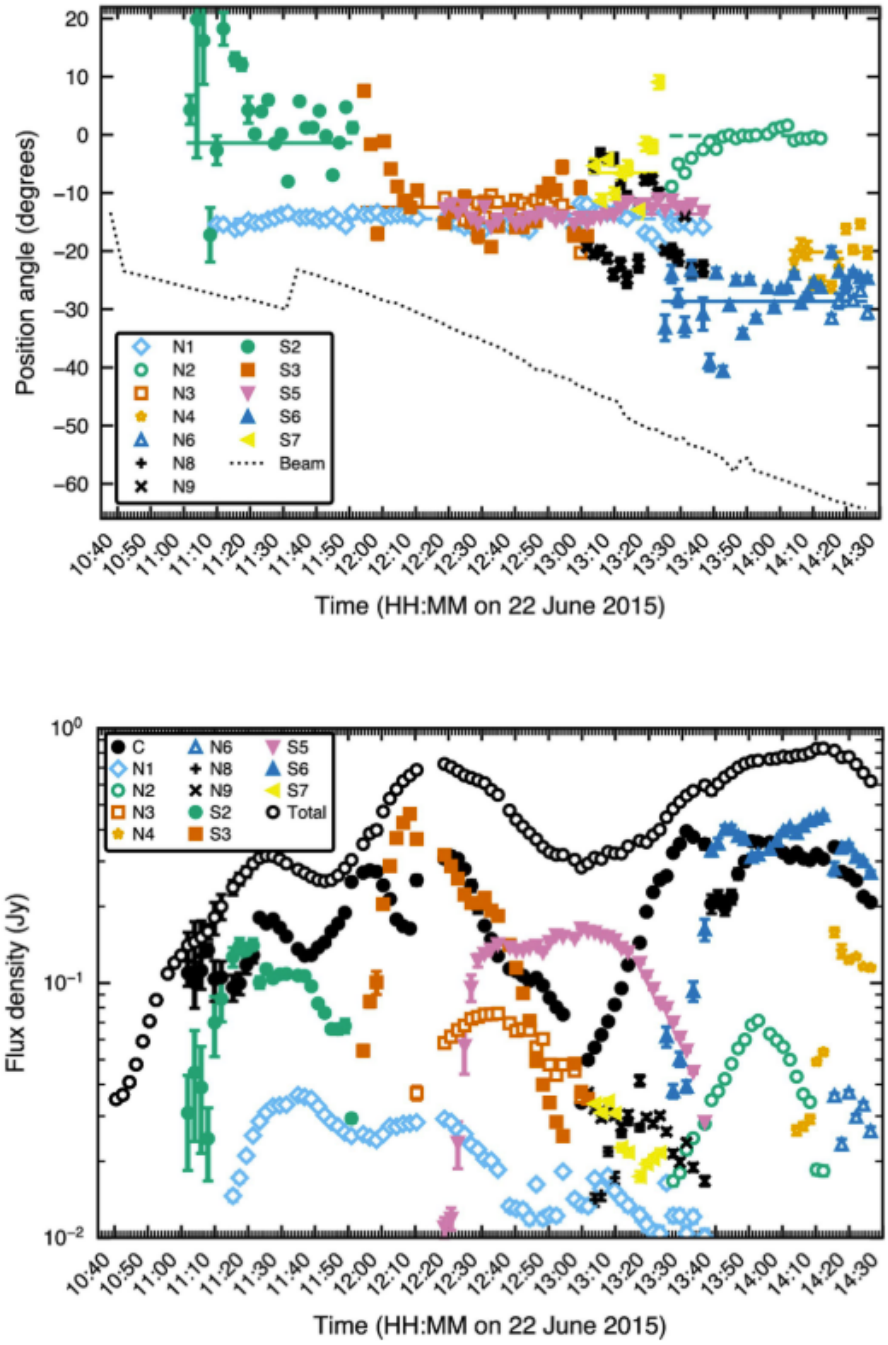


**Figure 4.1:** Key plots from the June 22nd VLBA observations; (Top) Position angles of the spatially resolved jet components. (Bottom) Light curves of resolved ejecta, compact core and total integrated flux as a function of time. These figures were taken directly from Miller-Jones et al. (2019).

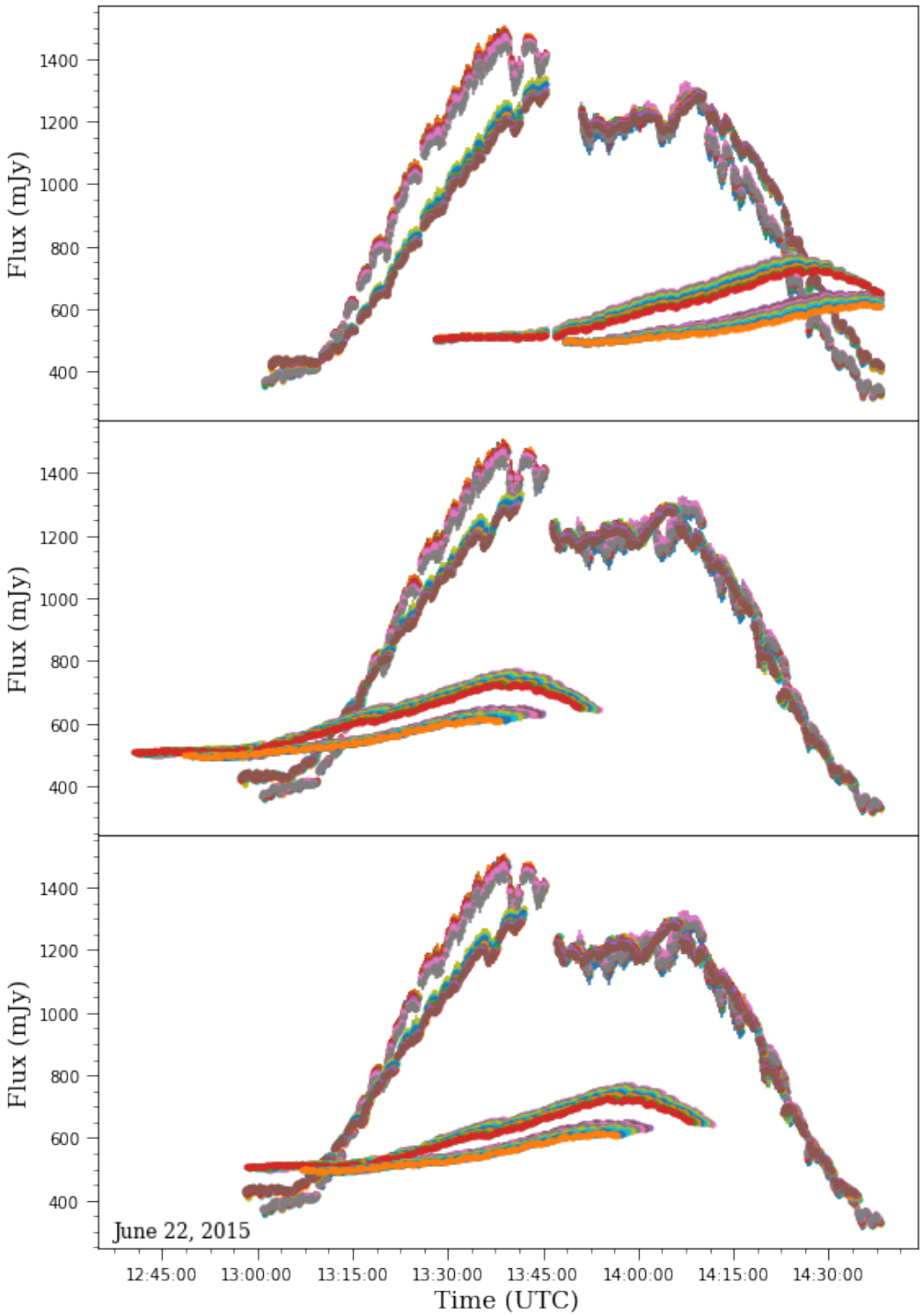


**Figure 4.2:** Flare III light curve with; (top) no delay correction, (middle) empirical delay correction measured by the ZDCF for flare III, (bottom) empirical delay correction measured by the ZDCF for flare II. Note, that the ZDCF algorithm fits the single peak in the 5/7 GHz light curve to the early time peak in 21/26 GHz. Applying the flare II delay correction to the flare III light curves positions aligns the 5/7 GHz light curves with the late time peak.

### 4.1.1 Model Comparisons

The multi-frequency intensity analysis of Tetarenko et al. (2017) quantitatively analysed the underlying properties of each baseband averaged light curve, modelling the jet morphology with two components; a compact jet with a constant-in-time flux and single spectral index, and a population of eight bi-polar vdL plasmoids with variable ejection times. The model included a predictive peak delay equation that was a modified version of the original equation presented in van der Laan (1966), relating the expected peak delays to the ejecta dynamics and the geometry of the system,

$$t_\nu = \frac{R_0}{\delta_\mp \beta_{\rm exp}} \left[ \left( \frac{\nu_{\rm IR}}{\nu} \right)^{\frac{p+4}{4p+6}} - 1 \right], \tag{4.1}$$

$$\delta_\mp = \frac{\sqrt{1-\beta_b^2}}{1 \mp \beta_b \cos i}, \tag{4.2}$$

where, $t_\nu$ is the delay of a given frequency $\nu$ with respect to the chosen reference of $\nu_{\rm IR} \equiv 230$ GHz. $\beta_b$ and $\beta_{\rm exp}$ are bulk (down-axis) and expansion speeds in units of $c$, and the inclination angle $i$ is the angle between the jet-axis and the observer's line of sight. $R_0$ is a characteristic radius of the ejecta at the reference frequency during its time of peak flux. The additional term $\delta_\mp$, transforms the delays from source to the observers frame, due to the mildly relativistic motion of the approaching $(-)$ and receding $(+)$ ejecta. The model predicted that each of the flares was dominated by, or entirely composed of, 2–4 of the ejecta[1]. The relationship between the empirical measurements of each flair and the predicted delays of the modelled composite ejecta are presented in Figure 4.3.

Of the three flares, flare II showed (unsurprisingly) the best agreement with the model predictions. Flare II had a clearly defined rise, decay, and peak across all 4 observing basebands. As a result, the ZDCF algorithm was the least affected by its methodological limitations when synthesizing the CCFs.

[1]A summary of the ejecta properties can be seen in in Table 2 and Figure 5 of the original paper Tetarenko et al. (2017).

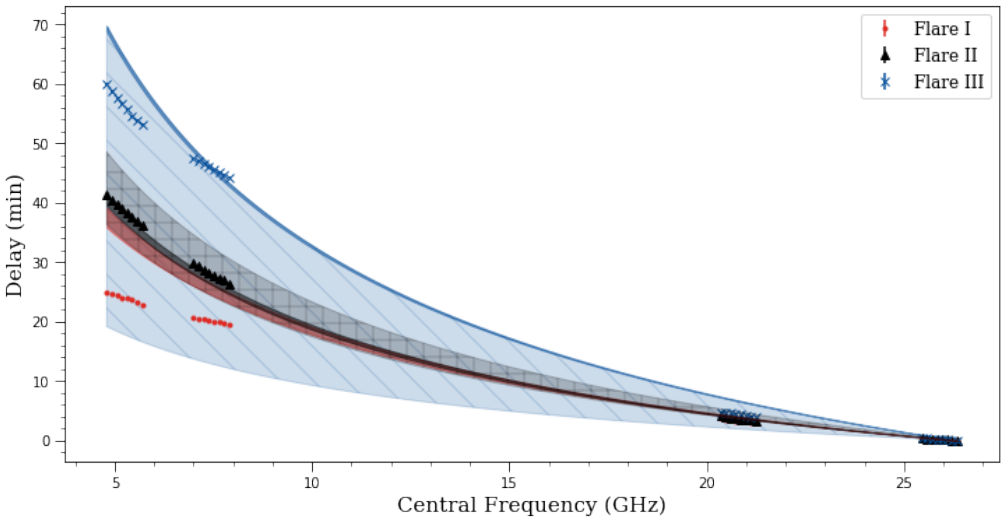


**Figure 4.3:** Peak delays for each of the three flares as a function of frequency. The data points correspond to the delays measured by the ZDCF algorithm for each of the spectral windows. The shaded regions of similar colour visualize the predicted range of delays for each flare's model components. The dark regions correspond to delay range spanned by the approaching/receding components of the dominant ejections; ejection 3 and ejection 7 for flare II and III respectively. The light hatched region corresponds to the full range of delays spanned by each flares composite ejecta. The predicted delay range of flare I is significantly narrow and, as a result, it was limited to a single shaded region. It should be noted that (although difficult to see) the lower limits of the shaded region for flare I and II are overlapping.

Additionally, the model predicted that the flare was dominated by 2 bi-polar ejections with similar delays and a small ($\pm\,7.5$ minute) range centered around the "median" values. Flare III's dominant ejection (roughly) agrees with the ZDCF's fitting, suggesting that the single peak observed in 5/7 GHz is in fact the early-time peak in the 21/26 GHz basebands, and the applied delay correction may be inaccurate. However, the complex morphology of flare III is a result of 4 composite ejection events, with a broad range of delays ($\sim$20–70 minutes) that encompass both empirical delay curves of II and III. Since the observations end before a (potential) secondary peak was observed, it is not possible to conclusively determine which (if either) of these scenarios is accurate. Lastly, the predicted delays of the first flare are significantly and consistently larger than the empirical measurements. The model predicted a second peak in the 21/26 GHz light curves at earlier times than the start time of the observations

(akin to the issues with flare III). The single 5/7 GHz peak structure results from the smoothed, overlapping light curves from the two composite ejections becoming indistinguishable from a single flare. As a result, the empirically determined flare I delays may also be an underestimation.

The preceding comparisons between the measured and predicted delays highlight the uncertainties inherent to this simplified approach. The implicit assumption that all of the ejecta contained within each flare have similar geometric and kinematic properties appears unreasonable when compared to the quantitative modelling of Tetarenko et al. (2017). As a result, the ascription of a single delay to each flare (at each spectral window) may have little meaning. Furthermore, the relative positions and fractional flux contributions of the ejecta composing each flare will vary with the central frequency. For example, the Tetarenko et al. (2017) model predicts that the peaks of the two ejecta responsible for the bimodal structure of flare III at 21/26 GHz become aligned within the 5/7 GHz light curves, resulting in the observed single peak structure. Acknowledging these potential inaccuracies, the empirically motivated delay corrections will be treated as a zeroth-order investigation into their effects on the derived polarimetric properties.

### 4.1.2 Delay Corrected Polarimetry

Comparisons between the peak delay corrected and uncorrected polarization properties are presented in Figure 3.8 and 3.9 respectively. The large separation between the peaks of the highest and lowest spectral windows ($\sim$25–60 minutes, a factor of $\sim$2–4 times the size of the imaging window) offered an interesting opportunity to study the effects of frequency-dependent absorption on the observed polarization properties. It was known *a priori* that the observed fluxes were a superposition of multiple jet components (with differing morphologies), and thus would not follow the peak delay interpretation of a single vdL bubble. However, any observed changes, or lack thereof, after the application of the delay

correction may provide insight into the dominant component of the underlying jet.

Unfortunately, as discussed in Section 3.3, the majority of the 21/26 GHz polarization detections had low significance with respect to the expected degree of spurious linear polarization. As a result, the determination of the rotation measure and polarization angle was limited to the lower frequency 5/7 GHz basebands. Although the majority of the $\lambda^2$ bandwidth was retained — resulting in a negligible loss of rotation measure resolution — the maximum offset between the peaks was reduced to $\sim$ 15 minutes and the significance with respect to the size of the imaging window was greatly reduced. The bottom panels of Figures 3.8 and 3.9 show that the application of the delay corrections resulted in a reduction of the dominant Faraday component's S/N in most cases and a insignificant increase in others. Interestingly, the increases only occurred when applying the empirical flare I delay corrections which (as discussed in Section 4.1.1) is likely an underestimate. Additionally, flare II showed a consistent and significant decrease in S/N despite being the only flare that had strong agreement between the empirical and model predicted delays. Thus, the delay corrections resulted in a net misalignment of the de-rotated polarization angles and subsequent decoherence. This may suggest that the effects of the evolving optical depth are insignificant as would be the case for a compact jet dominated light curve (making the delay correction superfluous or even corrupting) or that the delays originate from a different mechanism that doesn't affect the orientation of the intrinsic polarization angle (i.e., dispersion by a dense magneto-ionic plasma; van der Laan 1966). Future observations of single large-scale ejection events during a successful transition from the hard-to-soft state — as is common among flaring BHXRB (Fender and Gallo, 2014) — will remove the multi-component complexity and allow for a more detailed analysis towards the origins of the peak delays and the validity of their potential corrections.

## 4.2 Polarization Properties

The following subsections will present some preliminary qualitative interpretations of the polarimetric results presented in Chapter 3. It should be noted that the $\sim 14$ minute timescales correspond to one of, if not the, highest temporal resolution radio polarimetric study of a BHXRB outburst to date.

As a result of the reduction in S/N caused by the application of the peak correction, the discussion of the polarization angle and rotation measure is limited to the delay uncorrected data. Additionally, due to the poorly understood nature of the spurious fractional polarization and the non-linear relationship between the polarization properties and the $Q/U$ fluxes, the discussion of the rotation measure and polarization angle is further limited to four GHz time-bins with $\gtrsim 99\%$ significance in both the 5 and 7 GHz basebands, between 11:36–12:32.

### 4.2.1 Rotation Measure

The derived rotation measure exhibited a degree of variability with $-180 \lesssim \mathrm{RM} \lesssim -70$ rad m$^{-2}$, depending on the time bin (Top panel, Figure 3.7). To assess the significance of the detections, it is useful to compare the measured values to the models of Galactic RM along a similar line of sight. The three most widely adopted models predict a Galactic RM in the direction of V404 Cyg of; $-30 \pm 10$ rad m$^{-2}$ (Oppermann et al., 2012), $-36 \pm 20$ rad m$^{-2}$ (Oppermann et al., 2015), and $-130 \pm 50$ rad m$^{-2}$ (Hutschenreuter and Enßlin, 2020). The former two models are significantly different from the measured RMs of V404 Cyg, although the most recent modelling is consistent within error to the measured RMs. However, the model predicts the total Galactic RM along a given line of sight, whereas V404 Cyg is located $\sim 2.39$ kpc from Earth (well within the Galactic boundaries). One could naively assume a constant Galactic magnetic field and construct distance arguments that would suggest the observed

RM is significantly higher than expected for the Galactic contribution. However, large-scale inversion of the Galactic magnetic field direction is not only possible, but predicted. For example, Van Eck et al. (2011) derived a zeroth-order model of the magnetic field within the Galactic disk[2]. The model predicts a Galactic magnetic field aligned parallel to the line of sight throughout the entirety of the ISM separating Earth and V404 Cyg. Thus, the predicted Galactic RM will be positive at the distance and position of V404 Cyg, suggesting that the derived (significantly negative) RM is dominated by a component local to the source environment. Therefore, the outburst has likely resulted in the formation of a dense population of electrons or a strong magnetic field that has subsequently boosted the effects of Faraday rotation. Of the two scenarios, the former seems more likely, as a strong magnetic field is often associated with a high degree of linear polarization and the observed polarization fraction is weak.

Significant variability would further support the existence of a strong local contributions to the observed RM, as the Galactic component is not expected to vary significantly on timescales of $\sim 15$ minutes. However, the significance of the variability is method dependent. Assuming a constant model equal to the weighted mean of the rotation measures, $-126$ and $-114$ rad m$^{-2}$ results in $\chi^2$ values of 2.71 and 9.83 (3 degrees of freedom) for the RM Synthesis and MCMC fits, respectively. Thus, despite the two methods being consistent within each time bin, the lower uncertainties and elevated scatter of the Bayesian modelling supports the hypothesis that the RM is variable. In both the 2015 and 1989 outbursts, V404 Cyg exhibited a spectral variability that was ascribed to heavy and strongly variable local absorption (Oosterbroek et al., 1996; Życki et al., 1999; Motta et al., 2017). Subsequent modelling of the X-ray spectra during the most recent outburst by Motta et al. (2017) revealed that the absorption

[2]This paper defined the Galactic disk as heights from the Galactic plane ($z$) such that $|z| < 1.5$ kpc assuming zero Galactic magnetic field outside the range and azimuthal symmetry. The line of sight containing V404 Cyg meets the disk criterion for all Galactocentric radii considered to fall within the boundaries of the Milky Way.

was caused by the partial obscuration of the X-ray emission region by a patchy substructure with a high column density. Presuming a similar substructure extends out to the radio emitting regions, it could be the origin of the (potential) rotation measure variability, due to either the motion of the absorbing regions themselves or the changing line of sight (local to V404 Cyg) as the discrete eject propagate. Constant rotation measures have been observed in flaring BHXRBs (e.g., XTE J1748-288; Brocksopp et al. 2007), although previous multi-flare outbursts have shown a similar amount of RM variability (e.g., GRO J1655−40; Hannikainen et al. 2000). Therefore neither our current quantitative analysis nor population precedent conclusively suggests the variable rotation measure is significant.

The uncertainties of the RM synthesis fits are a function of the noise level extracted from the CLEAN FDF. Therefore, the method chosen to quantify the FDF noise determines the magnitude of the uncertainties. In the current iteration, the RMS was chosen as it maximized the noise and, by extension, it was the most conservative measure of the detection significance. In contrast, the `RM-tools-1D` package generally utilizes the median-absolute-deviation (MAD). If the MAD is applied to these observations, the noise level and RM uncertainty decreases on average by a factor of $\sim 2$, boosting the $\chi^2$ value to be in line with the Bayesian modelling. But using the MAD also increases the number of significant Faraday detections to an unreasonable number ($\gtrsim 10$). As it stands, it is unclear whether the statistical approach of the Bayesian modelling or the sampled noise of the FDF more accurately describe the level of confidence in the derived rotation measures. The appropriate treatment of the FDF noise is an ongoing investigation and will be updated in future work.

Some of the Faraday dispersion functions had populations of secondary $> 5\sigma$ detections with significantly larger rotation measures, $\pm(0.02 - 1) \times 10^5$ rad m$^{-2}$, than their primaries. RM magnitudes that extreme are characteristic of extremely particle-rich lines of sight, such as towards the Galactic centre, and

have never been observed in BHXRBs. Assuming the secondary components are real, this would suggest that there exists a population of extremely dense or highly magnetic *clouds*. The clouds would have to have angular scales smaller than V404 Cyg and exist within the Milky Way or in the local environment of V404 Cyg. It seems incredibly unlikely that such a population of objects would exist within the Galaxy and not have been discovered during any of the recent RM surveys (Oppermann et al., 2012, 2015; Hutschenreuter and Enßlin, 2020). To test if this phenomenon is unique to V404 Cyg, the time resolved RM synthesis routines were applied to the nearby phase calibrator, a bright and stable extragalactic source with a steady $\sim 2\%$ linear polarization. A similar population of secondary detections was observed, despite the local environment neither being expected nor observed to display any local variability. As a result, these detections appear more likely to be the remnants of sampling effects in the FDF that were missed during CLEAN (cf., the effects of poor/patchy $uv$-coverage during synthesis imaging; Taylor et al. 1999). The frequency of these $5\sigma$ false positives does not follow statistical expectation, pointing towards a systematic error or intrinsic limitation within current RM synthesis routines.

### 4.2.2 Polarization Angle

The observed polarisation angle ($\psi_w$) displayed a clear variability on timescales $\lesssim$15 minutes, regardless of the applied polarimetric method. Additionally, the changes in the observed polarization angle cannot be fully ascribed to the potentially variable rotation measure, suggesting there is a component that is a result of an intrinsic evolution of the emission region. The intrinsic polarization angle ($\psi_0$) was observed to decrease from $\sim 80^\circ$ to $\sim 50$–$60^\circ$ between 11:36–12:32, although the rate of decrease was dependent on the polarimetric method and the assumed behaviour of the rotation measure (Bottom panel, Figure 3.7). During the corresponding time interval in the VLBA light curves, the total intensity was initially dominated by the S2 component with a position angle

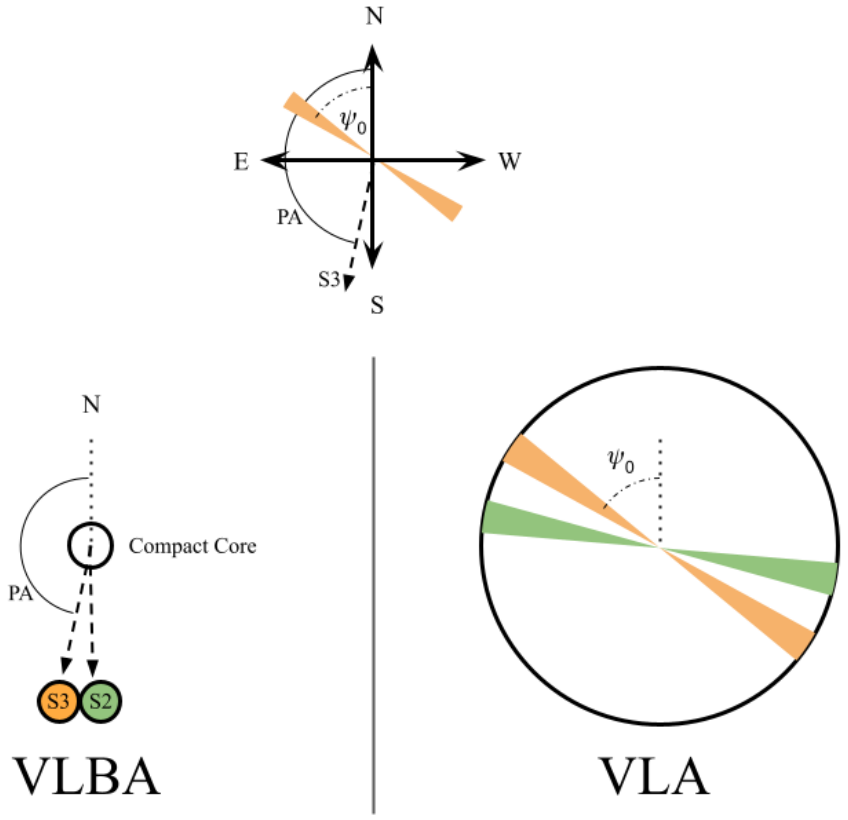


**Figure 4.4:** A schematic diagram of the different angles of interest as observed by their corresponding interferometric arrays for component S2 and S3. *left*: The components as seen by the VLBA. The dashed line arrows correspond to the direction of propagation of the ejecta projected onto the sky. The position angle (PA) for the ejecta is measured East of North. *right*: The events as seen by the VLA. The VLA observations do not have sufficient angular resolution to separate the compact core and the discrete ejecta and, as a result, a single source is imaged. The colour-coordinated shaded regions corresponds to the range of intrinsic polarization angles, $\psi_0$, during the corresponding times of dominance for each component. The PA and $\psi_0$ values for component S3 were mapped onto the compass.

(PA) of $\sim 1^\circ$ East of North and the compact core with an unresolved PA (see Figure 4.4 for a schematic diagram of the geometry). Late times showed the disappearance of S2 and the rise of S3, PA $\sim -12^\circ$ (Top panel, Figure 4.1). Past analyses have suggested that the compact core may be significantly depolarized when compared to the discrete ejections (e.g., Brocksopp et al. 2007). If a similar scenario is assumed for V404 Cyg, the polarization angle orientation in the time-interval of interest will be dominated by the properties of the S2/S3 components. Initially, the value of $\psi_0 \sim 80^\circ$ is (nearly) perpendicular to the

PA of the S2 component during the optically-thin peak/decay of its intensity light curves (Bottom panel, Figure 4.2) . Assuming a vdL description of each ejection, the observed orthogonality is characteristic of a magnetic field oriented parallel to the jet-axis. If the magnetic field conditions are assumed to be similar between the two components, there is an expected $\sim 80^{\circ}$ swing in the polarization angle caused by an inversion in the absorption conditions between the optically-thin decay of S2 and the optically-thick rise of S3. However, no such swing is observed and the final polarization angle is oriented neither orthogonal nor parallel to the jet-axis (it has an intermediate angle of $\sim 60$–$70^{\circ}$ with respect to the PA of S3). Thus, if the core is depolarized, the mechanisms that orient the magnetic field with respect to the jet-axis vary on time-scales shorter than the separation of successive ejection events and are poorly described by simplistic shearing and/or shock-compression models.

Interestingly, the change in the intrinsic polarization angle is of a similar magnitude to the swing of the PA ($\sim 30^{\circ}$) between the N2/S2 and N6/S6 components that were used to constrain the period of the precessing jet, and the $\lesssim 1$ hour timescale is less than $\sim 1.3$ hour separation of the ejection times. Therefore, the variability is consistent with the upper limit of the jet precession period and the changes in the intrinsic polarization angle may be instead tracking the precession effects of the jet axis for a polarized compact core. Unfortunately, without spatially-resolved polarimetry, determining if either or both of the two scenarios is more likely is not possible. Future inclusion of the time-dependent spectral index may help to disentangle the effects from overlapping optically thick and thin emission.

### 4.2.3 Fractional Polarization

Each baseband showed a weak but variable level of fractional polarization, $\sim 0.1$–$0.8\%$ and $\sim 0.05$–$0.25\%$ in the 21/26 GHz and 5/7 GHz bands, respectively (Figure 3.6). Unfortunately, the relative contributions from spurious effects are

poorly constrained. Across all basebands, the maximum fractional polarization corresponded to the intermediate region between the peak of flare I and the local minimum during the I-to-II transition. Interestingly, the singular fractional polarization peak, like the intensities, followed a delay with the lower frequencies lagging behind the higher. There is marginal evidence of a secondary increase in fractional polarization in the 21/26 GHz band, occurring alongside the decay of flare III. The secondary increase is not observed in the 5/7 GHz data, although this may be due to the delays shifting the peak outside of the observed time range.

Fractional polarizations that are lower than the upper limits predicted by the theoretical framework of synchrotron emission are a typical result of radio polarimetric observations of flaring BHXRBs. That being said, the majority of outbursts have shown significantly higher maximum fractional polarizations $\gtrsim 2\%$ at low frequency (1–10 GHz) observations (Curran et al., 2015; Brocksopp et al., 2007; Fender, 2003), with rare cases reaching appreciable fractions of the theoretical limits (e.g., the $\sim 50\%$ detections of Curran et al. 2014 or Brocksopp et al. 2013). A similar multi-flaring highly-luminous state was entered by the BHXRB GRO J1655-40 during its 1994 outburst (although the timescales of each flare's decay were significantly longer) and reached 4–8 GHz fractional polarizations of $\sim 1-10\%$ with variability as high as 4% on timescales less than half a day, suggesting that weakly polarized emission is not intrinsic to these multi-flaring events (Hjellming and Rupen, 1995; Hannikainen et al., 2000). A glimpse of a comparably low fractional polarization was observed during the 80 day monitoring campaign of V404 Cyg's 1989 outburst. The first day of observations caught the tail of a decaying "major synchrotron bubble event" that had the lowest fractional polarizations ($\sim 0.44/0.35\%$ for the 5/8 GHz bands) of all the observations. Following the decay, both the spectral and polarimetric properties stabilized to values characteristic of a typical compact jet(Han and Hjellming, 1992). It is possible that what was observed in 1989

was the end of a similar short-timescale multi-flaring event and the anomalously weak fractional polarization is an intrinsic characteristic of an outbursting V404 Cyg.

In the 15.6 GHz observations (Bottom panel, Figure 4.1), assuming they follow a similar delay as the VLA observations, the maximum fractional polarization occurs between ∼11:30–11:50, at a time when the compact core is dominant. If the compact core dominance is correlated with a high fractional polarization, then one would expect a secondary peak in the fractional polarization between ∼ 13:10–13:20 during a second interval of (more significant) core domination; however, this is not observed. Conversely, as discussed in Section 4.2.2, if the compact core is depolarized, then the maximum fractional polarization occurs during the dominance of the S2 component. Assuming this to be true, the rapid increase in polarization during the decay of S2 is consistent with the transition to optically-thin synchrotron emission that the vdL model predicts for a single ejecta.

A common explanation of a reduced fractional polarization is the superposition of multiple components (Brocksopp et al., 2013), with (partially) orthogonal magnetic field orientations *cancelling* each other out. However, secondary peaks in fractional polarization were not observed during subsequent periods of intensity dominance during the decay of a single component; e.g., component S3 domination between ∼ 12:05–12:20 and component S5 domination between ∼ 12:40–13:20. Therefore, there is either a physical mechanism exclusive to S2 that intrinsically boosted its fractional polarization or the compact core becomes a "counter-balancing" polarization components at later times. The latter scenario is consistent with the misassociation of a population unresolved ejecta as a compact jet. Fender et al. (2004) proposed a "shock-in-jet" picture where the peaks in total intensity are produced by collisions between jet components with different velocities. The collisions are expected to temporarily disorder the magnetic field, while generating shocks that would provide a mechanism to

reform an ordered direction at later times; thus, the peak in the fractional polarization would lag the peaks in the intensity (Brocksopp et al., 2007). A similar idea can be applied to these discrete ejecta. The single fractional polarization peak that follows flare I (the lowest luminosity flare) may be a result of a small number, or single, collision. The following flares have larger intensities due to a more frequent and/or continuous number of ejecta collisions that inhibit the reformation of a structured magnetic field and, as a result, maintain the low degree of fractional polarization. However, this picture is difficult to reconcile with the precession of the jet axis as well as the smooth decrease in fractional polarization. Alternatively, the low fractional polarization could be attributed to a strong Faraday depolarization and the variability to the variable rotation measure. Spatially variable depolarization is a common feature in the larger analogs of BHXRBS, active galactic nuclei, although it has also been observed in the X-ray binary SS 443 (Stirling et al., 2004; Miller-Jones et al., 2008). In the absence of spatially resolved polarimetry, disentangling these effects is difficult and the complete picture is likely a combination of multiple mechanisms both intrinsic to singular jet components and a result of their interactions.

# Chapter 5

# Conclusions and Future Work

This thesis has presented the data reduction, imaging, and time-resolved radio polarimetry of V404 Cyg's 2015 outburst, as well as a preliminary analysis of the derived polarization properties. The ∼14 minute imaging windows constitute one of, if not the, shortest timescale polarimetric analyses of the radio emission from BHXB jets to date. The polarization properties exhibited clear variability in the fractional polarization and polarization angle (both intrinsic and observed) and a potentially variable rotation measure, consistent with a rapidly evolving geometry and/or magnetic environment. A number of systematic limitations — and the intrinsic complexity of the system — made it difficult to confidently ascribe a relationship between the evolution of the polarization properties and the local environment. Therefore, the interpretation of these results was kept purposefully speculative.

Extensive efforts were taken to ensure the precision and accuracy of the calibration and reduction of data. Ongoing work will attempt to reconcile the observed variability and weak degree of linear polarization with quantitative theoretical models and predictions. Furthermore, the contributions of the spurious fractional polarization with respect to the individual Stokes parameters will be investigated, in an attempt to more accurately constrain its effects on the rotation measure and polarization angles. It should be noted that the original

investigation into the effects of spurious fractional polarization recognized that their statistical framework likely overestimated the effects of the spurious fractional polarization (Hales, 2017) and, as a result, the current restrictions to the 99% significance interval may be too aggressive. Additionally, there was a secondary observing run taken $\sim$ 2 weeks after the original observations, during V404 Cyg's return to quiescence. It will be interesting to see if these observations follow a similar behaviour as the 1989 outburst, i.e a significant increase in the polarization fraction and a spectral behaviour consistent with a single compact jet (Han and Hjellming, 1992).

In a more general context, the methodologies developed in this analysis are not exclusive to V404 Cyg and can be easily applied to future polarized transient events (both for other BHXBs and a wider range of rapidly varying astrophysical objects). The issues that arose during this work will also greatly help during the planning of future observing runs. Specifically, the leakage calibrator will be observed over a longer time period and (if possible) at multiple parallactic angles. In doing so, the increased S/N will reduce the magnitude of any spurious polarization. Additionally, future spatially-resolved observations will include full polarization calibration, allowing for more stringent constraints on the underlying polarization mechanisms. Lastly, with the ongoing construction/expansion of the new generation of interferometric arrays with greatly improved sensitivities (i.e., the ngVLA and the SKA) future time-resolved polarimetric analysis will be able to further reduce the temporal imaging windows, minimizing any potential averaging biases and more accurately capturing the instantaneous polarization properties of future BHXB outbursts and their evolving local environments.

# Bibliography

Tal Alexander. *Is AGN Variability Correlated with Other AGN Properties? ZDCF Analysis of Small Samples of Sparse Light Curves*, volume 218 of *Astrophysics and Space Science Library*, page 163. 1997. doi: 10.1007/978-94-015-8941-3_14.

Tal Alexander. Improved AGN light curve analysis with the z-transformed discrete correlation function. *arXiv e-prints*, art. arXiv:1302.1508, February 2013.

S. D. Barthelmy, A. D'Ai, P. D'Avanzo, H. A. Krimm, A. Y. Lien, F. E. Marshall, A. Maselli, and M. H. Siegel. Swift trigger 643949 is V404 Cyg. *GRB Coordinates Network*, 17929:1, June 2015.

T. M. Belloni. *States and Transitions in Black Hole Binaries*, volume 794, page 53. 2010. doi: 10.1007/978-3-540-76937-83.

R. D. Blandford and A. Königl. Relativistic jets as compact radio sources. *ApJ*, 232:34–48, August 1979. doi: 10.1086/157262.

R. D. Blandford and D. G. Payne. Hydromagnetic flows from accretion disks and the production of radio jets. *MNRAS*, 199:883–903, June 1982. doi: 10.1093/mnras/199.4.883.

R. D. Blandford and R. L. Znajek. Electromagnetic extraction of energy from Kerr black holes. *MNRAS*, 179:433–456, May 1977. doi: 10.1093/mnras/179.3.433.

M. A. Brentjens and A. G. de Bruyn. Faraday rotation measure synthesis. *A&A*, 441(3):1217–1228, October 2005. doi: 10.1051/0004-6361:20052990.

D Briggs. High Fidelity Deconvolution of Moderately Resolved Sources. *Ph. D. thesis, New Mexico Institute of Mining and Technology. Avaible via* `http://www.aoc.nrao.edu/dissertations/dbriggs/`, 1995.

C. Brocksopp, J. C. A. Miller-Jones, R. P. Fender, and B. W. Stappers. A highly polarized radio jet during the 1998 outburst of the black hole transient XTE J1748-288. *MNRAS*, 378(3):1111–1117, July 2007. doi: 10.1111/j.1365-2966.2007.11846.x.

C. Brocksopp, S. Corbel, A. Tzioumis, J. W. Broderick, J. Rodriguez, J. Yang, R. P. Fender, and Z. Paragi. XTE J1752-223 in outburst: a persistent radio jet, dramatic flaring, multiple ejections and linear polarization. *MNRAS*, 432 (2):931–943, June 2013. doi: 10.1093/mnras/stt493.

B. J. Burn. On the depolarization of discrete radio sources by Faraday dispersion. *MNRAS*, 133:67, January 1966. doi: 10.1093/mnras/133.1.67.

J. Casares and P. A. Charles. Optical studies of V404 Cyg, the X-ray transient GS 2023+338. IV. The rotation speed of the companion star. *MNRAS*, 271: L5–L9, November 1994. doi: 10.1093/mnras/271.1.L5.

Ioannis Contopoulos, Nikolaos D. Kylafis, Demosthenes Kazanas, and Dimitris M. Christodoulou. Formation and Destruction of Jets in X-Ray Binaries. In *International Journal of Modern Physics Conference Series*, volume 8 of *International Journal of Modern Physics Conference Series*, pages 287–292, January 2012. doi: 10.1142/S2010194512004722.

P. A. Curran, M. Coriat, J. C. A. Miller-Jones, R. P. Armstrong, P. G. Edwards, G. R. Sivakoff, P. Woudt, D. Altamirano, T. M. Belloni, S. Corbel, R. P. Fender, E. G. Körding, H. A. Krimm, S. Markoff, S. Migliari, D. M. Russell,

J. Stevens, and T. Tzioumis. The evolving polarized jet of black hole candidate Swift J1745-26. *MNRAS*, 437(4):3265–3273, February 2014. doi: 10.1093/mnras/stt2125.

P. A. Curran, J. C. A. Miller-Jones, A. P. Rushton, D. D. Pawar, G. E. Anderson, D. Altamirano, H. A. Krimm, J. W. Broderick, T. M. Belloni, R. P. Fender, E. G. Körding, D. Maitra, S. Markoff, S. Migliari, C. Rumsey, M. P. Rupen, D. M. Russell, T. D. Russell, C. L. Sarazin, G. R. Sivakoff, R. Soria, A. J. Tetarenko, D. Titterington, and V. Tudose. Radio polarimetry as a probe of unresolved jets: the 2013 outburst of XTE J1908+094. *MNRAS*, 451(4):3975–3985, August 2015. doi: 10.1093/mnras/stv1252.

Chris Done, Marek Gierliński, and Aya Kubota. Modelling the behaviour of accretion flows in X-ray binaries. Everything you always wanted to know about accretion but were afraid to ask. *Astronomy and Astrophysics Review*, 15:1–66, Dec 2007. doi: 10.1007/s00159-007-0006-1.

R. J. H. Dunn, R. P. Fender, E. G. Körding, T. Belloni, and C. Cabanac. A global spectral study of black hole X-ray binaries. *MNRAS*, 403(1):61–82, March 2010. doi: 10.1111/j.1365-2966.2010.16114.x.

R. P. Fender, T. M. Belloni, and E. Gallo. Towards a unified model for black hole X-ray binary jets. *MNRAS*, 355(4):1105–1118, December 2004. doi: 10.1111/j.1365-2966.2004.08384.x.

R. P. Fender, J. Homan, and T. M. Belloni. Jets from black hole X-ray binaries: testing, refining and extending empirical models for the coupling to X-rays. *MNRAS*, 396(3):1370–1382, July 2009. doi: 10.1111/j.1365-2966.2009.14841.x.

Rob Fender. Circularly polarised radio emission from GRS 1915+105 and other X-ray binaries. *Ap&SS*, 288(1):79–95, March 2003. doi: 10.1023/B:ASTR.0000004996.95929.b7.

Rob Fender. *Jets from X-ray binaries*, volume 39, pages 381–419. 2006.

Rob Fender and Elena Gallo. An Overview of Jets and Outflows in Stellar Mass Black Holes. *SSRv*, 183(1-4):323–337, September 2014. doi: 10.1007/s11214-014-0069-z.

Daniel Foreman-Mackey, David W. Hogg, Dustin Lang, and Jonathan Goodman. emcee: The MCMC Hammer. *PASP*, 125(925):306, March 2013. doi: 10.1086/670067.

C. L. Fryer, S. E. Woosley, and A. Heger. Pair-Instability Supernovae, Gravity Waves, and Gamma-Ray Transients. *ApJ*, 550(1):372–382, March 2001. doi: 10.1086/319719.

E. Gallo, R. P. Fender, and G. G. Pooley. A universal radio-X-ray correlation in low/hard state black hole binaries. *MNRAS*, 344(1):60–72, September 2003. doi: 10.1046/j.1365-8711.2003.06791.x.

Samuel J. George, Jeroen M. Stil, and Ben W. Keller. Detection Thresholds and Bias Correction in Polarized Intensity. *PASA*, 29(3):214–220, October 2012. doi: 10.1071/AS11027.

V. L. Ginzburg and S. I. Syrovatskii. Developments in the Theory of Synchrotron Radiation and its Reabsorption. *ARA&A*, 7:375, January 1969. doi: 10.1146/annurev.aa.07.090169.002111.

Jonathan Goodman and Jonathan Weare. Ensemble samplers with affine invariance. *Communications in Applied Mathematics and Computational Science*, 5(1):65–80, January 2010. doi: 10.2140/camcos.2010.5.65.

C. A. Hales, B. M. Gaensler, R. P. Norris, and E. Middelberg. Analytic detection thresholds for measurements of linearly polarized intensity using rotation measure synthesis. *MNRAS*, 424(3):2160–2172, August 2012. doi: 10.1111/j.1365-2966.2012.21372.x.

Christopher A. Hales. Calibration Errors in Interferometric Radio Polarimetry. *AJ*, 154(2):54, August 2017. doi: 10.3847/1538-3881/aa7aef.

Xiaohong Han and R. M. Hjellming. Radio Observations of the 1989 Transient Event in V404 Cygni (= GS 2023+338). *ApJ*, 400:304, November 1992. doi: 10.1086/171996.

D. C. Hannikainen, R. W. Hunstead, D. Campbell-Wilson, K. Wu, D. J. McKay, D. P. Smits, and R. J. Sault. Radio Emission from GRO J1655-40 during the 1994 Jet Ejection Episodes. *ApJ*, 540(1):521–534, September 2000. doi: 10.1086/309294.

Diana Hannikainen, Duncan Campbell-Wilson, Richard Hunstead, Vince McIntyre, Jim Lovell, John Reynolds, Tasso Tzioumis, and Kinwah Wu. XTE J1550-564: a superluminal ejection during the September 1998 outburst. *Astrophysics and Space Science Supplement*, 276:45–48, January 2001.

Marijke Haverkorn. *Magnetic Fields in the Milky Way*, volume 407 of *Astrophysics and Space Science Library*, page 483. 2015. doi: 10.1007/978-3-662-44625-6_17.

R. M. Hjellming and M. P. Rupen. Episodic ejection of relativistic jets by the X-ray transient GRO J1655 - 40. *Nature*, 375(6531):464–468, June 1995. doi: 10.1038/375464a0.

J. A. Högbom. Aperture Synthesis with a Non-Regular Distribution of Interferometer Baselines. *A&AS*, 15:417, June 1974.

Jeroen Homan and Tomaso Belloni. The Evolution of Black Hole States. *Ap&SS*, 300(1-3):107–117, November 2005. doi: 10.1007/s10509-005-1197-4.

P. A. Hughes, H. D. Aller, and M. F. Aller. Polarized radio outbursts in BL Lacertae. II. The flux and polarization of a piston-driven shock. *ApJ*, 298:301–315, November 1985. doi: 10.1086/163611.

Sebastian Hutschenreuter and Torsten A. Enßlin. The Galactic Faraday depth sky revisited. *A&A*, 633:A150, January 2020. doi: 10.1051/0004-6361/201935479.

Adam Ingram and Sara Motta. A review of quasi-periodic oscillations from black hole X-ray binaries: observation and theory. *arXiv e-prints*, art. arXiv:2001.08758, January 2020.

Juthika Khargharia, Cynthia S. Froning, and Edward L. Robinson. Near-infrared Spectroscopy of Low-mass X-ray Binaries: Accretion Disk Contamination and Compact Object Mass Determination in V404 Cyg and Cen X-4. *ApJ*, 716(2):1105–1117, June 2010. doi: 10.1088/0004-637X/716/2/1105.

R. A. Laing. Observations of M 87 at 15.4 GHz with the 5-km telescope. *MNRAS*, 193:427–437, November 1980a. doi: 10.1093/mnras/193.3.427.

R. A. Laing. A model for the magnetic-field structure in extended radio sources. *MNRAS*, 193:439–449, November 1980b. doi: 10.1093/mnras/193.3.439.

Walter H. G. Lewin and Michiel van der Klis. *Compact Stellar X-ray Sources*. 2006.

Malcolm S. Longair. *High Energy Astrophysics*. 2011.

D. R. Lorimer and M. Kramer. *Handbook of Pulsar Astronomy*. October 2012.

J. P. Macquart, R. D. Ekers, I. Feain, and M. Johnston-Hollitt. On the Reliability of Polarization Estimation Using Rotation Measure Synthesis. *ApJ*, 750(2): 139, May 2012. doi: 10.1088/0004-637X/750/2/139.

F. Makino. GS 2023+338. *IAUC*, 4782:1, May 1989.

S. Markoff, H. Falcke, and R. Fender. A jet model for the broadband spectrum of XTE J1118+480. Synchrotron emission from radio to X-rays in the Low/Hard

spectral state. *A&A*, 372:L25–L28, June 2001. doi: 10.1051/0004-6361:20010420.

Jeffrey E. McClintock and Ronald A. Remillard. *Black hole binaries*, volume 39, pages 157–213. 2006.

J. P. McMullin, B. Waters, D. Schiebel, W. Young, and K. Golap. CASA Architecture and Applications. In R. A. Shaw, F. Hill, and D. J. Bell, editors, *Astronomical Data Analysis Software and Systems XVI*, volume 376 of *Astronomical Society of the Pacific Conference Series*, page 127, October 2007.

F. Meyer, B. F. Liu, and E. Meyer-Hofmeister. Evaporation: The change from accretion via a thin disk to a coronal flow. *A&A*, 361:175–188, Sep 2000.

E. Meyer-Hofmeister and F. Meyer. The relation between radio and X-ray luminosity of black hole binaries: affected by inner cool disks? *A&A*, 562: A142, February 2014. doi: 10.1051/0004-6361/201322423.

J. C. A. Miller-Jones, S. Migliari, R. P. Fender, T. W. J. Thompson, M. van der Klis, and M. Méndez. Coupled Radio and X-Ray Emission and Evidence for Discrete Ejecta in the Jets of SS 433. *ApJ*, 682(2):1141–1151, August 2008. doi: 10.1086/589144.

J. C. A. Miller-Jones, P. G. Jonker, V. Dhawan, W. Brisken, M. P. Rupen, G. Nelemans, and E. Gallo. The First Accurate Parallax Distance to a Black Hole. *ApJL*, 706(2):L230–L234, December 2009. doi: 10.1088/0004-637X/706/2/L230.

James C. A. Miller-Jones, Alexandra J. Tetarenko, Gregory R. Sivakoff, Matthew J. Middleton, Diego Altamirano, Gemma E. Anderson, Tomaso M. Belloni, Rob P. Fender, Peter G. Jonker, Elmar G. Körding, Hans A. Krimm, Dipankar Maitra, Sera Markoff, Simone Migliari, Kunal P. Mooley, Michael P.

Rupen, David M. Russell, Thomas D. Russell, Craig L. Sarazin, Roberto Soria, and Valeriu Tudose. A rapidly changing jet orientation in the stellar-mass black-hole system V404 Cygni. *Nature*, 569(7756):374–377, April 2019. doi: 10.1038/s41586-019-1152-0.

S. E. Motta, J. J. E. Kajava, C. Sánchez-Fernández, M. Giustini, and E. Kuulkers. The black hole binary V404 Cygni: a highly accreting obscured AGN analogue. *MNRAS*, 468(1):981–993, June 2017. doi: 10.1093/mnras/stx466.

T. Oosterbroek, M. van der Klis, B. Vaughan, J. van Paradijs, R. Rutledge, W. H. G. Lewin, Y. Tanaka, F. Nagase, T. Dotani, K. Mitsuda, and K. Yoshida. On the origin of the iron line in GS 2023+338. *A&A*, 309:781–786, May 1996.

N. Oppermann, H. Junklewitz, G. Robbers, M. R. Bell, T. A. Enßlin, A. Bonafede, R. Braun, J. C. Brown, T. E. Clarke, I. J. Feain, B. M. Gaensler, A. Hammond, L. Harvey-Smith, G. Heald, M. Johnston-Hollitt, U. Klein, P. P. Kronberg, S. A. Mao, N. M. McClure-Griffiths, S. P. O'Sullivan, L. Pratley, T. Robishaw, S. Roy, D. H. F. M. Schnitzeler, C. Sotomayor-Beltran, J. Stevens, J. M. Stil, C. Sunstrum, A. Tanna, A. R. Taylor, and C. L. Van Eck. An improved map of the Galactic Faraday sky. *A&A*, 542:A93, June 2012. doi: 10.1051/0004-6361/201118526.

N. Oppermann, H. Junklewitz, M. Greiner, T. A. Enßlin, T. Akahori, E. Carretti, B. M. Gaensler, A. Goobar, L. Harvey-Smith, M. Johnston-Hollitt, L. Pratley, D. H. F. M. Schnitzeler, J. M. Stil, and V. Vacca. Estimating extragalactic Faraday rotation. *A&A*, 575:A118, March 2015. doi: 10.1051/0004-6361/201423995.

R. A. Perley and B. J. Butler. Integrated Polarization Properties of 3C48, 3C138, 3C147, and 3C286. *ApJS*, 206(2):16, June 2013. doi: 10.1088/0067-0049/206/2/16.

R. A. Perley and B. J. Butler. An Accurate Flux Density Scale from 50 MHz to 50 GHz. *ApJS*, 230(1):7, May 2017. doi: 10.3847/1538-4365/aa6df9.

S. O. Rice. Mathematical analysis of random noise. *The Bell System Technical Journal*, 24(1):46–156, 1945. doi: 10.1002/j.1538-7305.1945.tb00453.x.

Gerold A. Richter. V404 Cyg - a Further Outburst in 1956. *Information Bulletin on Variable Stars*, 3362:1, August 1989.

A. P. Rushton, J. C. A. Miller-Jones, P. A. Curran, G. R. Sivakoff, M. P. Rupen, Z. Paragi, R. E. Spencer, J. Yang, D. Altamirano, T. Belloni, R. P. Fender, H. A. Krimm, D. Maitra, S. Migliari, D. M. Russell, T. D. Russell, R. Soria, and V. Tudose. Resolved, expanding jets in the Galactic black hole candidate XTE J1908+094. *MNRAS*, 468(3):2788–2802, July 2017. doi: 10.1093/mnras/stx526.

D. M. Russell, S. Markoff, P. Casella, A. G. Cantrell, R. Chatterjee, R. P. Fender, E. Gallo, P. Gandhi, J. Homan, D. Maitra, J. C. A. Miller-Jones, K. O'Brien, and T. Shahbaz. Jet spectral breaks in black hole X-ray binaries. *MNRAS*, 429(1):815–832, February 2013. doi: 10.1093/mnras/sts377.

George B. Rybicki and Alan P. Lightman. *Radiative processes in astrophysics*. 1979.

F. R. Schwab. Relaxing the isoplanatism assumption in self-calibration; applications to low-frequency radio interferometry. *AJ*, 89:1076–1081, July 1984. doi: 10.1086/113605.

A. M. Stirling, R. E. Spencer, C. J. de la Force, M. A. Garrett, R. P. Fender, and R. N. Ogley. A relativistic jet from Cygnus X-1 in the low/hard X-ray state. *MNRAS*, 327(4):1273–1278, November 2001. doi: 10.1046/j.1365-8711.2001.04821.x.

A. M. Stirling, R. E. Spencer, T. V. Cawthorne, and Z. Paragi. Polarization and kinematic studies of SS 433 indicate a continuous and decelerating jet. *MNRAS*, 354(4):1239–1254, November 2004. doi: 10.1111/j.1365-2966.2004.08285.x.

H. Tananbaum, H. Gursky, E. Kellogg, R. Giacconi, and C. Jones. Observation of a Correlated X-Ray Transition in Cygnus X-1. *ApJL*, 177:L5, October 1972. doi: 10.1086/181042.

G.B. Taylor, C.L. Carilli, R.A. Perley, and National Radio Astronomy Observatory (U.S.). *Synthesis Imaging in Radio Astronomy II: A Collection of Lectures from the Sixth NRAO/NMIMT Synthesis Imaging Summer School Held at Socorro, New Mexico, USA, 17-23 June, 1998*. Astronomical Society of the Pacific conference series. Astronomical Society of the Pacific, 1999. ISBN 9781583810057. URL `https://books.google.ca/books?id=e23vAAAAMAAJ`.

A. J. Tetarenko, G. R. Sivakoff, J. C. A. Miller-Jones, E. W. Rosolowsky, G. Petitpas, M. Gurwell, J. Wouterloot, R. Fender, S. Heinz, D. Maitra, S. B. Markoff, S. Migliari, M. P. Rupen, A. P. Rushton, D. M. Russell, T. D. Russell, and C. L. Sarazin. Extreme jet ejections from the black hole X-ray binary V404 Cygni. *MNRAS*, 469(3):3141–3162, August 2017. doi: 10.1093/mnras/stx1048.

B. E. Tetarenko, G. R. Sivakoff, C. O. Heinke, and J. C. Gladstone. WATCHDOG: A Comprehensive All-sky Database of Galactic Black Hole X-ray Binaries. *ApJS*, 222(2):15, February 2016. doi: 10.3847/0067-0049/222/2/15.

H. van der Laan. A Model for Variable Extragalactic Radio Sources. *Nature*, 211(5054):1131–1133, September 1966. doi: 10.1038/2111131a0.

C. L. Van Eck, J. C. Brown, J. M. Stil, K. Rae, S. A. Mao, B. M. Gaensler, A. Shukurov, A. R. Taylor, M. Haverkorn, P. P. Kronberg, and N. M. McClure-Griffiths. Modeling the Magnetic Field in the Galactic Disk Using New

Rotation Measure Observations from the Very Large Array. *ApJ*, 728(2):97, February 2011. doi: 10.1088/0004-637X/728/2/97.

Feng Yuan and Ramesh Narayan. Hot Accretion Flows Around Black Holes. *Annual Review of Astronomy and Astrophysics*, 52:529–588, Aug 2014. doi: 10.1146/annurev-astro-082812-141003.

Andrzej A. Zdziarski, Patryk Pjanka, Marek Sikora, and Łukasz Stawarz. Jet contributions to the broad-band spectrum of Cyg X-1 in the hard state. *MNRAS*, 442(4):3243–3255, August 2014. doi: 10.1093/mnras/stu1009.

Piotr T. Życki, Chris Done, and David A. Smith. The 1989 May outburst of the soft X-ray transient GS 2023+338 (V404 Cyg). *MNRAS*, 309(3):561–575, November 1999. doi: 10.1046/j.1365-8711.1999.02885.x.

# Appendices

# A Data Tables

| 5/7 GHz: Uncorrected | | | | | | | | | | | | |
|---|---|---|---|---|---|---|---|---|---|---|---|---|
| | MCMC | | | RM$_1$ | | | | RM$_2$ | | | | |
| Time$_c$ | RM (rad m$^{-2}$) | $\psi_w$ (°) | $\psi_0$ (°) | RM (rad m$^{-2}$) | $\psi_w$ (°) | $\psi_0$ (°) | S/N | RM (rad m$^{-2}$) | $\psi_w$ (°) | $\psi_0$ (°) | S/N |
| 11:15:12 | $-196^{+35}_{-38}$ | $58.1^{+2.2}_{-2.1}$ | $84.6^{+7.0}_{-7.2}$ | $-280^{+117}_{-117}$ | $64.5^{+4.5}_{-4.5}$ | $103.9^{+15.4}_{-15.4}$ | 6.4 | – – | – – | – – | – – |
| 11:29:11 | $-104^{+28}_{-32}$ | $55.8^{+1.6}_{-1.5}$ | $70.1^{+5.4}_{-5.9}$ | $-131^{+75}_{-75}$ | $57.3^{+2.9}_{-2.9}$ | $75.3^{+9.6}_{-9.6}$ | 9.9 | $2388^{+102}_{-102}$ | $160.0^{+3.9}_{-3.9}$ | $11.9^{+13.0}_{-13.0}$ | 7.3 |
| 11:43:11 | $-132^{+24}_{-25}$ | $60.6^{+1.3}_{-1.3}$ | $78.8^{+4.7}_{-4.7}$ | $-136^{+31}_{-31}$ | $61.0^{+1.2}_{-1.2}$ | $79.7^{+4.0}_{-4.0}$ | 23.9 | – – | – – | – – | – – |
| 11:57:12 | $-178^{+28}_{-28}$ | $48.9^{+1.6}_{-1.5}$ | $72.9^{+5.3}_{-5.3}$ | $-156^{+32}_{-32}$ | $47.8^{+1.2}_{-1.2}$ | $69.0^{+4.0}_{-4.0}$ | 23.6 | $-5412^{+148}_{-148}$ | $98.7^{+5.7}_{-5.7}$ | $113.2^{+18.6}_{-18.6}$ | 5.0 |
| 12:11:12 | $-70^{+24}_{-24}$ | $44.4^{+1.2}_{-1.2}$ | $54.3^{+4.5}_{-4.5}$ | $-80^{+36}_{-36}$ | $45.1^{+1.4}_{-1.4}$ | $55.9^{+4.3}_{-4.3}$ | 21.1 | – – | – – | – – | – – |
| 12:25:12 | $-93^{+26}_{-27}$ | $41.5^{+1.3}_{-1.3}$ | $54.8^{+5.0}_{-5.2}$ | $-118^{+42}_{-42}$ | $42.5^{+1.6}_{-1.6}$ | $58.3^{+5.1}_{-5.1}$ | 17.8 | – – | – – | – – | – – |
| 12:39:11 | $-94^{+26}_{-27}$ | $38.3^{+1.4}_{-1.5}$ | $51.8^{+5.1}_{-5.4}$ | $-134^{+53}_{-53}$ | $36.7^{+2.0}_{-2.0}$ | $55.1^{+6.6}_{-6.6}$ | 14.0 | – – | – – | – – | – – |
| 12:53:11 | $-57^{+28}_{-29}$ | $40.2^{+1.4}_{-1.4}$ | $48.1^{+5.4}_{-5.4}$ | $-115^{+70}_{-70}$ | $35.2^{+2.7}_{-2.7}$ | $51.2^{+8.7}_{-8.7}$ | 10.7 | – – | – – | – – | – – |
| 13:07:12 | $-93^{+25}_{-28}$ | $43.5^{+1.4}_{-1.4}$ | $56.4^{+4.9}_{-5.3}$ | $-178^{+73}_{-73}$ | $40.9^{+2.8}_{-2.8}$ | $66.4^{+9.3}_{-9.3}$ | 10.2 | $-58973^{+145}_{-145}$ | $44.9^{+5.5}_{-5.5}$ | $0.4^{+18.5}_{-18.5}$ | 5.2 |
| 13:21:12 | $6^{+30}_{-30}$ | $41.6^{+1.6}_{-1.5}$ | $40.7^{+5.7}_{-5.6}$ | $20^{+62}_{-62}$ | $39.5^{+2.4}_{-2.4}$ | $36.7^{+8.0}_{-8.0}$ | 12.1 | – – | – – | – – | – – |
| 13:35:11 | $-74^{+30}_{-32}$ | $42.3^{+1.6}_{-1.6}$ | $52.6^{+5.7}_{-6.0}$ | $-102^{+66}_{-66}$ | $39.0^{+2.5}_{-2.5}$ | $53.1^{+8.2}_{-8.2}$ | 11.4 | $6678^{+137}_{-137}$ | $73.4^{+5.2}_{-5.2}$ | $43.4^{+17.0}_{-17.0}$ | 5.5 |
| 13:49:11 | $-151^{+38}_{-43}$ | $40.2^{+2.0}_{-2.0}$ | $61.5^{+7.3}_{-7.9}$ | $-268^{+86}_{-86}$ | $39.8^{+3.3}_{-3.3}$ | $76.2^{+10.5}_{-10.5}$ | 8.7 | $-28811^{+117}_{-117}$ | $5.7^{+4.5}_{-4.5}$ | $144.2^{+14.3}_{-14.3}$ | 6.4 |
| 14:03:12 | $-90^{+31}_{-32}$ | $39.2^{+1.6}_{-1.6}$ | $52.3^{+6.0}_{-6.2}$ | $-253^{+124}_{-124}$ | $31.0^{+4.8}_{-4.8}$ | $65.2^{+15.2}_{-15.2}$ | 6.0 | – – | – – | – – | – – |
| 14:17:12 | $-97^{+32}_{-32}$ | $43.1^{+1.6}_{-1.4}$ | $57.2^{+6.1}_{-6.2}$ | $-236^{+117}_{-117}$ | $41.8^{+4.5}_{-4.5}$ | $73.7^{+14.3}_{-14.3}$ | 6.4 | $-88882^{+142}_{-142}$ | $115.4^{+5.4}_{-5.4}$ | $60.5^{+17.3}_{-17.3}$ | 5.3 |
| 14:31:12 | $-118^{+37}_{-37}$ | $38.5^{+1.8}_{-2.0}$ | $55.6^{+7.2}_{-7.4}$ | – – | – – | – – | – – | – – | – – | – – | – – |

**Table A.1:** Polarimetric results for the 5/7 GHz observations with no delay correction. RM1 and RM2 correspond to the polarization proprieties of the most significant and second most significant detection in each Faraday dispersion function. Note that some FDF had a 3$^{\text{rd}}$ or 4$^{\text{th}}$ component, but they were omitted from the data table.

| 5/7 GHz: Flare I Correction | | | | | | | | | | | |
|---|---|---|---|---|---|---|---|---|---|---|---|
| | MCMC | | | $RM_1$ | | | | $RM_2$ | | | |
| $Time_c$ | RM ($rad\,m^{-2}$) | $\psi_w$ (°) | $\psi_0$ (°) | RM ($rad\,m^{-2}$) | $\psi_w$ (°) | $\psi_0$ (°) | S/N | RM ($rad\,m^{-2}$) | $\psi_w$ (°) | $\psi_0$ (°) | S/N |
| 11:15:12 | $-181^{+39}_{-38}$ | $60.2^{+2.5}_{-2.3}$ | $84.8^{+7.8}_{-7.5}$ | $-228^{+93}_{-93}$ | $65.6^{+3.6}_{-3.6}$ | $98.0^{+12.3}_{-12.3}$ | 8.0 | −− | −− | −− | −− |
| 11:29:11 | $-150^{+28}_{-28}$ | $56.2^{+1.5}_{-1.4}$ | $76.7^{+5.4}_{-5.3}$ | $-188^{+57}_{-57}$ | $56.3^{+2.2}_{-2.2}$ | $82.3^{+7.3}_{-7.3}$ | 13.2 | $2357^{+117}_{-117}$ | $161.3^{+4.5}_{-4.5}$ | $14.8^{+15.1}_{-15.1}$ | 6.4 |
| 11:43:11 | $-137^{+24}_{-25}$ | $62.0^{+1.4}_{-1.4}$ | $80.8^{+4.7}_{-4.7}$ | $-124^{+30}_{-30}$ | $61.8^{+1.1}_{-1.1}$ | $79.0^{+3.8}_{-3.8}$ | 25.1 | −− | −− | −− | −− |
| 11:57:12 | $-200^{+28}_{-29}$ | $47.4^{+1.7}_{-1.5}$ | $73.6^{+5.4}_{-5.2}$ | $-174^{+33}_{-33}$ | $46.1^{+1.3}_{-1.3}$ | $69.1^{+4.1}_{-4.1}$ | 22.4 | −− | −− | −− | −− |
| 12:11:12 | $-110^{+25}_{-27}$ | $44.7^{+1.3}_{-1.3}$ | $59.6^{+4.7}_{-4.9}$ | $-127^{+40}_{-40}$ | $44.9^{+1.5}_{-1.5}$ | $61.4^{+4.9}_{-4.9}$ | 18.6 | −− | −− | −− | −− |
| 12:25:12 | $-87^{+27}_{-26}$ | $41.9^{+1.4}_{-1.4}$ | $53.9^{+5.1}_{-5.0}$ | $-121^{+48}_{-48}$ | $42.4^{+1.9}_{-1.9}$ | $58.2^{+6.0}_{-6.0}$ | 15.4 | −− | −− | −− | −− |
| 12:39:11 | $-107^{+25}_{-27}$ | $40.3^{+1.4}_{-1.4}$ | $55.1^{+4.8}_{-5.2}$ | $-179^{+63}_{-63}$ | $37.5^{+2.4}_{-2.4}$ | $61.3^{+7.9}_{-7.9}$ | 11.8 | $-16707^{+123}_{-123}$ | $106.8^{+4.7}_{-4.7}$ | $176.7^{+15.4}_{-15.4}$ | 6.1 |
| 12:53:11 | $-61^{+28}_{-28}$ | $40.3^{+1.5}_{-1.5}$ | $48.5^{+5.2}_{-5.3}$ | $-160^{+70}_{-70}$ | $34.7^{+2.7}_{-2.7}$ | $56.5^{+9.0}_{-9.0}$ | 10.6 | $-16685^{+143}_{-143}$ | $68.1^{+5.5}_{-5.5}$ | $178.3^{+18.2}_{-18.2}$ | 5.2 |
| 13:07:12 | $-100^{+27}_{-28}$ | $43.8^{+1.5}_{-1.5}$ | $57.3^{+5.2}_{-5.4}$ | $-178^{+73}_{-73}$ | $40.6^{+2.8}_{-2.8}$ | $65.2^{+9.4}_{-9.4}$ | 10.2 | −− | −− | −− | −− |
| 13:21:12 | $-27^{+28}_{-29}$ | $42.0^{+1.6}_{-1.7}$ | $45.7^{+5.4}_{-5.5}$ | $-16^{+70}_{-70}$ | $38.0^{+2.7}_{-2.7}$ | $40.2^{+9.0}_{-9.0}$ | 10.6 | −− | −− | −− | −− |
| 13:35:11 | $-78^{+27}_{-27}$ | $43.2^{+1.6}_{-1.6}$ | $53.7^{+5.2}_{-5.3}$ | $-161^{+82}_{-82}$ | $39.1^{+3.2}_{-3.2}$ | $60.7^{+10.3}_{-10.3}$ | 9.1 | $-16604^{+148}_{-148}$ | $93.2^{+5.7}_{-5.7}$ | $158.6^{+18.7}_{-18.7}$ | 5.0 |
| 13:49:11 | $-118^{+32}_{-34}$ | $-136.3^{+1.8}_{-1.9}$ | $-120.2^{+6.2}_{-6.6}$ | $-339^{+112}_{-112}$ | $42.0^{+4.3}_{-4.3}$ | $86.6^{+13.8}_{-13.8}$ | 6.7 | −− | −− | −− | −− |
| 14:03:12 | $-65^{+30}_{-32}$ | $41.5^{+1.6}_{-1.7}$ | $50.5^{+5.8}_{-6.1}$ | $-226^{+121}_{-121}$ | $36.5^{+4.7}_{-4.7}$ | $66.0^{+14.8}_{-14.8}$ | 6.1 | $5600^{+131}_{-131}$ | $73.4^{+5.0}_{-5.0}$ | $64.2^{+16.0}_{-16.0}$ | 5.7 |
| 14:17:12 | $-88^{+31}_{-31}$ | $44.9^{+1.6}_{-1.6}$ | $57.1^{+5.8}_{-5.9}$ | $7273^{+118}_{-118}$ | $162.6^{+4.6}_{-4.6}$ | $120.6^{+14.4}_{-14.4}$ | 6.3 | $-239^{+130}_{-130}$ | $43.9^{+5.0}_{-5.0}$ | $74.9^{+15.9}_{-15.9}$ | 5.7 |
| 14:31:12 | $-76^{+60}_{-62}$ | $41.2^{+3.2}_{-3.3}$ | $51.5^{+11.4}_{-11.7}$ | – | – | – | – | −− | −− | −− | −− |

**Table A.2:** Polarimetric results for the 5/7 GHz observations corrected for the flare I delays.

| 5/7 GHz: Flare II Correction | | | | | | | | | | | |
|---|---|---|---|---|---|---|---|---|---|---|---|
| | MCMC | | | $RM_1$ | | | | $RM_2$ | | | |
| $Time_c$ | RM ($rad\,m^{-2}$) | $\psi_w$ (°) | $\psi_0$ (°) | RM ($rad\,m^{-2}$) | $\psi_w$ (°) | $\psi_0$ (°) | S/N | RM ($rad\,m^{-2}$) | $\psi_w$ (°) | $\psi_0$ (°) | S/N |
| 11:15:12 | $-199^{+38}_{-38}$ | $59.5^{+2.1}_{-2.0}$ | $86.6^{+7.2}_{-7.1}$ | $-289^{+93}_{-93}$ | $59.7^{+3.6}_{-3.6}$ | $102.2^{+12.7}_{-12.7}$ | 8.0 | $-2985^{+148}_{-148}$ | $126.0^{+5.7}_{-5.7}$ | $25.7^{+20.2}_{-20.2}$ | 5.0 |
| 11:29:11 | $-113^{+27}_{-29}$ | $58.3^{+1.5}_{-1.5}$ | $73.8^{+5.2}_{-5.4}$ | $-117^{+35}_{-35}$ | $58.5^{+1.3}_{-1.3}$ | $74.9^{+4.6}_{-4.6}$ | 21.2 | $5633^{+139}_{-139}$ | $117.3^{+5.4}_{-5.4}$ | $49.0^{+18.1}_{-18.1}$ | 5.4 |
| 11:43:11 | $-296^{+25}_{-25}$ | $58.4^{+1.4}_{-1.4}$ | $97.7^{+4.7}_{-4.7}$ | $-280^{+30}_{-30}$ | $57.2^{+1.2}_{-1.2}$ | $94.5^{+3.7}_{-3.7}$ | 24.9 | $-5428^{+148}_{-148}$ | $107.0^{+5.7}_{-5.7}$ | $109.5^{+18.4}_{-18.4}$ | 5.0 |
| 11:57:12 | $-76^{+28}_{-28}$ | $45.8^{+1.7}_{-1.8}$ | $55.4^{+5.3}_{-5.3}$ | $-71^{+40}_{-40}$ | $44.1^{+1.5}_{-1.5}$ | $53.6^{+5.0}_{-5.0}$ | 18.6 | −− | −− | −− | −− |
| 12:11:12 | $-130^{+28}_{-30}$ | $44.8^{+1.5}_{-1.4}$ | $62.2^{+5.3}_{-5.4}$ | $-159^{+42}_{-42}$ | $43.8^{+1.6}_{-1.6}$ | $65.3^{+5.4}_{-5.4}$ | 17.5 | −− | −− | −− | −− |
| 12:25:12 | $-110^{+27}_{-28}$ | $40.4^{+1.4}_{-1.4}$ | $55.7^{+5.0}_{-5.3}$ | $-173^{+54}_{-54}$ | $38.8^{+2.1}_{-2.1}$ | $62.1^{+6.8}_{-6.8}$ | 13.9 | −− | −− | −− | −− |
| 12:39:11 | $-84^{+28}_{-29}$ | $40.6^{+1.4}_{-1.4}$ | $52.2^{+5.2}_{-5.4}$ | $-175^{+71}_{-71}$ | $36.4^{+2.7}_{-2.7}$ | $59.4^{+8.8}_{-8.8}$ | 10.5 | $-16648^{+137}_{-137}$ | $140.7^{+5.3}_{-5.3}$ | $170.9^{+16.9}_{-16.9}$ | 5.5 |
| 12:53:11 | $-70^{+27}_{-27}$ | $41.2^{+1.4}_{-1.4}$ | $50.8^{+5.1}_{-5.1}$ | $-134^{+73}_{-73}$ | $36.5^{+2.8}_{-2.8}$ | $54.6^{+9.3}_{-9.3}$ | 10.2 | −− | −− | −− | −− |
| 13:07:12 | $-57^{+29}_{-27}$ | $44.8^{+1.6}_{-1.5}$ | $52.4^{+5.6}_{-5.2}$ | $-102^{+69}_{-69}$ | $44.8^{+2.7}_{-2.7}$ | $58.7^{+8.8}_{-8.8}$ | 10.8 | −− | −− | −− | −− |
| 13:21:12 | $-70^{+28}_{-30}$ | $43.4^{+1.6}_{-1.6}$ | $52.8^{+5.4}_{-5.6}$ | $-109^{+87}_{-87}$ | $37.9^{+3.4}_{-3.4}$ | $52.6^{+11.1}_{-11.1}$ | 8.5 | $-16717^{+140}_{-140}$ | $81.7^{+5.4}_{-5.4}$ | $0.8^{+17.8}_{-17.8}$ | 5.3 |
| 13:35:11 | $-76^{+28}_{-31}$ | $40.7^{+1.5}_{-1.6}$ | $51.4^{+5.5}_{-6.0}$ | $-151^{+87}_{-87}$ | $35.8^{+3.3}_{-3.3}$ | $56.7^{+11.3}_{-11.3}$ | 8.6 | −− | −− | −− | −− |
| 13:49:11 | $-142^{+37}_{-38}$ | $42.6^{+1.8}_{-1.9}$ | $62.1^{+6.9}_{-7.1}$ | $-375^{+100}_{-100}$ | $41.6^{+3.9}_{-3.9}$ | $91.8^{+12.6}_{-12.6}$ | 7.4 | −− | −− | −− | −− |
| 14:03:12 | $-69^{+33}_{-35}$ | $45.4^{+1.8}_{-1.9}$ | $54.9^{+6.4}_{-6.7}$ | $2891^{+123}_{-123}$ | $159.0^{+4.7}_{-4.7}$ | $139.9^{+15.1}_{-15.1}$ | 6.1 | −− | −− | −− | −− |
| 14:17:12 | $-90^{+31}_{-32}$ | $42.8^{+1.7}_{-1.7}$ | $55.2^{+5.9}_{-6.2}$ | −− | −− | −− | −− | −− | −− | −− | −− |

**Table A.3:** Polarimetric results for the 5/7 GHz observations corrected for the flare II delays.

| Full Bandwidth: Uncorrected | | | | | | | | | | | |
|---|---|---|---|---|---|---|---|---|---|---|---|
| | MCMC | | | $RM_1$ | | | | $RM_2$ | | | |
| $Time_c$ | RM ($rad\,m^{-2}$) | $\psi_w$ (°) | $\psi_0$ (°) | RM ($rad\,m^{-2}$) | $\psi_w$ (°) | $\psi_0$ (°) | S/N | RM ($rad\,m^{-2}$) | $\psi_w$ (°) | $\psi_0$ (°) | S/N |
| 11:15:12 | $-186^{+22}_{-23}$ | $58.7^{+1.6}_{-1.6}$ | $82.7^{+4.5}_{-4.5}$ | $-191^{+57}_{-57}$ | $65.1^{+3.3}_{-3.3}$ | $88.6^{+9.0}_{-9.0}$ | 8.6 | −− | −− | −− | −− |
| 11:29:11 | $-189^{+20}_{-22}$ | $60.7^{+1.4}_{-1.3}$ | $85.1^{+4.1}_{-4.2}$ | $-210^{+45}_{-45}$ | $61.8^{+2.6}_{-2.6}$ | $88.3^{+7.2}_{-7.2}$ | 10.9 | $1996^{+76}_{-76}$ | $130.3^{+4.4}_{-4.4}$ | $59.3^{+12.1}_{-12.1}$ | 6.5 |
| 11:43:11 | $-140^{+22}_{-23}$ | $62.3^{+1.4}_{-1.4}$ | $80.3^{+4.2}_{-4.4}$ | $-150^{+20}_{-20}$ | $63.2^{+1.1}_{-1.1}$ | $82.2^{+3.2}_{-3.2}$ | 25.0 | −− | −− | −− | −− |
| 11:57:12 | $-127^{+19}_{-19}$ | $46.9^{+1.2}_{-1.3}$ | $63.4^{+3.7}_{-3.8}$ | $-109^{+20}_{-20}$ | $48.2^{+1.2}_{-1.2}$ | $61.1^{+3.1}_{-3.1}$ | 24.3 | $-5415^{+95}_{-95}$ | $11.7^{+5.5}_{-5.5}$ | $113.4^{+14.4}_{-14.4}$ | 5.2 |
| 12:11:12 | $-89^{+15}_{-16}$ | $45.4^{+1.0}_{-1.0}$ | $57.5^{+3.1}_{-3.2}$ | $-81^{+21}_{-21}$ | $46.6^{+1.2}_{-1.2}$ | $55.8^{+3.0}_{-3.0}$ | 23.7 | $-3696^{+91}_{-91}$ | $64.7^{+5.3}_{-5.3}$ | $123.0^{+13.0}_{-13.0}$ | 5.5 |
| 12:25:12 | $-124^{+21}_{-22}$ | $43.3^{+1.2}_{-1.2}$ | $60.1^{+4.1}_{-4.1}$ | $-133^{+26}_{-26}$ | $44.7^{+1.5}_{-1.5}$ | $60.7^{+3.8}_{-3.8}$ | 19.3 | $-7680^{+94}_{-94}$ | $123.5^{+5.4}_{-5.4}$ | $145.9^{+14.0}_{-14.0}$ | 5.3 |
| 12:39:11 | $-141^{+24}_{-25}$ | $42.0^{+1.5}_{-1.4}$ | $60.1^{+4.5}_{-4.5}$ | $-200^{+33}_{-33}$ | $40.0^{+1.9}_{-1.9}$ | $65.5^{+5.2}_{-5.2}$ | 15.1 | $-77205^{+95}_{-95}$ | $1.9^{+5.5}_{-5.5}$ | $141.7^{+15.0}_{-15.0}$ | 5.2 |
| 12:53:11 | $-110^{+25}_{-25}$ | $43.7^{+1.6}_{-1.5}$ | $57.3^{+4.6}_{-4.6}$ | $-230^{+44}_{-44}$ | $39.5^{+2.6}_{-2.6}$ | $70.2^{+7.2}_{-7.2}$ | 11.2 | −− | −− | −− | −− |
| 13:07:12 | $-125^{+24}_{-25}$ | $46.6^{+1.5}_{-1.6}$ | $62.0^{+4.5}_{-4.7}$ | $-231^{+45}_{-45}$ | $44.1^{+2.6}_{-2.6}$ | $75.2^{+7.3}_{-7.3}$ | 11.1 | $6802^{+97}_{-97}$ | $41.7^{+5.6}_{-5.6}$ | $27.2^{+15.9}_{-15.9}$ | 5.1 |
| 13:21:12 | $-85^{+20}_{-21}$ | $45.9^{+1.3}_{-1.2}$ | $57.1^{+4.0}_{-4.0}$ | $-91^{+40}_{-40}$ | $43.1^{+2.3}_{-2.3}$ | $55.0^{+6.3}_{-6.3}$ | 12.5 | −− | −− | −− | −− |
| 13:35:11 | $-113^{+15}_{-16}$ | $44.3^{+1.2}_{-1.1}$ | $59.5^{+3.2}_{-3.3}$ | $-138^{+39}_{-39}$ | $41.5^{+2.3}_{-2.3}$ | $58.8^{+6.1}_{-6.1}$ | 12.6 | $6832^{+87}_{-87}$ | $155.0^{+5.1}_{-5.1}$ | $18.9^{+13.5}_{-13.5}$ | 5.7 |
| 13:49:11 | $-213^{+21}_{-24}$ | $42.9^{+1.5}_{-1.7}$ | $72.2^{+4.3}_{-5.0}$ | $-254^{+47}_{-47}$ | $43.7^{+2.7}_{-2.7}$ | $74.9^{+7.2}_{-7.2}$ | 10.5 | $-28626^{+81}_{-81}$ | $13.3^{+4.7}_{-4.7}$ | $114.0^{+12.3}_{-12.3}$ | 6.1 |
| 14:03:12 | $-188^{+16}_{-18}$ | $42.2^{+1.4}_{-1.5}$ | $68.7^{+3.7}_{-4.1}$ | $-259^{+56}_{-56}$ | $35.3^{+3.2}_{-3.2}$ | $67.8^{+8.6}_{-8.6}$ | 8.9 | $-3554^{+89}_{-89}$ | $25.6^{+5.1}_{-5.1}$ | $112.3^{+13.8}_{-13.8}$ | 5.6 |
| 14:17:12 | $-150^{+18}_{-17}$ | $45.0^{+1.4}_{-1.4}$ | $66.5^{+3.9}_{-3.8}$ | $-208^{+60}_{-60}$ | $41.7^{+3.5}_{-3.5}$ | $68.5^{+9.6}_{-9.6}$ | 8.2 | $-88746^{+86}_{-86}$ | $117.7^{+4.9}_{-4.9}$ | $36.8^{+13.6}_{-13.6}$ | 5.8 |
| 14:31:12 | $-173^{+24}_{-24}$ | $41.5^{+1.5}_{-1.6}$ | $65.4^{+4.8}_{-5.0}$ | $-255^{+75}_{-75}$ | $34.3^{+4.3}_{-4.3}$ | $68.7^{+12.3}_{-12.3}$ | 6.6 | $-3639^{+93}_{-93}$ | $167.1^{+5.4}_{-5.4}$ | $116.9^{+15.4}_{-15.4}$ | 5.3 |

**Table A.4:** Polarimetric results for the full bandwidth observations without a delay correction.

| Full Bandwidth: Flare I Correction | | | | | | | | | | | |
|---|---|---|---|---|---|---|---|---|---|---|---|
| | MCMC | | | $RM_1$ | | | | $RM_2$ | | | |
| $Time_c$ | RM ($rad\,m^{-2}$) | $\psi_w$ (°) | $\psi_0$ (°) | RM ($rad\,m^{-2}$) | $\psi_w$ (°) | $\psi_0$ (°) | S/N | RM ($rad\,m^{-2}$) | $\psi_w$ (°) | $\psi_0$ (°) | S/N |
| 11:15:12 | $-157^{+18}_{-17}$ | $59.4^{+1.2}_{-1.1}$ | $80.1^{+3.5}_{-3.4}$ | $-150^{+22}_{-22}$ | $59.3^{+1.3}_{-1.3}$ | $78.5^{+3.6}_{-3.6}$ | 22.5 | −− | −− | −− | −− |
| 11:29:11 | $-266^{+16}_{-16}$ | $60.7^{+1.1}_{-1.1}$ | $94.9^{+3.1}_{-3.2}$ | $-252^{+18}_{-18}$ | $59.8^{+1.1}_{-1.1}$ | $92.1^{+3.0}_{-3.0}$ | 27.1 | −− | −− | −− | −− |
| 11:43:11 | $-79^{+25}_{-25}$ | $47.4^{+1.7}_{-1.6}$ | $56.6^{+4.5}_{-4.6}$ | $-122^{+26}_{-26}$ | $47.4^{+1.5}_{-1.5}$ | $61.3^{+3.8}_{-3.8}$ | 19.3 | −− | −− | −− | −− |
| 11:57:12 | $-91^{+20}_{-19}$ | $43.6^{+1.2}_{-1.2}$ | $55.5^{+3.9}_{-3.6}$ | $-96^{+25}_{-25}$ | $44.2^{+1.4}_{-1.4}$ | $55.4^{+3.7}_{-3.7}$ | 19.9 | −− | −− | −− | −− |
| 12:11:12 | $-119^{+21}_{-21}$ | $40.3^{+1.3}_{-1.4}$ | $56.5^{+4.2}_{-4.3}$ | $-144^{+33}_{-33}$ | $40.3^{+1.9}_{-1.9}$ | $57.5^{+5.2}_{-5.2}$ | 14.8 | −− | −− | −− | −− |
| 12:25:12 | $-126^{+23}_{-24}$ | $42.7^{+1.4}_{-1.4}$ | $59.0^{+4.3}_{-4.5}$ | $-204^{+43}_{-43}$ | $40.0^{+2.5}_{-2.5}$ | $64.9^{+6.8}_{-6.8}$ | 11.4 | $-16734^{+81}_{-81}$ | $122.7^{+4.7}_{-4.7}$ | $5.9^{+12.7}_{-12.7}$ | 6.1 |
| 12:39:11 | $-127^{+24}_{-26}$ | $45.6^{+1.5}_{-1.6}$ | $61.2^{+4.4}_{-4.8}$ | $-256^{+48}_{-48}$ | $42.8^{+2.8}_{-2.8}$ | $75.6^{+7.9}_{-7.9}$ | 10.4 | −− | −− | −− | −− |
| 12:53:11 | $-110^{+25}_{-27}$ | $48.3^{+1.8}_{-1.6}$ | $61.7^{+4.8}_{-4.9}$ | $-211^{+53}_{-53}$ | $48.3^{+3.1}_{-3.1}$ | $75.9^{+8.9}_{-8.9}$ | 9.4 | −− | −− | −− | −− |
| 13:07:12 | $-95^{+26}_{-28}$ | $45.4^{+1.9}_{-1.8}$ | $56.9^{+5.1}_{-5.1}$ | $-177^{+45}_{-45}$ | $42.9^{+2.6}_{-2.6}$ | $65.3^{+7.3}_{-7.3}$ | 11.0 | $12789^{+95}_{-95}$ | $4.8^{+5.5}_{-5.5}$ | $4.9^{+15.5}_{-15.5}$ | 5.2 |
| 13:21:12 | $-141^{+22}_{-23}$ | $45.3^{+1.4}_{-1.4}$ | $64.0^{+4.3}_{-4.5}$ | $-199^{+50}_{-50}$ | $44.9^{+2.9}_{-2.9}$ | $69.5^{+7.9}_{-7.9}$ | 9.9 | −− | −− | −− | −− |
| 13:35:11 | $-137^{+16}_{-16}$ | $41.7^{+1.2}_{-1.3}$ | $60.3^{+3.3}_{-3.5}$ | $-237^{+54}_{-54}$ | $34.1^{+3.1}_{-3.1}$ | $63.3^{+8.6}_{-8.6}$ | 9.1 | $5834^{+77}_{-77}$ | $31.3^{+4.5}_{-4.5}$ | $32.0^{+12.2}_{-12.2}$ | 6.4 |
| 13:49:11 | $-105^{+6963}_{-30}$ | $48.9^{+2.3}_{-11.2}$ | $63.3^{+951.9}_{-15.3}$ | $-158^{+76}_{-76}$ | $46.4^{+4.4}_{-4.4}$ | $65.5^{+11.9}_{-11.9}$ | 6.5 | −− | −− | −− | −− |
| 14:03:12 | $-157^{+2625}_{-19}$ | $46.4^{+1.5}_{-6.9}$ | $67.9^{+362.1}_{-9.6}$ | $-239^{+81}_{-81}$ | $41.5^{+4.7}_{-4.7}$ | $70.9^{+12.7}_{-12.7}$ | 6.1 | $47514^{+98}_{-98}$ | $145.2^{+5.7}_{-5.7}$ | $54.1^{+15.4}_{-15.4}$ | 5.1 |

**Table A.5:** Polarimetric results for the full bandwidth observations corrected with the flare I delays.

| Full Bandwidth: Flare II Correction | | | | | | | | | | | |
|---|---|---|---|---|---|---|---|---|---|---|---|
| | MCMC | | | $RM_1$ | | | | $RM_2$ | | | |
| $Time_c$ | RM ($rad\,m^{-2}$) | $\psi_w$ (°) | $\psi_0$ (°) | RM ($rad\,m^{-2}$) | $\psi_w$ (°) | $\psi_0$ (°) | S/N | RM ($rad\,m^{-2}$) | $\psi_w$ (°) | $\psi_0$ (°) | S/N |
| 11:15:12 | $-236^{+17}_{-17}$ | $57.7^{+1.1}_{-1.1}$ | $87.6^{+3.2}_{-3.3}$ | $-222^{+18}_{-18}$ | $58.8^{+1.0}_{-1.0}$ | $85.8^{+2.8}_{-2.8}$ | 27.3 | −− | −− | −− | −− |
| 11:29:11 | $-208^{+24}_{-24}$ | $56.2^{+1.6}_{-1.6}$ | $80.1^{+4.4}_{-4.4}$ | $-262^{+24}_{-24}$ | $53.2^{+1.4}_{-1.4}$ | $84.4^{+3.8}_{-3.8}$ | 20.2 | $5672^{+84}_{-84}$ | $4.3^{+4.9}_{-4.9}$ | $47.0^{+13.0}_{-13.0}$ | 5.9 |
| 11:43:11 | $-134^{+27}_{-28}$ | $46.8^{+1.6}_{-1.6}$ | $63.3^{+4.9}_{-5.0}$ | $-164^{+26}_{-26}$ | $45.9^{+1.5}_{-1.5}$ | $66.6^{+4.2}_{-4.2}$ | 19.0 | −− | −− | −− | −− |
| 11:57:12 | $-106^{+21}_{-22}$ | $40.6^{+1.3}_{-1.4}$ | $54.6^{+4.1}_{-4.4}$ | $-137^{+32}_{-32}$ | $39.2^{+1.9}_{-1.9}$ | $56.1^{+5.1}_{-5.1}$ | 15.3 | −− | −− | −− | −− |
| 12:11:12 | $-97^{+21}_{-21}$ | $41.7^{+1.2}_{-1.3}$ | $54.7^{+4.1}_{-4.2}$ | $-159^{+44}_{-44}$ | $38.3^{+2.6}_{-2.6}$ | $57.3^{+6.8}_{-6.8}$ | 11.2 | −− | −− | −− | −− |
| 12:25:12 | $-115^{+20}_{-22}$ | $43.2^{+1.3}_{-1.3}$ | $58.3^{+3.9}_{-4.1}$ | $-203^{+45}_{-45}$ | $40.9^{+2.6}_{-2.6}$ | $65.7^{+7.0}_{-7.0}$ | 11.1 | −− | −− | −− | −− |
| 12:39:11 | $-110^{+24}_{-25}$ | $48.9^{+1.6}_{-1.5}$ | $62.3^{+4.6}_{-4.5}$ | $-197^{+49}_{-49}$ | $50.2^{+2.8}_{-2.8}$ | $74.8^{+7.8}_{-7.8}$ | 10.1 | −− | −− | −− | −− |
| 12:53:11 | $-111^{+25}_{-27}$ | $46.4^{+1.8}_{-1.7}$ | $59.9^{+4.9}_{-5.0}$ | $-241^{+53}_{-53}$ | $43.3^{+3.0}_{-3.0}$ | $74.2^{+8.7}_{-8.7}$ | 9.4 | $-16705^{+97}_{-97}$ | $11.9^{+5.6}_{-5.6}$ | $1.0^{+16.0}_{-16.0}$ | 5.1 |
| 13:21:12 | $-153^{+21}_{-24}$ | $43.3^{+1.4}_{-1.5}$ | $63.8^{+4.2}_{-4.6}$ | $-293^{+53}_{-53}$ | $39.7^{+3.0}_{-3.0}$ | $76.5^{+8.5}_{-8.5}$ | 9.4 | −− | −− | −− | −− |
| 13:35:11 | $-85^{+2502}_{-18}$ | $47.0^{+1.4}_{-41.1}$ | $58.5^{+340.7}_{-43.6}$ | $-124^{+78}_{-78}$ | $41.8^{+4.5}_{-4.5}$ | $57.2^{+12.4}_{-12.4}$ | 6.3 | $5748^{+89}_{-89}$ | $25.0^{+5.2}_{-5.2}$ | $31.9^{+14.2}_{-14.2}$ | 5.5 |
| 13:49:11 | $-148^{+5963}_{-25}$ | $46.9^{+44.9}_{-1.6}$ | $67.0^{+856.2}_{-5.0}$ | $-214^{+83}_{-83}$ | $39.8^{+4.8}_{-4.8}$ | $66.3^{+13.1}_{-13.1}$ | 6.0 | $7096^{+91}_{-91}$ | $127.0^{+5.3}_{-5.3}$ | $151.2^{+14.4}_{-14.4}$ | 5.5 |

**Table A.6:** Polarimetric results for the full bandwidth observations corrected with the flare II delays.

# B Delay Histograms

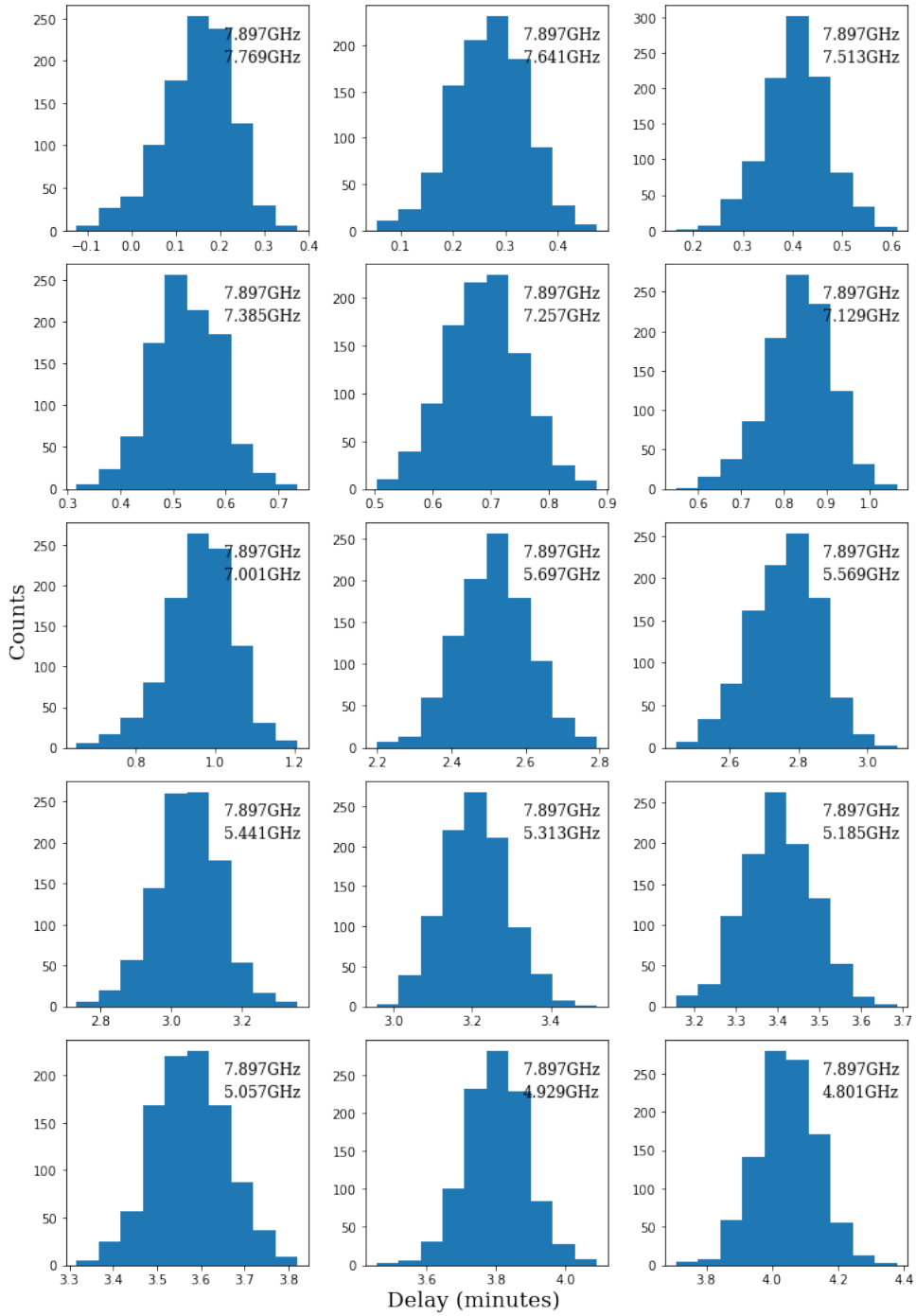


**Figure B.1:** Distribution of the ZDCF delays for the Monte Carlo re-sampled light curves of flare I limited to the 5/7 GHz bandwidth.

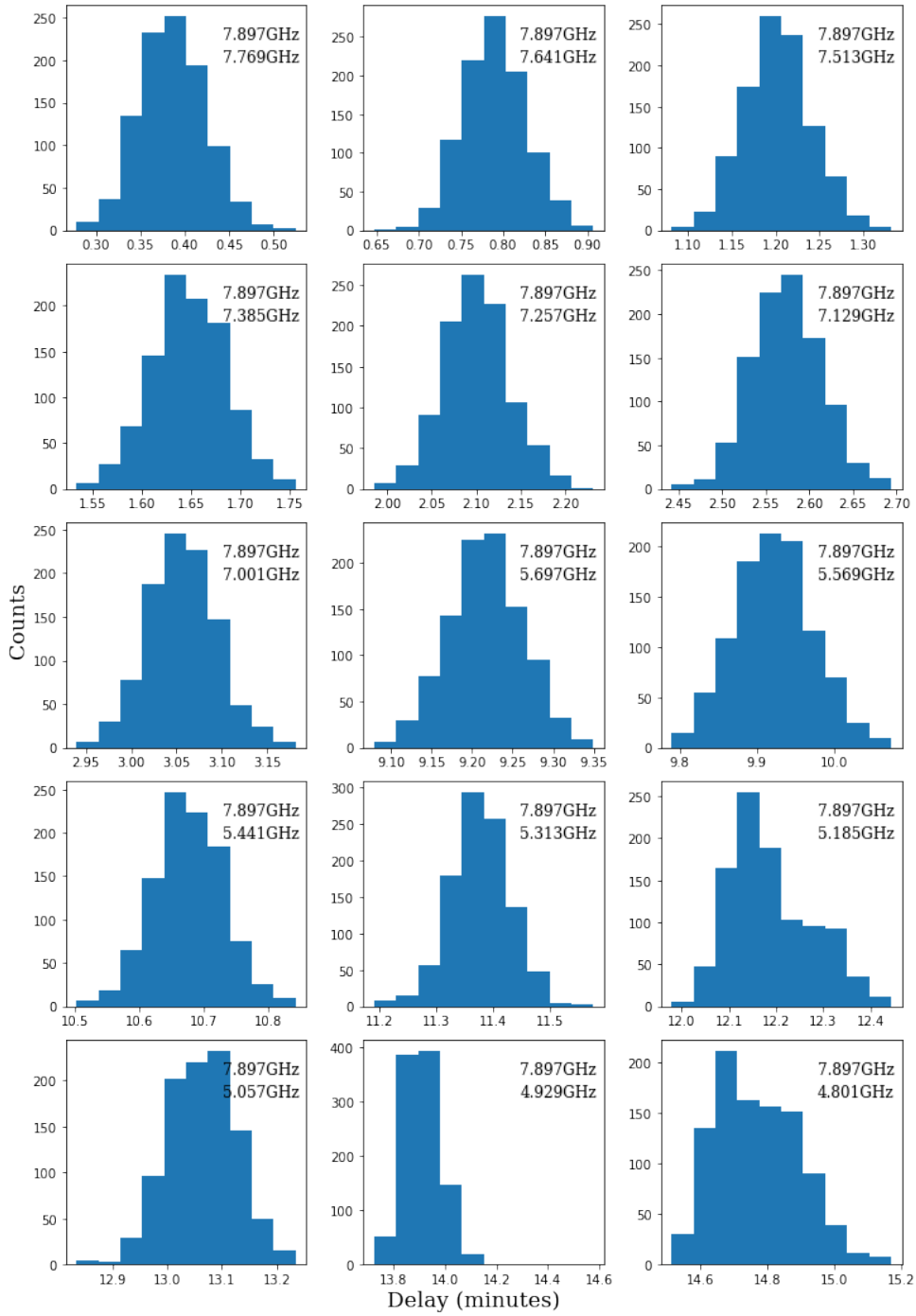


**Figure B.2:** Distribution of the ZDCF delays for the Monte Carlo re-sampled light curves of flare II limited to the 5/7 GHz bandwidth.

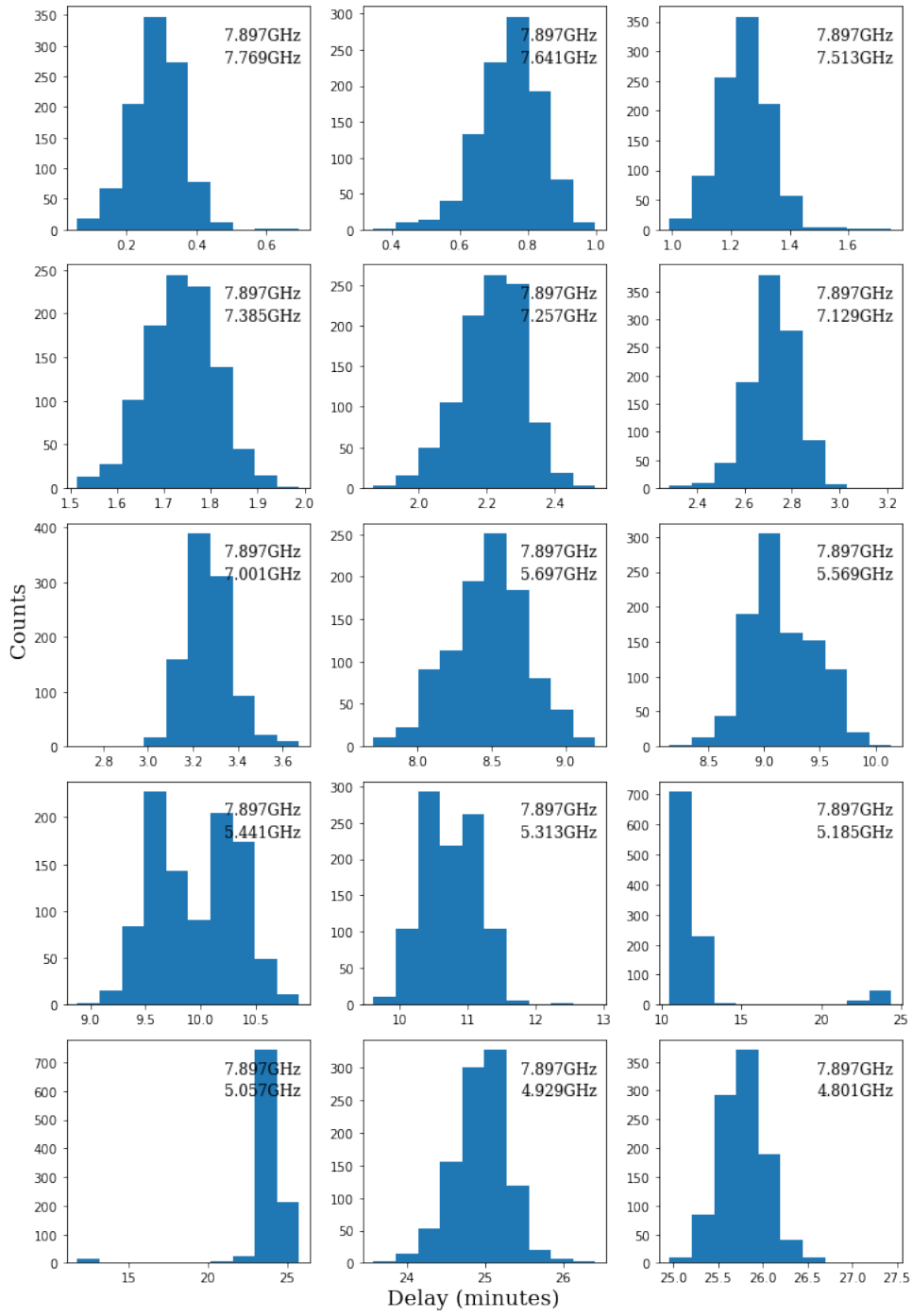


**Figure B.3:** Distribution of the ZDCF delays for the Monte Carlo re-sampled light curves of flare II limited to the 5/7 GHz bandwidth. Notice the abrupt transition from 10 minutes to 25 minutes when the comparative frequency changes from 5.185 GHz to 5.057 GHz.

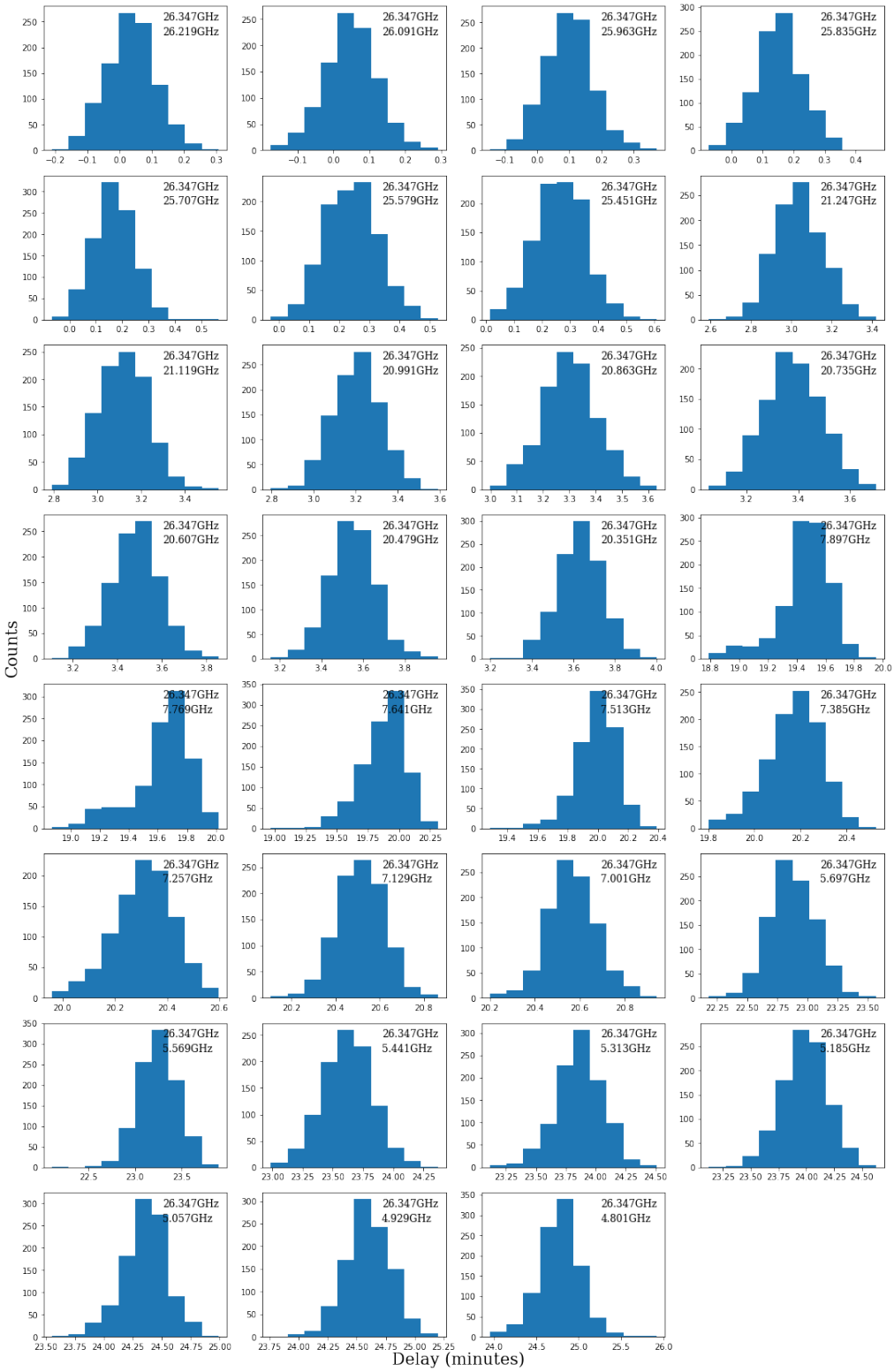


**Figure B.4:** Distribution of the ZDCF delays for the Monte Carlo re-sampled light curves of flare I limited to the full bandwidth.

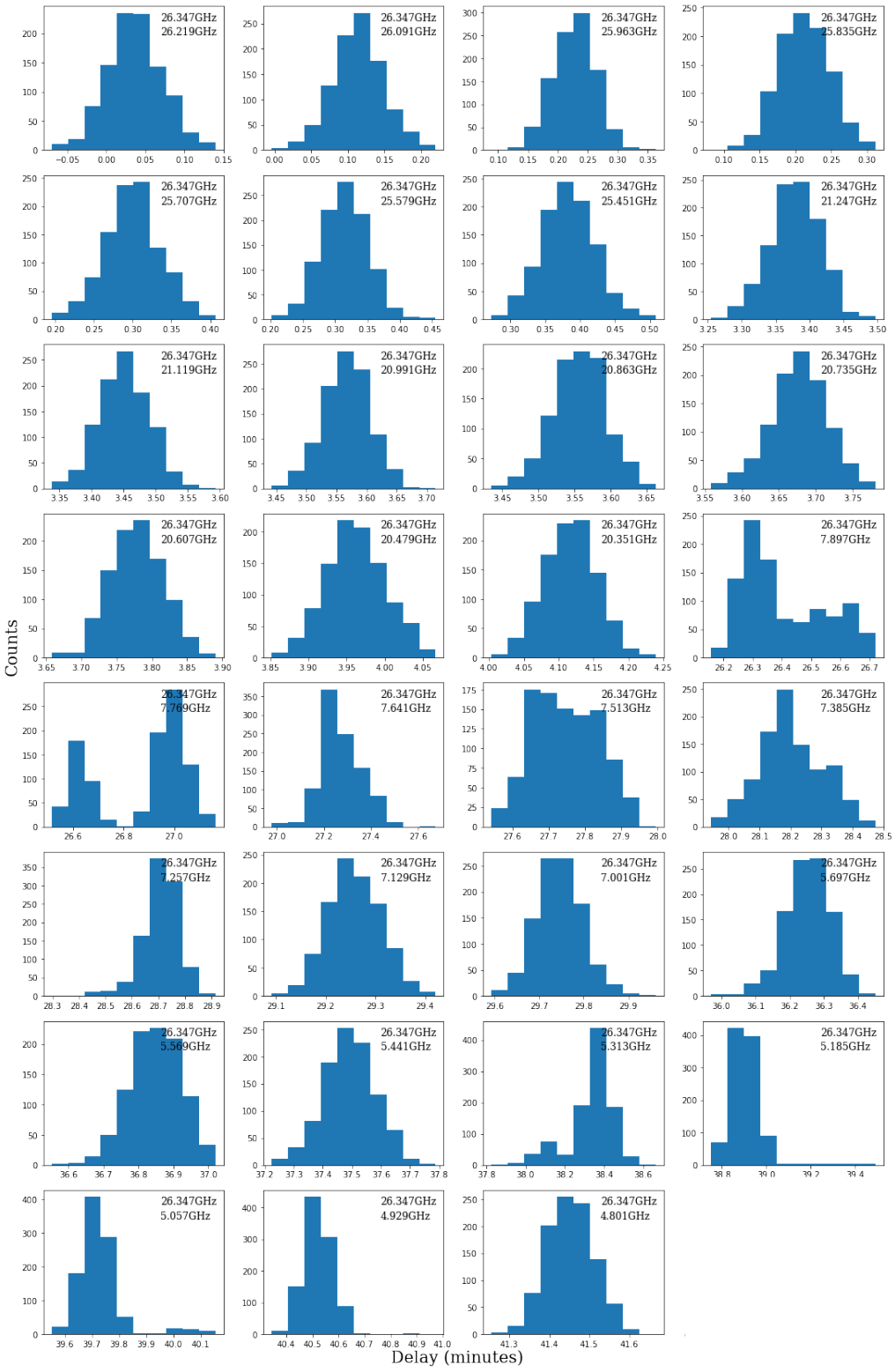


**Figure B.5:** Distribution of the ZDCF delays for the Monte Carlo re-sampled light curves of flare II limited to the full bandwidth.

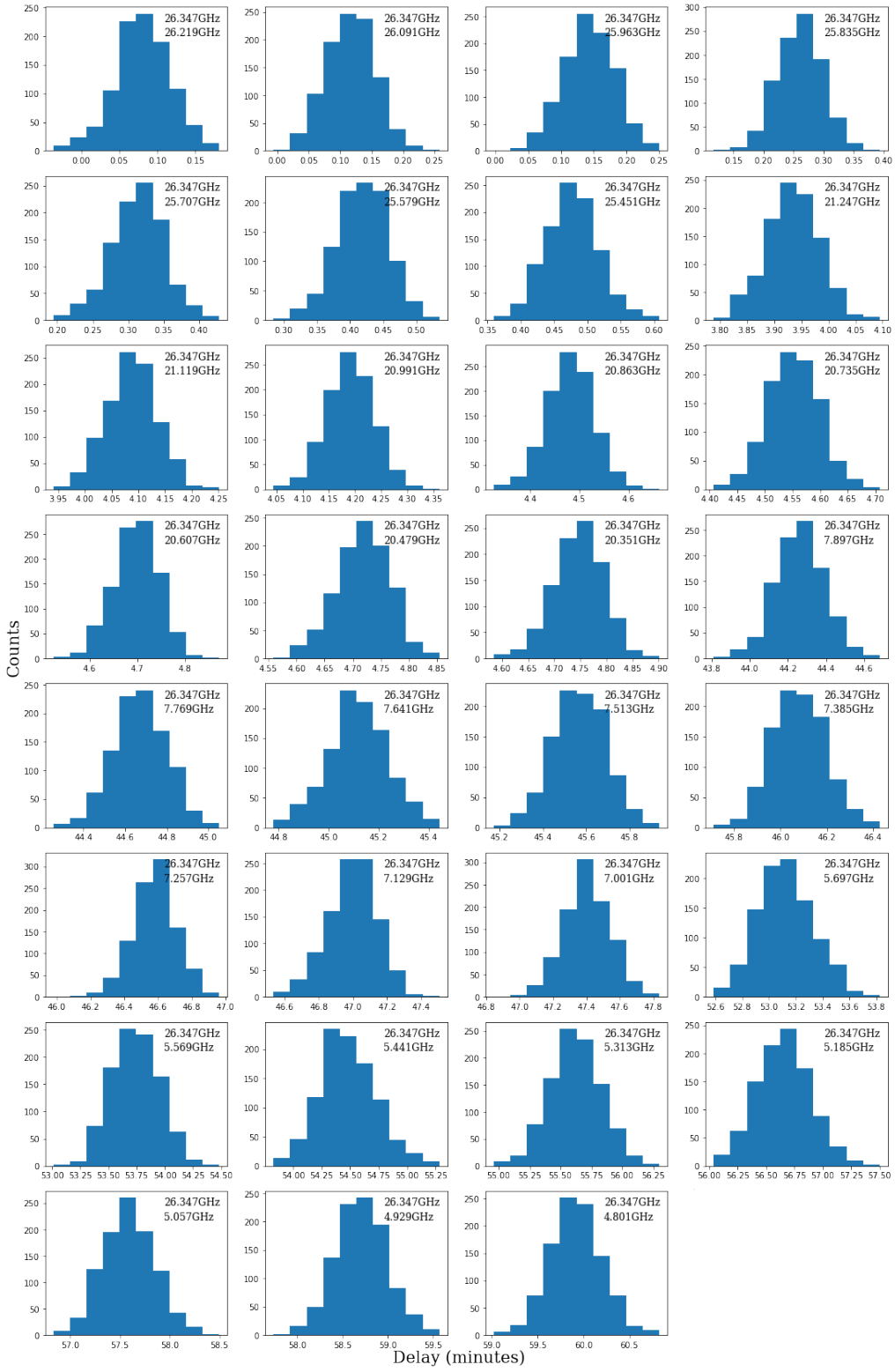


**Figure B.6:** Distribution of the ZDCF delays for the Monte Carlo re-sampled light curves of flare III limited to the full bandwidth.